

The Pennsylvania State University

The Graduate School

College of Earth and Mineral Sciences

**TRANSPORT STUDIES IN POLYMER ELECTROLYTE
FUEL CELL WITH POROUS METALLIC FLOW FIELD AT
ULTRA HIGH CURRENT DENSITY**

A Dissertation in

Energy and Mineral Engineering

by

Abdul-Kader Srouji

© 2014 Abdul-Kader Srouji

Submitted in Partial Fulfillment
of the Requirements
for the Degree of

Doctor of Philosophy

December 2014

The dissertation of Abdul-Kader Srouji was reviewed and approved* by the following:

Serguei Lvov
Professor of Energy and Mineral Engineering &
Professor of Materials Science and Engineering
Dissertation Co-Adviser
Chair of Committee

Matthew M. Mench
Department Head, Mechanical, Aerospace, and Biomedical Engineering
Condra Chair of Excellence in Energy Storage and Conversion
The University of Tennessee, Knoxville
Dissertation Co-Adviser

Jeffrey Brownson
Assitant Professor of Energy and Mineral Engineering

Randy Vander Wal
Professor of Energy and Mineral Engineering &
Professor of Materials Science and Engineering

Michael Janik
Assitant Professor of Chemical Engineering &
John J. and Jean M. Brennan Clean Energy Early Career Professor in the College of
Engineering

Luis Ayala
Associate Professor of Petroleum and Natural Gas Engineering;
Associate Department Head for Graduate Education

*Signatures are on file in the Graduate School

ABSTRACT

Achieving cost reduction for polymer electrolyte fuel cells (PEFC) requires a simultaneous effort in increasing power density while reducing precious metal loading. In PEFCs, the cathode performance is often limiting due to both the slow oxygen reduction reaction (ORR), and mass transport limitation caused by limited oxygen diffusion and liquid water flooding at high current density. This study is motivated by the achievement of ultra-high current density through the elimination of the channel/land (C/L) paradigm in PEFC flow field design. An open metallic element (OME) flow field capable of operating at unprecedented ultra-high current density (3 A/cm^2) introduces new advantages and limitations for PEFC operation. The first part of this study compares the OME with a conventional C/L flow field, through performance and electrochemical diagnostic tools such as electrochemical impedance spectroscopy (EIS). The results indicate the uniqueness of the OME's mass transport improvement. No sign of operation limitation due to flooding is noted. The second part specifically examines water management at high current density using the OME flow field. A unique experimental setup is developed to measure steady-state and transient net water drag across the membrane, in order to characterize the fundamental aspects of water transport at high current density with the OME. Instead of flooding, the new limitation is identified to be anode side dry-out of the membrane, caused by electroosmotic drag. The OME improves water removal from the cathode, which immediately improves oxygen transport and performance. However, the low water content in the cathode reduces back diffusion of water to the membrane, and electroosmotic drag dominates at high current density, leading to dry-out. The third part employs the OME

flow field as a tool that avoids C/L effects endemic to a typical flow field, in order to study oxygen transport resistance at the catalyst layer of a PEFC. In open literature, a resistance of unknown origin, was shown to directly or indirectly scale with Pt loading. A lack of understanding of the mechanism responsible for such resistance is noted, and several possible theories have been proposed. This lack of fundamental understanding of the origins of this resistance adds complexity to computational models which are designed to capture performance behavior with ultra-low loading electrodes. By employing the OME flow field as a tool to study this phenomena, the origins of the transport resistance appearing at ultra-low Platinum (Pt) loading is proposed to be an increase in oxygen dilution resistance through water film.

TABLE OF CONTENTS

LIST OF FIGURES	viii
LIST OF TABLES.....	xii
ACKNOWLEDGEMENT	xiii
Chapter 1 Introduction	1
Background.....	1
PEFC Operation.....	3
PEFC Components	4
Flow field architecture.....	6
Discussion of Theoretical Aspect	9
Water transport across the membrane.....	12
Electrochemical Impedance Spectroscopy and circuit modeling for PEFC.....	14
References	16
Chapter 2 Performance and Mass Transport in Open Metallic Element Architecture Fuel Cells at Ultra-High Current Density.....	19
Preface to Chapter 2	19
Abstract.....	20
Introduction	21
Experimental Setup and Procedure.....	24

Results and Discussion	27
Conclusion	43
References	44
Chapter 3 Ultra-High Current Density Water Management in Polymer Electrolyte Fuel	
Cell with Porous Metallic Flow Field	46
Preface to chapter 3	46
Abstract.....	47
Introduction	48
Experimental.....	54
Results and Discussion	61
Conclusion	81
References	83
Chapter 4 Oxygen Transport Resistance in Polymer Electrolyte Fuel Cell Catalyst Layer	
Preface to Chapter 4	88
Abstract.....	89
Introduction	90
Relationship of oxygen transport resistance to limiting current.....	97
Experimental Method	98
Results	100
Discussion and interpretation	111

Conclusion	115
References	116
Chapter 5 CONCLUSION	119
Chapter 6 FUTURE WORK.....	121
Fundamental two-phase transport through porous metallic element.....	121
Fundamental water transport mechanism through cell layers	122
Effect of DM properties on water retention and dry out mitigation	122
Cell active area compression	123
Wider range of Pt loading, and understanding loading effect and effective surface area	123
Durability study from dry-out cycling at ultra-high current density	124
Appendix A: Data repeatability from cell assemblies.....	125
Appendix B: Electrochemical Impedance Spectroscopy Verification with Kramer-Kronig Transform.....	129

LIST OF FIGURES

Figure 1-1. Schematic of a generic fuel cell [4]	5
Figure 1-2. Water buildup in channel and under the lands of a channel/land cell architecture, b) real-time neutron image of water buildup, reproduced from [27]	8
Figure 1-3. Typical polarization curve of a PEFC [3, 5].....	11
Figure 1-4. a) Typical Nyquist plot for PEFC, b) Equivalent circuit employed to fit impedance spectra	15
Figure 2-1. a) channel/land, b) open metallic element. (not to scale)	24
Figure 2-2. Parallel flow field performance at 60oC, under different backpressure and cathode gas dilution. (No backpressure for air, automotive pressure conditions for air, automotive pressure conditions for heliox).	27
Figure 2-3. a) Water buildup in channel and under the lands of a channel/land cell architecture, b) real-time neutron image of water buildup, reproduced from [27].	29
Figure 2-4. Performance comparison between OME and parallel flow field at 60°C, with dry air flow at the cathode using automotive conditions shown in Table 1.	30
Figure 2-5. IR-Free performance comparison between OME, and parallel flow field, with respective ASR at 60oC and air at the cathode, under automotive conditions.	32
Figure 2-6. Effect of heliox mixture on performance at 60°C with automotive operating conditions: a) Effect on parallel cell b) OME air and parallel heliox.	34
Figure 2-7. Nyquist plot for parallel and OME with air flow at the cathode: a) 0.5 A cm ⁻² , b) 1 A cm ⁻² , c) 2 A cm ⁻² , d) OME only at 2.5 and 3 A cm ⁻²	37

Figure 2-8. a) Equivalent circuit employed to fit impedance spectra, b) charge transfer resistance, c) mass transport resistance; with air flow at the cathode using automotive conditions.	39
Figure 2-9. Effect of heliox mixture on OME performance at 60°C, using automotive conditions (2 A cm ⁻² is not a stable point with Heliox, due to dry-out).	40
Figure 2-10. Voltage and ASR evolution of OME cell at 2 A cm ⁻² with Heliox flow at the cathode, and a cell temperature of 60°C.	42
Figure 2-11. Measured net water drag coefficient of OME with air, and OME with heliox using automotive conditions. The computed theoretical limit where all the water is collected at the cathode outlet is also plotted.	42
Figure 3-1. a) cross section of cathode side showing OME and improved mass transport (not to scale), b) through-plane water transport in a PEFC and net water drag (NWD), c) schematic representation of PEFC with in-line dew point temperature sensors and water desiccant bottles for live and average water measurement, respectively.	53
Figure 3-2. Performance curve and ASR for baseline conditions at a cell temperature of 60°C.	62
Figure 3-3. Cell voltage as a function of temperature with baseline condition 1, and condition 2, at 2 A cm ⁻²	65
Figure 3-4. NWD coefficient evolution as a function of temperature with baseline Condition 1, and Condition 2, at 2 A cm ⁻²	66
Figure 3-5. evolution of voltage, NWD and ASR during transient dry-out that leads to shut down of operation at 67.5 °C with baseline condition, at 2 A cm ⁻²	68

Figure 3-6. a) Nyquist plot for Baseline condition 1, b) Nyquist plot for Condition 2, c) electric circuit model used for EIS data fit.....	69
Figure 3-7. Charge transfer resistance and ASR data from EIS, for Baseline Condition 1, and condition 2, at 2 A cm^{-2}	70
Figure 3-8. Cell voltage as a function of temperature under all measured conditions, at 2 A cm^{-2}	72
Figure 3-9. NWD coefficient as a function of temperature under all measured conditions.	73
Figure 3-10. a) Nyquist plot for Condition 3, b) Nyquist plot for Condition 4.....	74
Figure 3-11. Charge transfer resistance and ASR data from EIS, for all measured conditions, at 2 A cm^{-2}	75
Figure 3-12. Calculated mass transport resistances for all measured conditions deduced from EIS data, at 2 A cm^{-2}	76
Figure 3-13. Cathode catalyst layer hydration state as interpreted from temperature step experiments a) membrane and cathode catalyst layer schematic, b) agglomerate with excess water and back diffusion, c) agglomerate with partially evaporated water film, d) enough water for ionomer hydration only, and limited back diffusion.....	80
Figure 4-1. Cross section view of cathode in a) Channel / Land, b) Open metallic element fuel cell (not to scale). Reproduced from [5].	98
Figure 4-2. Limiting current measurements at a cell operating pressure of 150 kPa, for different flow field architectures and different loadings. a) Parallel with 0.4 mgPtcm^{-2} , b) Parallel with 0.07 mgPtcm^{-2} , c) OME with 0.4 mgPtcm^{-2} , d) OME with 0.07 mgPtcm^{-2}	102

Figure 4-3. Limiting current density as a function of reactant gas partial pressure for different cells. a) Parallel with 0.4 mgPt.cm ⁻² , b) Parallel with 0.07 mgPt.cm ⁻² , c) OME with 0.4 mgPt.cm ⁻² , d) OME with 0.07 mgPt.cm ⁻²	105
Figure 4-4. Oxygen transport resistance as a function of total pressure for different cell architectures and loadings.	106
Figure 4-5. Effect of Pt loading and flow field architecture on pressure dependant molecular diffusion resistance $R_{\text{dif,p}}$	113
Figure 4-6. Effect of Pt loading and flow field architecture on the other transport resistance R_{other}	114

LIST OF TABLES

Table 1-1. Common fuel cell types and their characteristics [4, 5]	2
Table 2-1. Fuel cell automotive operating conditions	26
Table 2-2. Peak power of OME and parallel channel/land cells at cell temperature of 60°C using automotive conditions shown in Table 1.	31
Table 3-1. Baseline operating conditions	56
Table 3-2. Operating conditions for increased temperature experiments	58
Table 3-3. Calculated effective water permeability for a pressure differential of 60 kPa	66
Table 4-1. Summary of methodology and R_{other} measurements from literature.	96
Table 4-2. Cell build specifications	99
Table 4-3. Operating parameters for limiting current measurement	100
Table 4-4. Summary of computed transport resistances and effective diffusion lengths	110

ACKNOWLEDGEMENT

I owe so many acknowledgements to people who have helped me in every respect throughout this journey. Foremost, I would like to thank my advisor, Professor Matthew Mench. I have always felt so fortunate to be his student and to pursue my PhD under his supervision. I am grateful for all his guidance and support, patience, and opportunities he has provided. Besides learning from him throughout these years, I am thankful to have him as a close friend.

I owe a lot to my co-advisor, Professor Seguei Lvov, who has offered generous guidance and support. I would not be in this position today without his encouragement and support.

I would like to thank my thesis committee, Dr. Jeffrey Brownson, Dr. Mike Janik, and Dr. Randy Vander Wal for their sincere guidance and feedback, and their great teaching.

Thank you to the Nuvera Fuel Cell team, without whom most of this work would not have happened. The three years project, out of which part of my thesis work spun off was a great joy.

I am forever indebted to my parents Nabila, and Kamal, and my brother Karim, for their understanding, inexhaustible support, and encouragement. You have always been on my side, and words cannot describe how much I am thankful for all what you have done for me.

Chapter 1 Introduction

Background

A fuel cell is a power generating device. It converts the chemical energy of a fuel into electrical energy through electrochemical reactions with oxygen or another oxidizing agent. The first fuel cell can be traced to 1842, when Sir William R. Grove from south Wales, built a device which generated electrical energy by combining hydrogen and oxygen [2]. During the “space race” of the 1950s, NASA in collaboration with engineers at GE began development of fuel cells to generate power for satellites and space capsules. Their first industrial polymer electrolyte fuel cell (PEFC) system was used during Project Gemini in 1962 [2, 3]. More recently, geo-political and socio-economic distress about fossil fuel depletion and protecting the environment has encouraged governmental and private efforts in developing highly efficient and clean technologies such as fuel cells. Fuel cells are sought to be ideal for various applications, from stationary power generation to automotive engines, and consumer electronics [4]. The direct conversion of chemical energy to electrical energy without combustion means that the operating efficiencies of PEFC are not limited by Carnot Cycle. They can therefore achieve system efficiency of 50-60%, which is much higher than the internal combustion engine efficiency of 25-35% [5]. Fuel cells are also quiet due to minimal presence of moving parts, and they are free of harmful emissions. There are several types of fuel cells, each being characterized by the

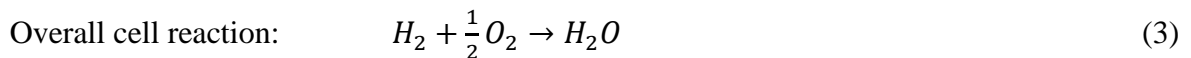
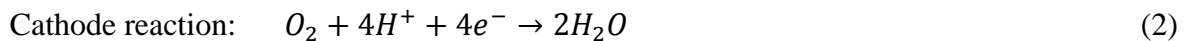
electrolyte used. The most common types are listed in Table 1. The basic operation of a PEFC and its components are described in the next section.

Table 1-1. Common fuel cell types and their characteristics [4, 5]

Fuel Cell	Electrolyte	Operating Temperature (°C)	Fuel Type	System Efficiency Qualified Power
Alkaline FC	KOH	60-120	Pure H ₂	35-55 % 10-100 kW
PEFC	Solid Polymer (Nafion®)	50-100	Pure H ₂	35-45 % 100 W- 500 kW
Phosphoric Acid FC	Phosphoric Acid	150-220	Pure H ₂	40 % < 10 MW
Molten Carbonate FC	Lithium and Potassium Carbonate	600-650	H ₂ , CO, CH ₄	>50% <100 MW
Solid Oxide FC	Solid Oxide Electrolyte (Zirconia)	500-1100	H ₂ , CO, CH ₄	> 50% <100 MW

PEFC Operation

The basic components and operation of a simple PEFC are shown in Figure 1-1. Hydrogen gas is generally supplied to the anode side of the cell while the oxidant, usually oxygen gas from the air is distributed to the cathode. At the anode, an electrochemical oxidation reaction occurs. The hydrogen gas splits into hydrogen ions H^+ and electrons e^- . The produced electrons flow through an external circuit, and can power an electric motor or other device. The hydrogen ions pass from the anode side to the cathode through a semi-permeable polymer membrane. The membrane has high ionic conductivity, but is not conductive to electrons. It therefore prevents a short circuit between the anode and cathode compartments. At the cathode, the hydrogen ions, electrons and oxygen are combined in an oxygen reduction reaction that forms water as product. The discussed electrochemical reactions are:



A catalyst layer containing nano-sized (2-4nm) platinum particles on carbon support are generally applied on each sides of the cell.

PEFC Components

In the center of the diagram of Figure 1-1, the ion conductive membrane separates anode from cathode. Its thickness varies between 15-175 μm . The type most commonly used for PEFC membranes today is polyperfluorosulfonic acid membrane. It normally consists of polytetrafluoroethylene (PTFE) backbone with sulfonic acid groups attached to the perfluorinated-vinyl-polyether side chains. When hydrated, the highly hydrophilic sulfonic acid groups will absorb water and ionize. This will enable H^+ ion transfer through the membrane.

Platinum powder nano-particles, roughly 2-4 nm in size and supported by larger (around 40 nm) carbon particles are applied to each side of the membrane. The electrochemical reactions occur on those catalyst layers. The thickness of a catalyst layer is typically 10-30 μm , and can also be referred to as electrode. The combination of membrane and catalyst layer is usually referred to as membrane electrode assembly (MEA).

The MEA is sandwiched between two backing layers also known as gas diffusion media (DM). Typical DMs are made of carbon cloth (woven) or carbon paper. Carbon cloth DMs are made of fibers woven in some pattern, whereas carbon fiber paper consists of fibers aligned in random direction. The main purpose of the DM is to transport reactant gases from flow channels to the catalyst layer. In addition, they provide support for the flow channel, and protect the catalyst layer. DMs need to be conductive in order to allow electrons to flow from the catalyst layer to the external circuit. Another important function

of the DM is its ability to remove product water away from the catalyst sites to the channel.

Flow channels, also acting as current collection plates, are made of electrically conductive material, most commonly graphite or metal. Their key function is to distribute the reactants over the assembly. They also provide adequate compression to the soft sub-layers (DM, Catalyst layer and MEA), and therefore need to be robust. This proposal will use a novel flow field design and therefore a review of common flow fields is discussed in the next section.

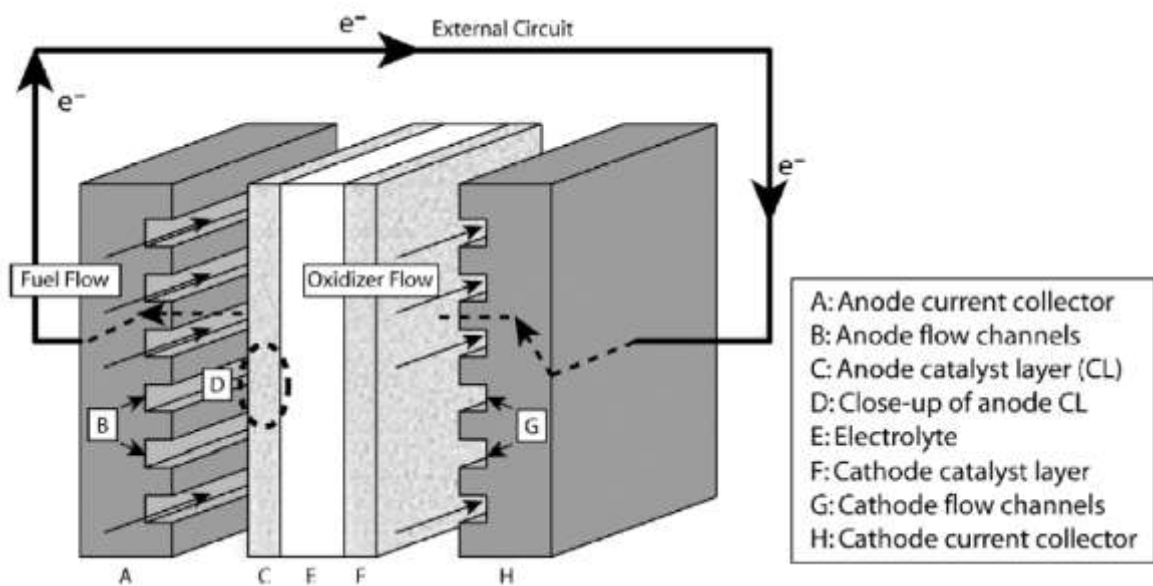


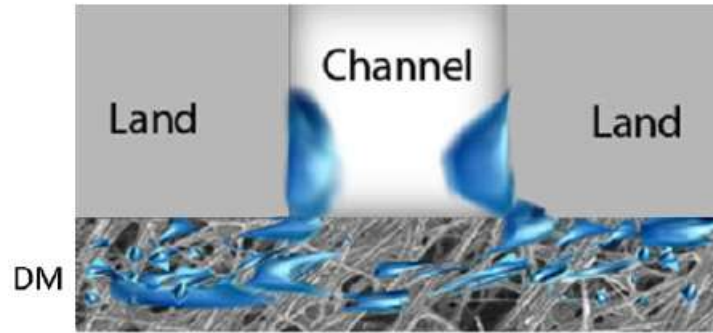
Figure 1-1. Schematic of a generic fuel cell [4]

Flow field architecture

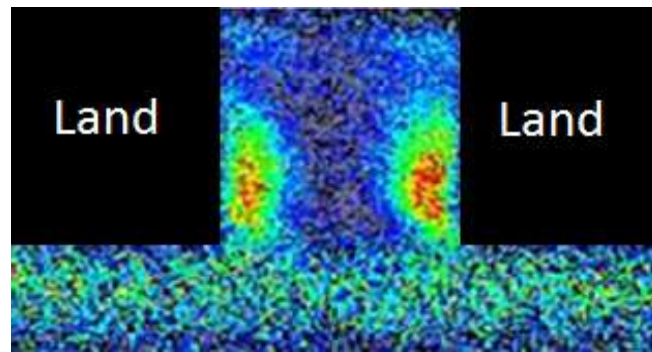
Reactant gases in a fuel cell are distributed over the gas diffusion media (DM) through a flow field, before diffusing to the reaction sites. For functional requirements, the design of a flow field must achieve adequate reactant gas distribution over their respective electrodes, provide pathways for water evacuation from the cell, translate compression from the end plates/bipolar plates to the soft materials layered within, and provide necessary electrical conduction and heat transfer.

A variety of flow field designs are well developed, including parallel, serpentine, and interdigitated (e.g [6-13]). It is important to note that even though different flow field layouts have been developed, they are generally based on a conventional alternating channel/land distribution. Parallel flow fields suffer from uneven gas flow supply and water droplet accumulation, which can result in poor performance at high current or wet conditions. Neutron imaging utilized to quantify liquid water accumulation and distribution in a PEFC showed that locations under lands have restricted mass transport and are preferential liquid storage sites, even in dryer operating conditions [14]. Figure 1-2 is a typical false colored neutron image showing water trapping and accumulation under lands. It was also shown that decreasing the land-to-channel ratio is advantageous in decreasing the water stored in the cell, but could be a drawback when operating in low humidity conditions [15]. Another neutron study revealed that the liquid storage in the gas diffusion layer increased with larger lands [16]. Larger lands create increased distance for transport of products from the electrode, and also add a shadowing effect for reactants diffusing to the electrode. A serpentine layout suffers from relatively higher pressure drop and

concentration gradients since the flow path is relatively long. Liquid water has also been shown to accumulate in turns and switchbacks [17, 18], which can harm performance, stability, and durability. The presence of lands introduces a drawback since reactant gas must diffuse under the lands to reach the electrode. At high current density, the land width was found to be the dominant factor for performance. At the same time, large channel spans cause additional ohmic resistance [19], and increase DM intrusion in the channel [20, 21]. The under-compressed DM surface below the channel makes less contact with the catalyst layer [22]. It is also shown that water in low compression interfaces is prone to ice lens formation during operation or storage at subfreezing temperatures, which ultimately causes mechanical damage to the soft materials [23]. Conventional channel/land configurations have also been developed with porous carbon material that acts as an integrated passive wick that removes excess water from the channels and DM [24-26].



a.



b.

Figure 1-2. Water buildup in channel and under the lands of a channel/land cell architecture, b) real-time neutron image of water buildup, reproduced from [27]

Discussion of Theoretical Aspect

PEFC performance

The performance of a PEFC is characterized by four kinds of losses. These are *i*) activation polarization, *ii*) ohmic polarization, *iii*) concentration (mass transfer) polarization, and *iv*) fuel cross-over polarization. The typical performance curve of a PEFC and the current density regions, where each loss dominates are as shown in Figure 1-3.

The activation polarization represents the rate of an electrochemical reaction controlled by electrode kinetics in the low current density region. Like any chemical reaction, electrochemical reactions in a PEFC involve an electronic barrier that must be overcome prior to current generation. Activation overpotential can be described by the Butler-Volmer equation for an electrode:

$$i = i_0 \left[\exp \left(\frac{\alpha_A n F}{RT} \eta_{act} \right) - \exp \left(- \frac{\alpha_c n F}{RT} \eta_{act} \right) \right] \quad (4)$$

where i represents the current density (A/m^2), F is Faraday's constant which is 96,485 (C/mole-eq), i_0 is the exchange current density (A/m^2), η_{act} is the activation overpotential, n is the number of electrons transferred in the elementary electrode reaction charge transfer sites, α_A is the anodic transfer coefficient, and finally α_c is the cathodic transfer coefficient.

Ohmic polarization are a result of limited ionic conductivity of the membrane, the electrical resistance of the various soft materials, and the inherent contact resistance at the interface of the many layers. Ohmic losses are a strong function of the hydration level of

the membrane, and are therefore affected by various operating conditions such as flow rates, gas humidity and current density. A high water content in the membrane is essential to reduce ohmic loss of the membrane. The ohmic losses are expressed by Ohm's law:

$$\eta_{ohm} = iR_{total} \quad (5)$$

Where R_{total} is the total resistance of the fuel cell including contact and ionic resistance, and i is the current density.

Concentration polarizations are a consequence of mass transport limitations of the reactant gases to the reaction sites at high current density. The increased water generation with low operating temperature (below 100°C) leads to increased water saturation in the pores of the diffusion media. This increases the tortuosity of the pathways in which reactant gases diffuse to their respective reaction sites and results in a concentration difference between the catalyst surface and the diffusion media. Consequently the electrode potential is reduced. Concentration polarization is expressed according to the Nernst equation:

$$\eta_{conc} = \frac{RT}{nF} \ln \left(1 - \frac{i}{i_L} \right) \quad (6)$$

Where i_L is the limiting current density, indicating the maximum rate at which reactant can be supplied to an electrode and T is the temperature.

Cross-over loss is the last type of loss in a PEFC. It is a result of unreacted hydrogen crossover to the cathode compartment. This leads to a reduction in electrochemical reaction rate.

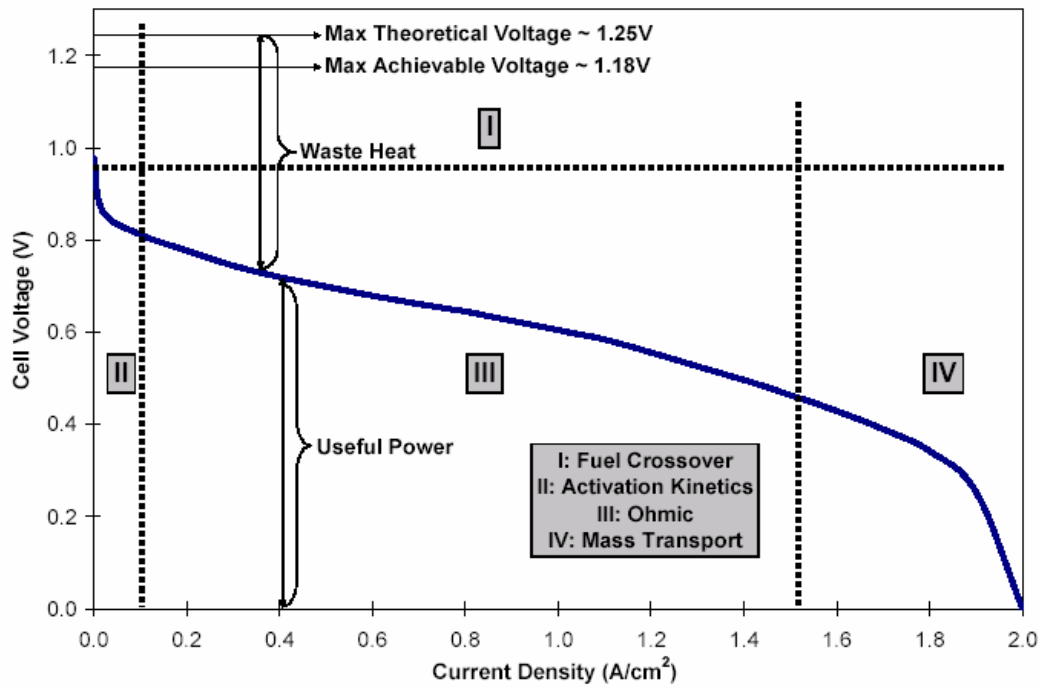


Figure 1-3. Typical polarization curve of a PEFC [3, 5]

Water transport across the membrane

Part of the water introduced in the humidified reactant streams crosses the membrane electrode assembly (MEA) which contributes to membrane and ionomer hydration. The oxygen reduction reaction at the cathode is another source of water. At elevated current densities, it is very common for the byproduct water generation rate to be orders of magnitude higher than the rate of water introduced with the gas streams. Water is also moved from the anode to the cathode side of the membrane via electroosmotic drag induced by proton transport. This is due to water forming a hydration shell around a proton, or hydrodynamic pumping due to ionic and hydration shell movement. Electroosmotic drag is increased with thinner membranes and increase membrane water content. Because electroosmotic drag affects water management in a fuel cell, it has a local and general contribution to the performance and durability. A local dry-out on the anode side of the membrane can be induced by electroosmotic drag. This affects the conductivity of the membrane and therefore increases ohmic resistance. Both water generation and electroosmotic drag contribute to dumping water in the cathode side of the MEA. Even though high water content in the cathode ionomer improves proton transport, the slight excess will result in reduced performance due to flooding and water film resistance over the electrochemically active area. Also, low water content in the ionomer phase of the cathode electrode is detrimental to charge transport and therefore performance. The dumping of water at the cathode creates a concentration gradient across the membrane. When the water concentration on the cathode side is high enough, water can move from the cathode toward the anode compartment in what is termed back diffusion of water. The

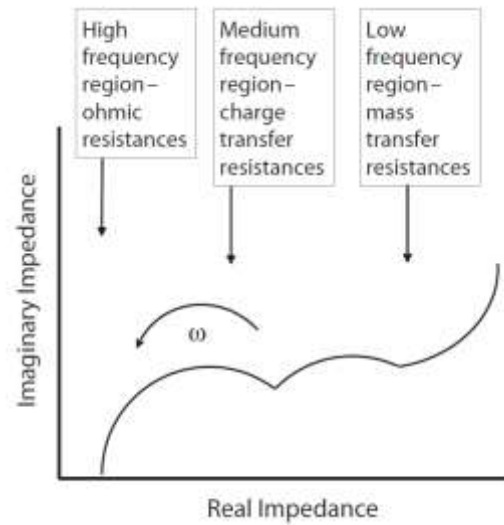
separate measurement and estimation of electroosmosis and diffusion rates are possible [28-32]. Pressure gradients between the two gas compartments (across the membrane) also affect net water transport direction. However, it is the combined effect during typical fuel cell operating conditions that dictates the overall direction of water transport, and is referred to as the effective or net water drag.

Electrochemical Impedance Spectroscopy and circuit modeling for PEFC

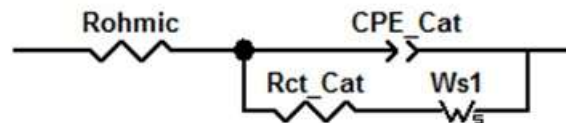
Many complex problems in electrochemistry, such as corrosion or the kinetics of a given electrode are studied with electrochemical impedance spectroscopy (EIS). In a fuel cell, voltage loss at a given current density is a result of a combination of ohmic and non-ohmic contributions. While the ohmic contributions can readily be studied with DC techniques, the non-ohmic contributions, such as adsorption processes at the electrodes, the charge transfer across the double layer, and the kinetically based concentration polarization, normally have frequency-dependent response times. Therefore those phenomena are studied using an AC technique, EIS. EIS is a great tool for fuel cells as the AC signal is applied without any modifications to the internals of the cell. Also the amplitude of the signal is minimal making the technique non-intrusive. A signal (20mV~50mV) is applied at varying frequencies (100 mHz – 5 kHz), and the response is recorded in the shape of a Nyquist or Bode plot. This response to the oscillating signal can be used to discern qualitative details of the kinetics and concentration polarization behavior at the electrodes. Using a first principle based approach or an equivalent electrical circuit, the ohmic, charge transfer and mass transport resistances can be qualitatively discerned. A generalized Nyquist plot from the frequency response is shown in Figure 1-4a.

The commonly employed equivalent circuit for data fitting is shown in Figure 1-4b, [33, 34]. Cathode charge transfer and mass transport are modeled with a resistor (R_{ct_cat}) and a finite diffusion Warburg impedance (W_{s1}) respectively, in series. The double layer capacitance for the cathode is represented with a constant phase element (CPE_Cat). The

ohmic resistance is Rohmic, which consists of the ionic resistance of the membrane in series with the ohmic resistance of the various layers and their contact resistances.



a)



b)

Figure 1-4. a) Typical Nyquist plot for PEFC, b) Equivalent circuit employed to fit impedance spectra

References

1. A. K. Srouji, L. J. Zheng, A. Turhan, M. M. Mench. J Power Sources, 218 (2012) 341.
2. M. L. Perry, and T.F. Fuller, J Electrochem Soc. 2002, 149:S59-S67.
3. M. M. Mench, Fuel Cell Engines, Wiley, 2007.
4. D. Sperling, and J. S. Cannon, The Hydrogen Energy Transition: Cutting Carbon from Transportation, Academic Press, 2004.
5. J. Larminie, and A. Dicks, Fuel Cell Systems Explained, Wiley, 2000.
6. X. Li, I. Sabir, Int. J. Hydrogen Energy 30 (2005) 359e371.
7. A. Pollegri, P.M. Spaziant, US Patent No. 4, 197,178, 1980.
8. F. Spurrier, B. Pierce, M. Wright, US Patent No. 4,631,239, 1986.
9. S. Granata, B. Woodle, US Patent No. 4,684,582, 1987.
10. D. Jeon, S. Greenway, S. Shimpalee, J. Van Zee, Int. J. Hydrogen Energy 33 (2008) 1052e1066.] G. Hu, J. Fan, S. Chen, Y. Liu, K. Cen, J. Power Sources 136 (2004) 1e9.
12. L. Wang, H. Liu, J. Power Sources 134 (2004) 185e196.
13. C. Cavalca, S. Homeyer, E. Walsworth, US Patent No. 5,686,199, 1997.
14. A. Turhan, K. Heller, J. Brenizer, M.M. Mench, J. Power Sources 160 (2006)
15. A. Turhan, K. Heller, J. Brenizer, M.M. Mench, J. Power Sources 180 (2008)
16. K. Cho, M.M. Mench, Int. J. Hydrogen Energy 35 (2010)
17. N. Pekula, K. Heller, P. Chuang, A. Turhan, M.M. Mench, J. Brenizer, K. Unlu, Nucl. Instrum. Methods Phys. Res. 542 (2005).

18. T. Trabold, J. Owejan, D. Jacobson, M. Arif, P. Huffman, *Int. J. Heat Mass Transf.* 49 (2006).
19. S. Goebel, *J. Power Sources* 196 (2011).
20. Y. Lai, P. Rapaport, C. Ji, V. Kumar, *J. Power Sources* 184 (2008).
21. Nitta, T. Hottinen, O. Himanen, M. Mikkola, *J. Power Sources* 171 (2007)
22. H. Bajpai, M. Khandelwal, E. Kumbur, M.M. Mench, *J. Power Sources* 195 (2010).
23. S. He, M.M. Mench, *J. Electrochem. Soc.* 153 (2006)
24. S. Litster, C. Buie, T. Fabian, J. Eaton, J. Santiago, *J. Power Sources* 154 (2007)
25. J. Yi, J. Yang, C. King, *AIChE J.* 50 (2004).
26. A. Weber, R. Darling, *J. Power Sources* 168 (2007).
27. A. Turhan, S. Kim, M. Hatzell, M.M. Mench, *Electrochim. Acta* 55 (2010)
28. T. A. Zawodzinski, S. Radzinski, R.J. Sherman, V.T. Smith, T.E. Springer, S. Gottesfeld, *J. Electrochem. Soc.* 140 (1993) 1041–1047.
29. T. A. Zawodzinski, J. Davey, J. Valerio, S. Gottesfeld, *Electrochim. Acta* 40 (1995) 297–302.
30. A. B. LaConti, A.R. Fragala, J.R. Boyack, in: D.E. McIntyre, S. Srinivasan, E.G. Will (Eds.), *Proceedings of the Symposium on Electrode Materials and Processes for Energy Conversion and Storage*, vol. 77, 1977, p. 354.
31. T.F. Fuller, J. Newman, *J. Electrochem. Soc.* 139 (1992) 1332–1339.
32. G. Xie, T. Okada, *J. Electrochem. Soc.* 142 (1995) 3057–3062.
33. D. Malevich, E. Halliop, A.B. Peppley, G.J. Pharoah, K. Karan, *J. Electrochem. Soc.* 156 (2009)

34. N. Fouquet, C. Doulet, C. Nouillant, G. Dauphin-Tanguy, B. Ould-Bouamama, J. Power Sources 159 (2006).

Chapter 2 Performance and Mass Transport in Open Metallic Element Architecture Fuel Cells at Ultra-High Current Density

This text is originally published in the Journal of Power Sources, referenced as:

Srouji, A. K., Zheng, L. J., Dross R., Turhan, A., Mench, M. M., "Performance and Mass Transport in Open Metallic Element Architecture Fuel Cells at Ultra-High Current Density," Journal of Power Sources, 218 (2012), pp. 341-347.
<http://dx.doi.org/10.1016/j.jpowsour.2012.06.075>

Preface to Chapter 2

This chapter is the preliminary evaluation of performance and mass transport of an open metallic element architecture fuel cell, in comparison to a conventional parallel channel/land design. Electrochemical impedance spectroscopy, oxygen dilution in helium, and net water drag measurements are used to identify the improvements on polarization curves, as a result of the new architecture. The results provide for the first time a fundamental comparative between the two cell designs. New limitations inherent of the OME design are also highlighted.

The work presented in this chapter is part of a collaborative project between the Pennsylvania State University and Nuvera Fuel Cells Inc., and funded by the U.S. Department of Energy.

Abstract

Performance and mass transport of a polymer electrolyte fuel cell (PEFC) with an open metallic element (OME) flow field architecture were analyzed in comparison to a conventional parallel channel/land (C/L) fuel cell, using low humidity at the anode and dry oxidant at the cathode. Under identical conditions the OME cell was able to operate at a current density of 3 A cm^{-2} , recording a peak power of 1.2 W cm^{-2} , compared to 0.9 W cm^{-2} using a parallel cell. Area specific resistance (ASR) was lower for the OME cell as a result of more uniform compression and reduced contact resistance. Electrochemical impedance spectroscopy (EIS) revealed great improvement in mass transport compared to a parallel C/L cell. A heliox mixture at the cathode of both cells revealed improved mass transport for the parallel cell, but revealed no oxygen gas phase transport limitation at high current densities. In fact, it was shown that with an OME architecture, limitation at ultra-high current density results from dehydration at the anode and not reactant mass transport. This also indicates that ionomer film resistances at the electrode do not preclude operation at extremely high currents.

Introduction

The polymer electrolyte fuel cell (PEFC) is a possible alternative to the internal combustion engine for many applications. In the context of clean and sustainable energy, the PEFC is a zero emission technology when using hydrogen gas produced from renewable sources. The majority of automotive manufacturers are engaging in PEFC research and development, and numerous prototype vehicles have already been developed and demonstrated competent performance and range. Market entry is planned in 2015, but reduction in cost below the state-of-the-art system price of 46 \$ kW⁻¹ is still needed [1].

Reactant gases in a fuel cell are distributed over the gas diffusion media (DM) through a flow field, before diffusing to the reaction sites. For functional requirements, the design of a flow field must achieve adequate reactant gas distribution over their respective electrodes, provide pathways for water evacuation from the cell, translate compression from the end plates/bipolar plates to the soft materials layered within, and provide necessary electrical conduction and heat transfer.

A variety of flow field designs are well developed, including parallel, serpentine, and interdigitated (e.g [2-9]). It is important to note that even though different flow field layouts have been developed, they are generally based on a conventional alternating channel/land distribution. Parallel flow fields suffer from uneven gas flow supply and water droplet accumulation, which can result in poor performance at high current or wet conditions. Neutron imaging utilized to quantify liquid water accumulation and distribution in a PEFC showed that locations under lands have restricted mass transport and are preferential liquid storage sites, even in dryer operating conditions [10]. It was also shown

that decreasing the land-to-channel ratio is advantageous in decreasing the water stored in the cell, but could be a drawback when operating in low humidity conditions [11]. Another neutron study revealed that the liquid storage in the gas diffusion layer increased with larger lands [12]. Larger lands create increased distance for transport of products from the electrode, and also add a shadowing effect for reactants diffusing to the electrode. A serpentine layout suffers from relatively higher pressure drop and concentration gradients since the flow path is relatively long. Liquid water has also been shown to accumulate in turns and switchbacks [13, 14], which can harm performance, stability, and durability. The presence of lands introduces a drawback since reactant gas must diffuse under the lands to reach the electrode. At high current density, the land width was found to be the dominant factor for performance. At the same time, large channel spans cause additional ohmic resistance [15], and increase DM intrusion in the channel [16, 17]. The under-compressed DM surface below the channel makes less contact with the catalyst layer [18]. It is also shown that water in low compression interfaces is prone to ice lens formation during operation or storage at subfreezing temperatures, which ultimately causes mechanical damage to the soft materials [19]. Conventional channel/land configurations have also been developed with porous carbon material that acts as an integrated passive wick that removes excess water from the channels and DM [20-22].

The motivation of this study is to understand factors which limit ultra-high current density in fuel cells, so that reduced system cost can ultimately be achieved through higher power density stacks. To help achieve this, a single cell with open metallic element, conceived and designed by Nuvera Fuel Cells (Billerica, MA), with a flow field capable of dramatically increasing limiting current density compared to conventional design, was

tested. The elimination of lands in the flow field is the unique ohmic and mass transport behavior of this architecture. A conventional parallel land/channel fuel cell was used as a comparative reference, in order to better understand the increase in power density observed with the open metallic element design. A set of operating conditions of particular interest to the automotive industry were used in order to operate both cells as shown in Table 1. The results of this study provide a comparison between conventional parallel C/L design and an open metallic element for the first time in literature, and show different origins of performance limitation of the two designs. The experimental work also provides validation data for simultaneous modeling efforts of the open metallic element design [23].

Experimental Setup and Procedure

Two single cells were used in this comparative study. The first cell has a conventional C/L flow field in parallel configuration as shown in Figure 1(a), with an active area of 25 cm². The second cell has an open metallic element acting as flow field and an active area measuring 50 cm², as seen in Figure 1(b). Both cells' flow fields have the same length in the direction of the flow, making the comparison of two different sized cells possible. The anode and cathode reactant flows were operated in a counter-flow arrangement.

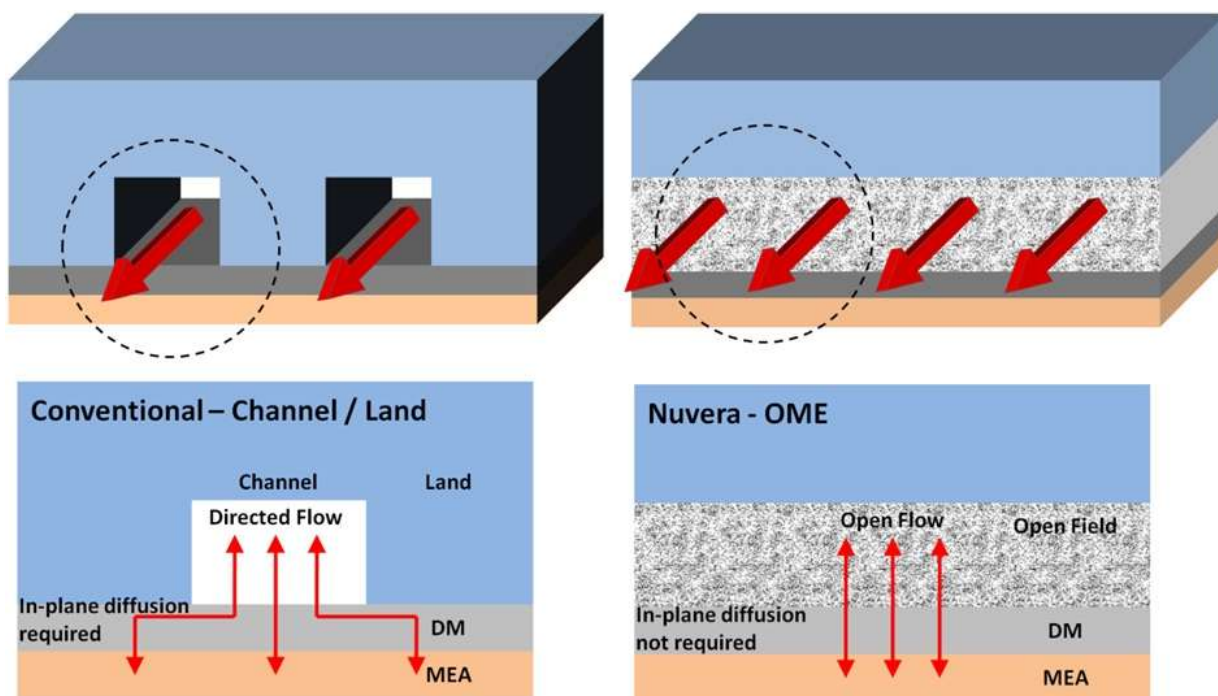


Figure 2-1. a) channel/land, b) open metallic element. (not to scale)

All experiments were conducted using commercial type membrane electrolyte assembly (MEA) composed of an 18 μm (dry) membrane with a catalyst loading of 0.15 mg Pt.cm^{-2} at the anode and 0.4 mg Pt.cm^{-2} at the cathode. The diffusion media (DM) used on both electrodes are Sigracet 25BC by SGL Group (Wiesbaden, Germany), which have a 5% PTFE content and a micro porous layer (MPL) with 23% PTFE content.

An Arbin Instruments (College Station, TX) fuel cell testing station was used for all experiments. The gases were humidified using a standalone membrane-type humidification system from Fuel Cell Technologies Inc. (Albuquerque, NM). Gas inlet pressure was controlled with a backpressure unit from Scribner Associates Inc. (Southern Pine, NC).

Electrochemical impedance spectroscopy (EIS) was performed using a Zahner IM6ex with an external EL300 load, by Zahner Elektrik (Kronach, Germany). The frequency was swept from 100 mHz to 5 kHz using a 20 mV amplitude signal.

Two dew point temperature sensors by Vaisala Inc (Helsinki, Finland) were used to measure the dew point temperatures of the gases exiting the anode and cathode of the OME cell, in order to compute the net water drag coefficient.

The cells temperatures were maintained at 60°C with high flow rate coolant (DI water) from a re-circulating bath for all experiments. Table 1 summarizes the test protocol employed in all experiments unless otherwise specified. The anode side was fed with hydrogen gas at 53% inlet relative humidity (RH), with a constant stoichiometry of 2. The cathode side was fed with dry air or heliox at a stoichiometry increasing from 1.6 to 2 with 0.1 increments as current is increased from 0.25 to 2 A cm^{-2} . The stoichiometry remained 2 for any current density above 2 A cm^{-2} . The same inlet pressure was set on both sides of

the cell by applying backpressure. Inlet pressure was throttled from 118 kPa to 180 kPa (absolute pressure) with increasing current density up to 2 A cm^{-2} . After 2 A cm^{-2} inlet pressure remained constant at 180 kPa. The cell was operated in galvanostatic mode. Each point on the polarization curves shown corresponds to a 45 minutes operation average.

		Anode		Cathode	
Gas		Hydrogen		Air or Heliox (21% O ₂ , Bal. He)	
Relative Humidity		53%		Dry (humidifier bypassed)	
Current density (A cm^{-2})	Stoichiometry	Inlet Pressure (kPa, absolute)		Stoichiometry	Inlet Pressure (kPa, absolute)
0.25	2	118		1.6	118
0.5	2	129		1.7	129
1	2	152		1.8	152
1.5	2	175		1.9	175
2	2	180		2	180
2.5	2	180		2	180
3.0	2	180		2	180

Table 2-1. Fuel cell automotive operating conditions

Results and Discussion

Performance Comparison of Open Metallic Element (OME) and Conventional Design

The performances obtained using the parallel C/L flow field architecture with air at the cathode, are shown in Figure 2, and are well known.

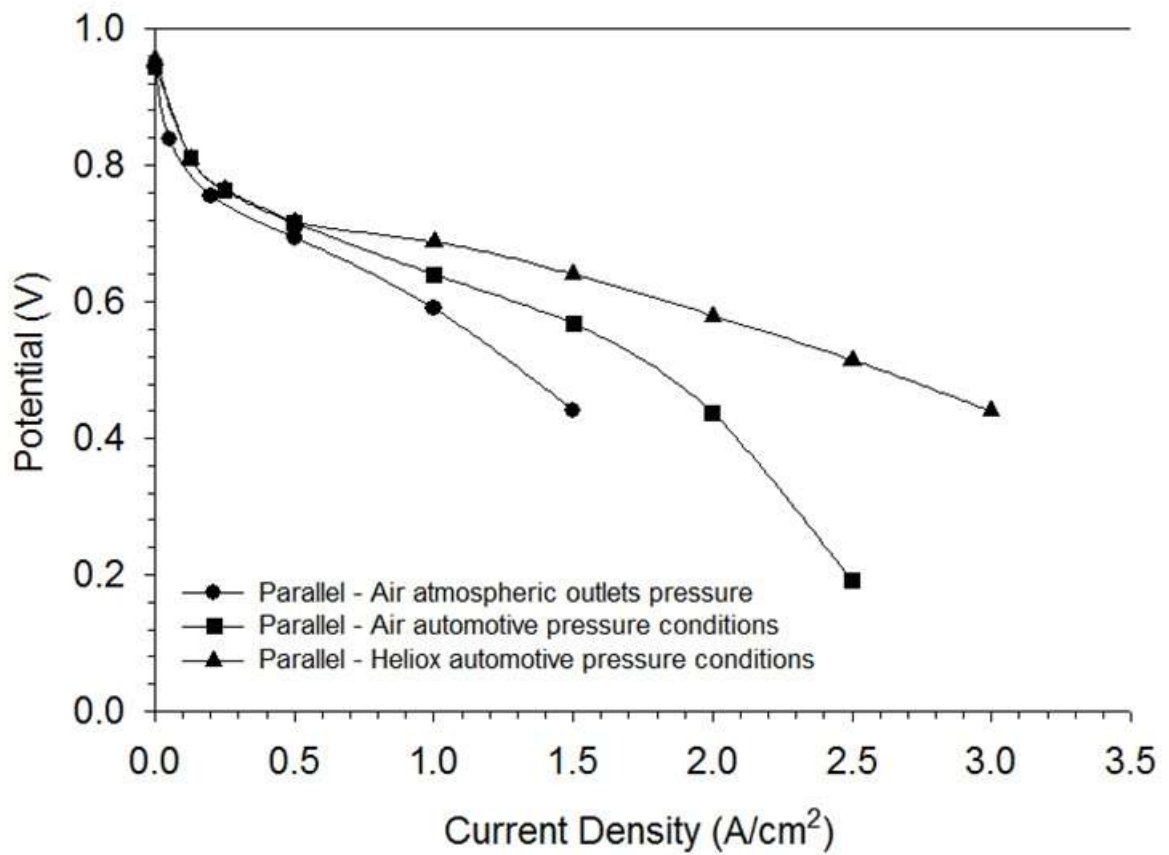


Figure 2-2. Parallel flow field performance at 60°C, under different backpressure and cathode gas dilution. (No backpressure for air, automotive pressure conditions for air, automotive pressure conditions for heliox).

The low pressure (atmospheric pressure at cell outlets) curve represents an ideal for future automotive conditions where parasitic losses are minimized. However, with the existing materials and architecture, these conditions cause performance problems due to increased ionic losses, and high mass transport limitation. The maximum power density achieved does not exceed 0.675 W cm^{-2} , and the cell does not operate stably above 1.5 A cm^{-2} . The conditions utilized for this study, with back pressure on both reactant streams, result in better performance throughout the current density range due to enhanced electrode kinetics and mass transport [24-26]. Concurrently, the cell generates 0.9 W cm^{-2} . However, a sharp decrease in performance is still visible at current densities higher than 1.5 A cm^{-2} , and is generally a result of the mass transport limitations. The conventional designs are inadequate in efficient water removal from the cell components resulting in blockage of reactant diffusion into the reaction sites and causing flooding losses. This is visible in Figure 3, taken with neutron imaging from [27]. Water accumulates under the lands and moves from under the land toward the inner walls of the channel, and therefore retarding the water removal process [27]. The performance curve with heliox at the cathode clearly shows the improvement in mass transport by increasing diffusivity of oxygen into the reaction sites. This performance decrease at the high current region is a significant problem in terms of obtaining high power density, which is a critical parameter in automotive applications in particular.

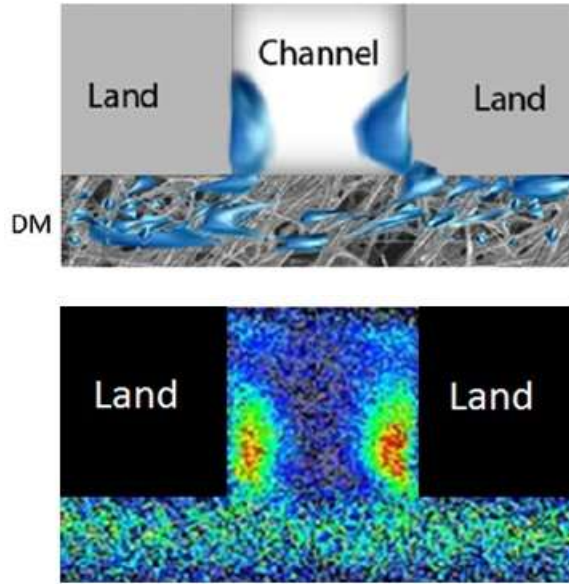


Figure 2-3. a) Water buildup in channel and under the lands of a channel/land cell architecture, b) real-time neutron image of water buildup, reproduced from [27].

The OME design studied here greatly improves the cell performance in the mass limited region while using the same operating conditions. As seen in Figure 4, at the same conditions (air at the cathode, low humidity, and automotive pressure conditions) the open flow field architecture yields a 25% increase in the limiting current density, mainly through better mass transfer.

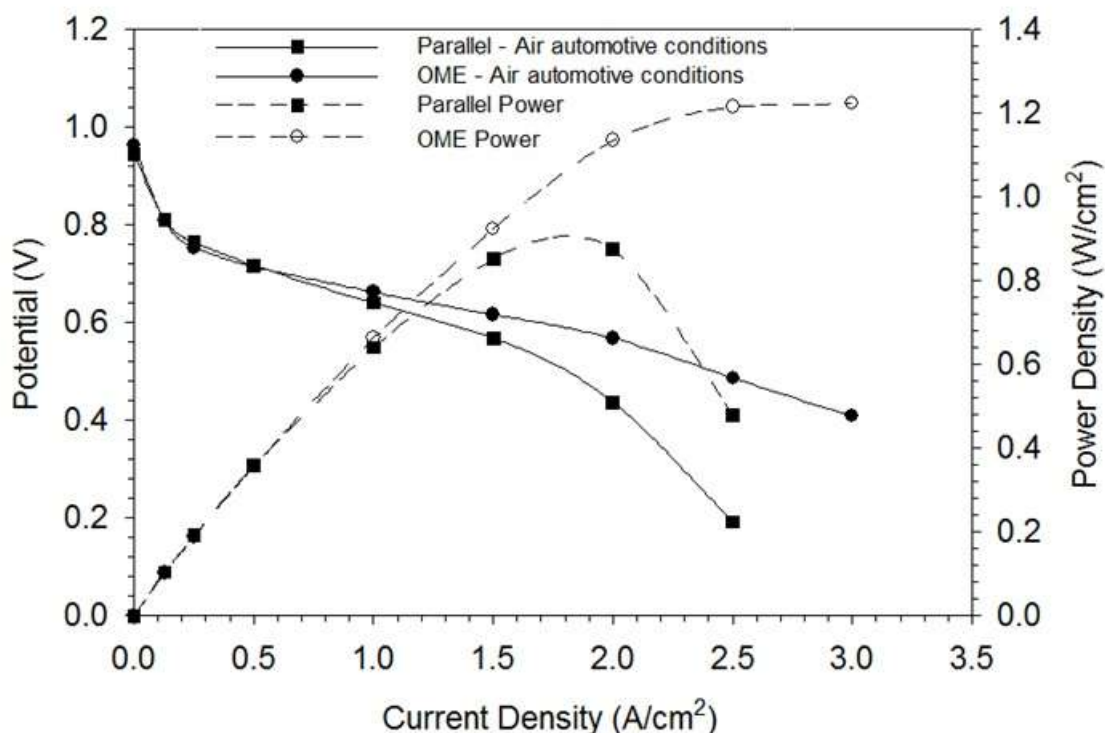


Figure 2-4. Performance comparison between OME and parallel flow field at 60°C, with dry air flow at the cathode using automotive conditions shown in Table 1.

To the author's knowledge, the 3 A cm^{-2} value is the highest reported limiting current density in the literature at reasonable operating voltage in air environments. The OME also results in a reduced ohmic resistance, as seen from the mid-current region. The performance curves for both cells are identical up to 0.5 A cm^{-2} , which is expected since they both use the same MEA, and therefore should have the same kinetic behavior. The most important outcome of the boost in performance is seen by comparing power density curves, where the use of OME successfully eliminated the diminishing return of power density at ultra-high currents. As a result a 33% increase in power density is obtained, from 0.9 W cm^{-2} ($1.6 \text{ W.mg}^{-1}\text{Pt}$) with the parallel channel/land architecture to 1.2 W cm^{-2} ($2.2 \text{ W.mg}^{-1}\text{Pt}$) with the OME. This substantial gain in power density enables higher power

operation, and therefore greatly decreases the size and cost of stacks for automotive application through less use of expensive catalyst and smaller auxiliary components. Peak power values for both cells are summarized in Table 2.

Table 2-2. Peak power of OME and parallel channel/land cells at cell temperature of 60°C using automotive conditions shown in Table 1.

	OME	Parallel channel/land
Peak power density (W cm^{-2})	1.2	0.9
Peak power per catalyst loading ($\text{W.mg}^{-1}\text{Pt}$)	2.2	1.6

The performance improvement with the open flow field is further analyzed by means of area specific resistance (ASR) data for both designs. As seen in Figure 5, the ASR for the open flow field is almost 50% lower than that of the conventional design. The ASR value consists of both the membrane ionic resistance and the contact resistance between the cell components. The lower ASR strongly suggests that more uniform compression, and therefore better contact is achieved with the OME. The iR-free curves of Figure 5 almost overlap in the low and mid-current density regions of both cells (i.e. up to 1.5 A cm^{-2}) as an indication of vastly similar kinetic and mass transport behavior between the two cases in this current region. However, the sharp performance drop observed with the parallel cell

at current densities higher than 1.5 A cm^{-2} is not apparent with the OME. Since the curves are compensated for resistive losses, this enhancement clearly is a result of better mass transport obtained with the OME design.

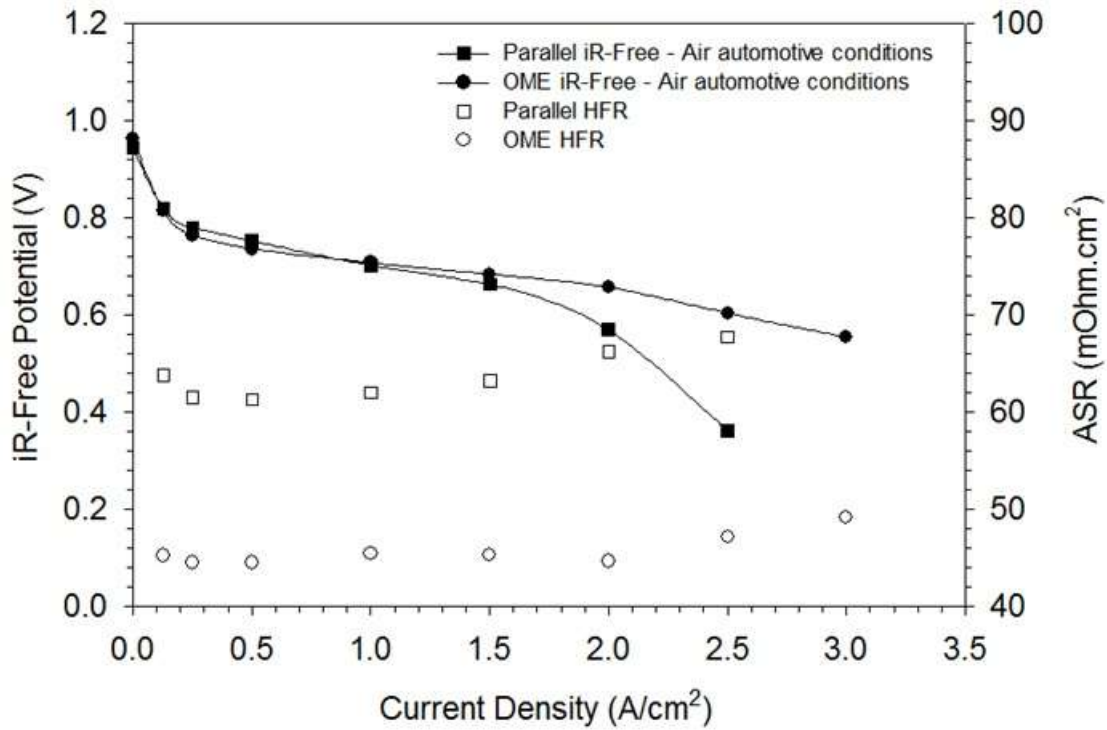
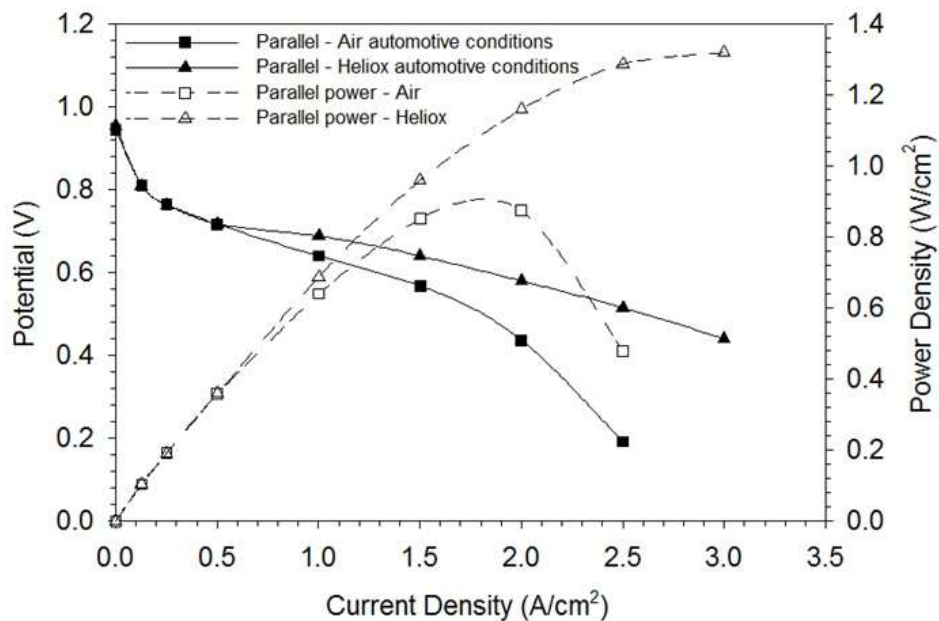


Figure 2-5. IR-Free performance comparison between OME, and parallel flow field, with respective ASR at 60°C and air at the cathode, under automotive conditions.

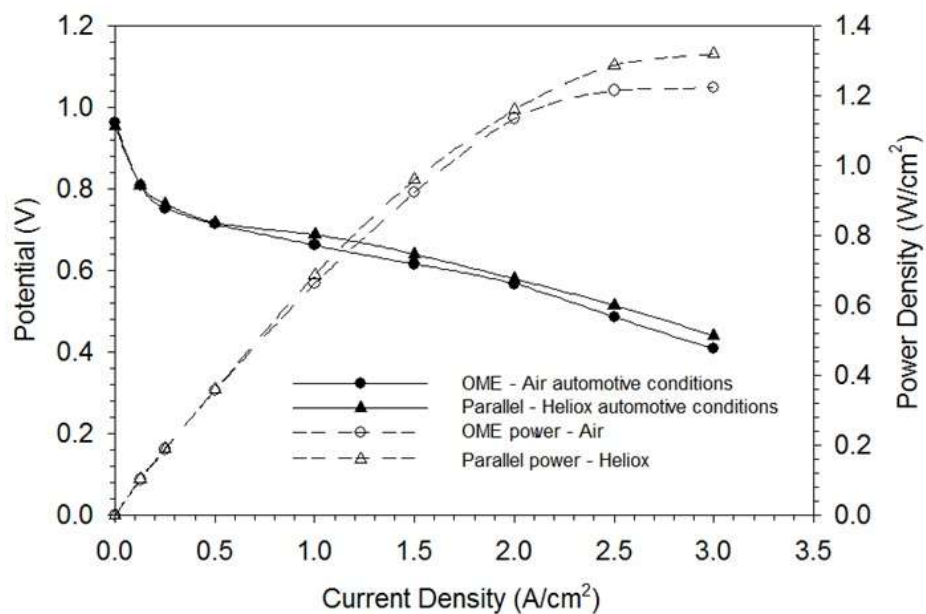
Analysis of mass transport region for OME and parallel flow fields

The considerable gain in performance with the use of OME as a flow field is mainly attributed to the mass transport improvements in the high current density region. In order to investigate the difference at high current density, a heliox mixture containing the same mole fraction of oxygen as that of air (21% O_2 , Bal. He) was fed at the cathode of both cells. At the temperature of 60°C and pressure conditions up to 180 kPa, oxygen diffusivity

in helium gas is 4.1 times higher than in nitrogen, and water vapor diffusivity in helium is 3.8 times higher than in nitrogen [28]. As shown in Figure 6(a), there is noticeable increase in performance when heliox is introduced in the parallel C/L cell. The limiting current density is increased, and the performance curve is now more linear indicative of less mass transport resistance. When this automotive heliox test on the parallel cell is compared with the automotive air performance of the OME, as seen in Figure 6(b), a close match is found.



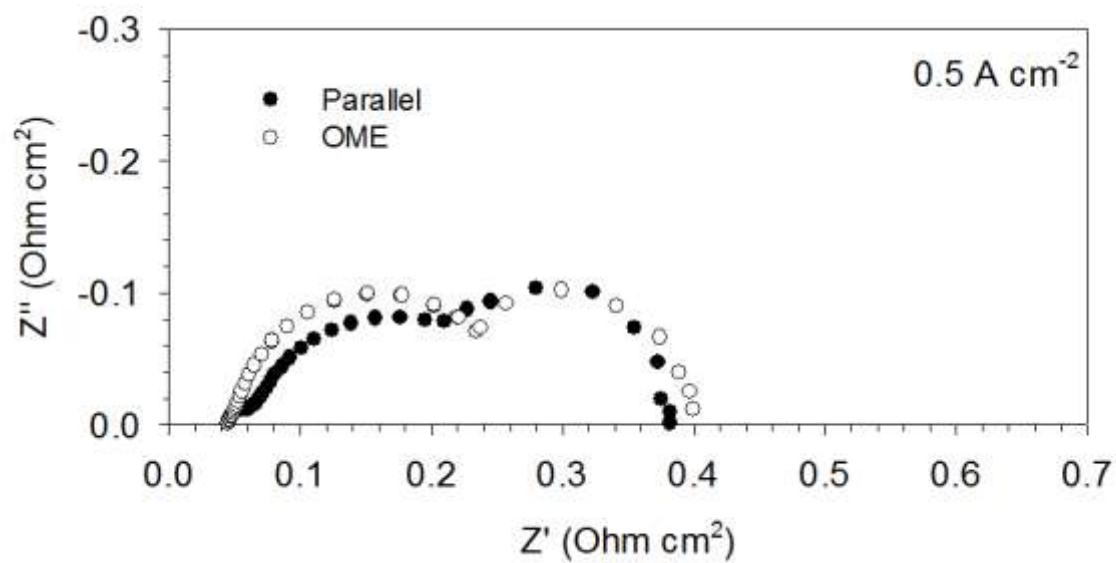
a)



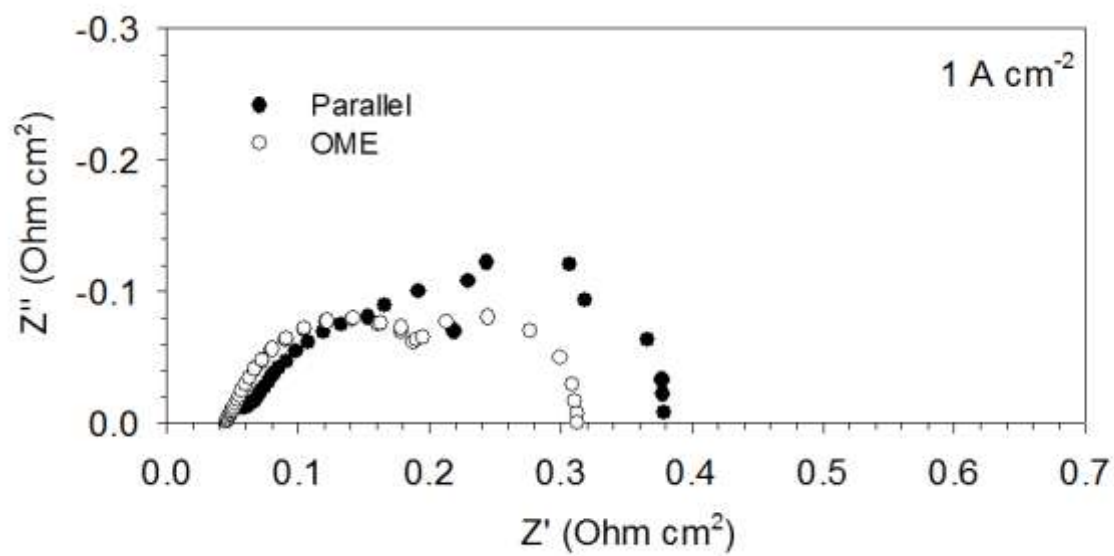
b)

Figure 2-6. Effect of heliox mixture on performance at 60°C with automotive operating conditions: a) Effect on parallel cell b) OME air and parallel heliox.

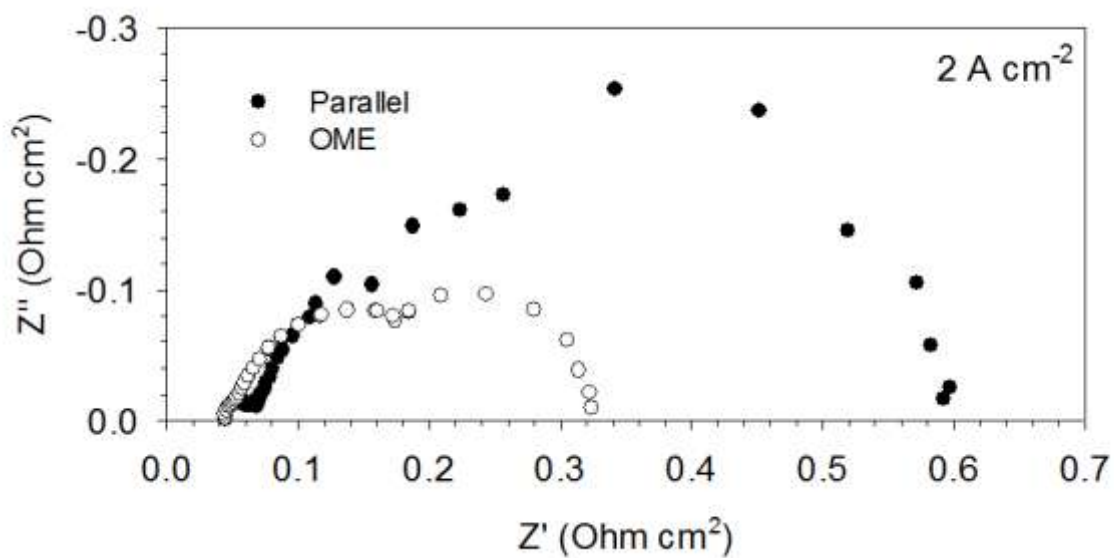
Complete electrochemical impedance spectroscopy (EIS) data for both cells is shown in Nyquist plots of Figure 7. Note that air is used as the oxidant in both cases for the EIS data, and Figure 7(d) is only OME data as it is operating at ultra-high current densities above 2 A cm⁻².



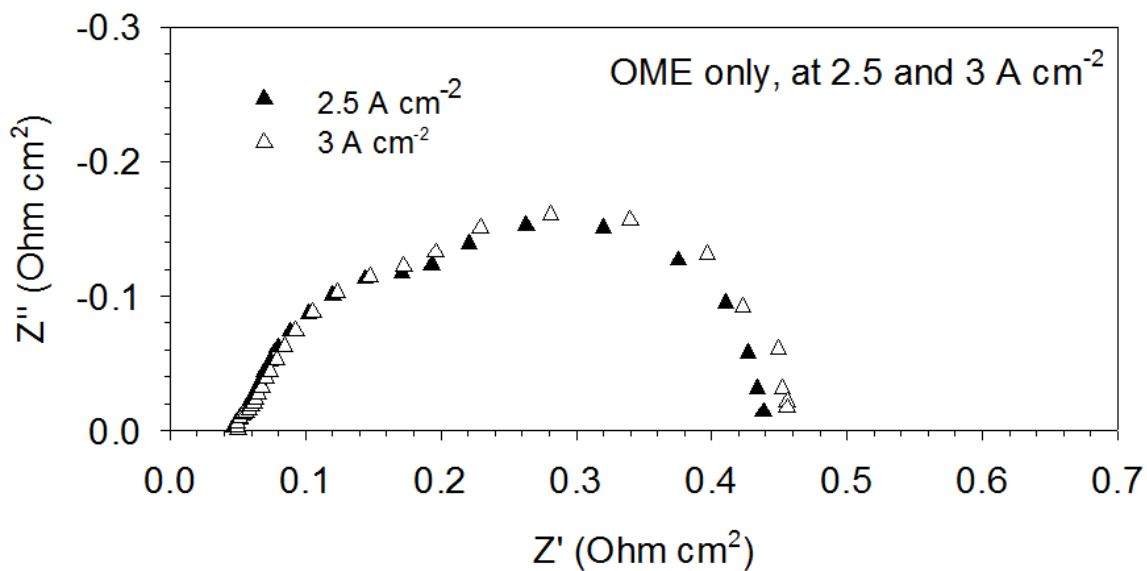
a)



b)



c)



d)

Figure 2-7. Nyquist plot for parallel and OME with air flow at the cathode: a) 0.5 A cm^{-2} , b) 1 A cm^{-2} , c) 2 A cm^{-2} , d) OME only at 2.5 and 3 A cm^{-2} .

The smaller low frequency diameter of the semicircle with the OME suggests lower transport resistance compared to conventional parallel design. The Nyquist plots of Figure 7 were fit to the commonly employed equivalent circuit shown in Figure 8(a) [29, 30]. The medium and low-frequency response arcs are characteristics of cathode charge-transfer and mass-transport processes, and are modeled with a resistor (R_{ct_Cat}) and a finite diffusion Warburg impedance (W_{s1}) respectively, in series. The double layer capacitance for the cathode is represented with a constant phase element (CPE_{Cat}). The real axis (Z') intercept corresponds to the ohmic resistance (R_{ohmic}), which consists of the ionic resistance of the membrane in series with the ohmic resistance of the various layers (catalyst layer, microporous layer, DM, flow field) and their contact resistances. The ohmic resistance is the same resistance mentioned previously as ASR. Deconvolution of the EIS data into charge transfer and mass transport resistances are shown in Figure 8(b) and 8(c), respectively. There is a visible sharp increase in transport resistance with the parallel cell at current densities above 1 A cm^{-2} . The sharp increase is not seen with the OME, and the mass transfer resistance flattens after 1 A cm^{-2} . All these results clearly indicate that the OME design greatly reduces mass transport losses and yields in much higher current and power density.

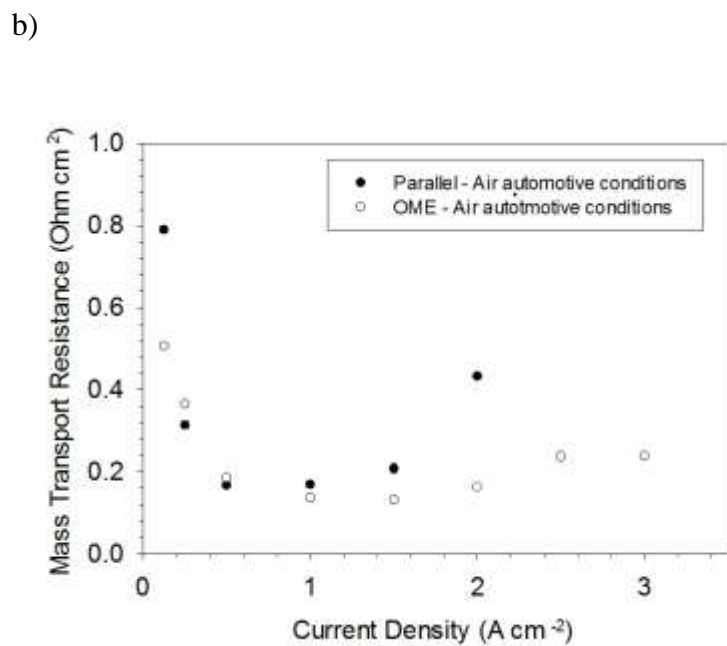
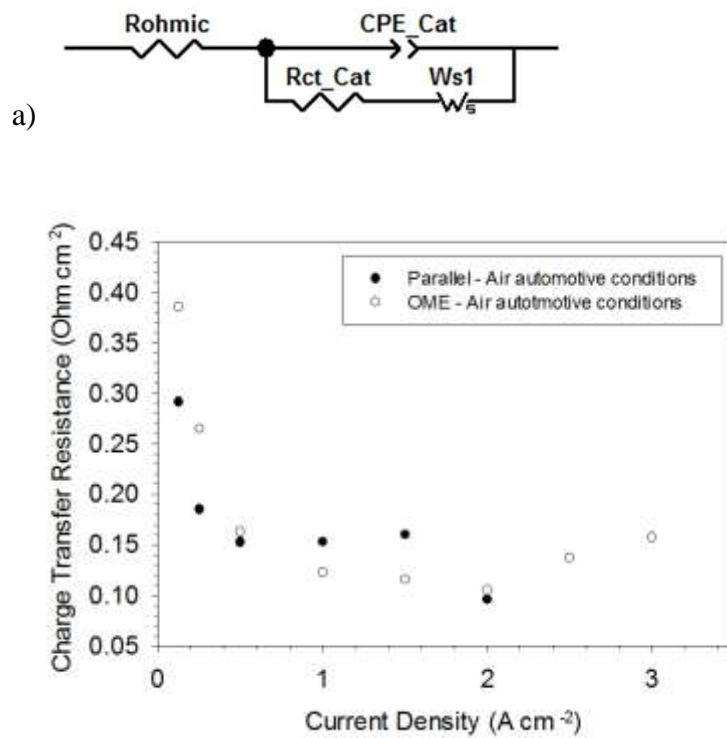


Figure 2-8. a) Equivalent circuit employed to fit impedance spectra, b) charge transfer resistance, c) mass transport resistance; with air flow at the cathode using automotive conditions.

To understand if further improvement in mass transport can be obtained with the OME, heliox was introduced in the cathode of the OME cell under the same automotive conditions. The heliox test on the OME cell resulted in identical performance to the OME cell operating with air at the cathode, except for the limiting current density, as can be seen in Figure 9. The fact that the performance of the open flow field with heliox was not better than air, contrary to what was observed for the parallel cell, means that the transport of reactants in the open flow field architecture is not restricted by the diffusion of oxygen to the reaction sites. Also, this indicates that ionomer film resistances at the electrode do not prevent operation at extremely high currents.

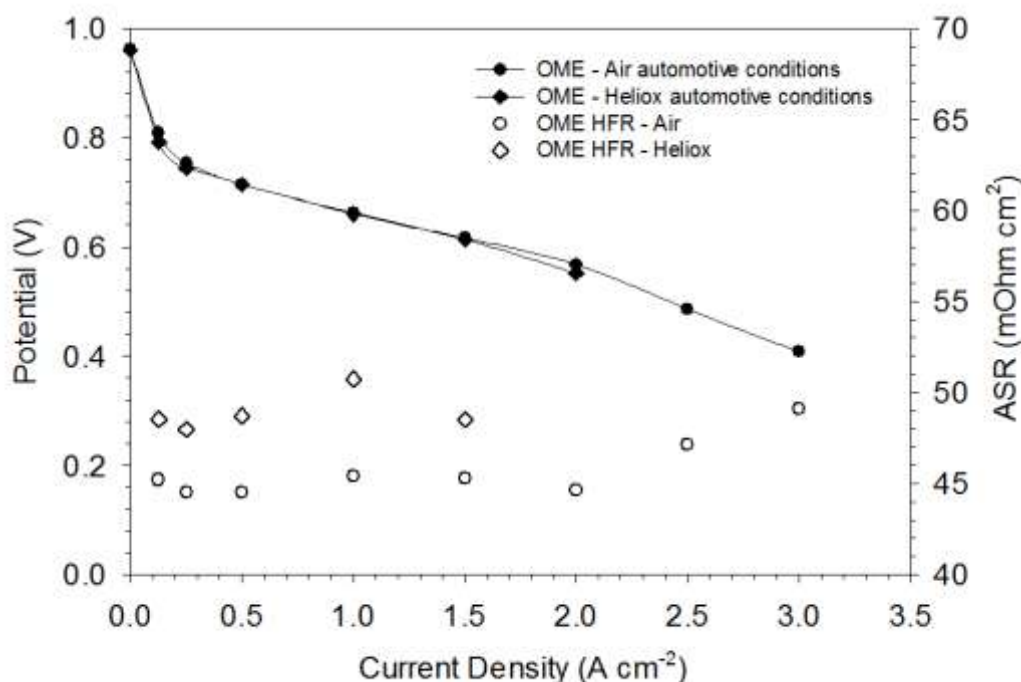


Figure 2-9. Effect of heliox mixture on OME performance at 60°C, using automotive conditions (2 A cm⁻² is not a stable point with Heliox, due to dry-out).

However, limiting current density with heliox was only 2 A cm^{-2} , compared to 3 A cm^{-2} with air. From this observation we deduce that a phenomena different than transport limitation is determining the cell performance in OME at high current density with heliox. As shown in Figure 10, the open flow field cell operating with heliox at a constant current density of 2 A cm^{-2} suffered from gradual voltage drop associated with regular increase in ASR. Heliox improves the diffusivity of oxygen and water vapor at the cathode side. In this case, the faster diffusion of water vapor with heliox caused membrane dry-out by exacerbating the already enhanced diffusion in OME with air flow. In other words, most of the water introduced in the anode side is now removed through the cathode flow with the use of heliox. The results from water balance measurements, as shown in Figure 11, also confirm this behavior by showing a significant increase in net water drag coefficient at high current density with heliox.

Due to the metallic nature of the OME and corrosion reported in previous metallic flow field studies, we have not observed any sign of corrosion after more than 2000 hours of operation between various OME cells. This is attributed to the stability of the elements over our range of operating conditions.

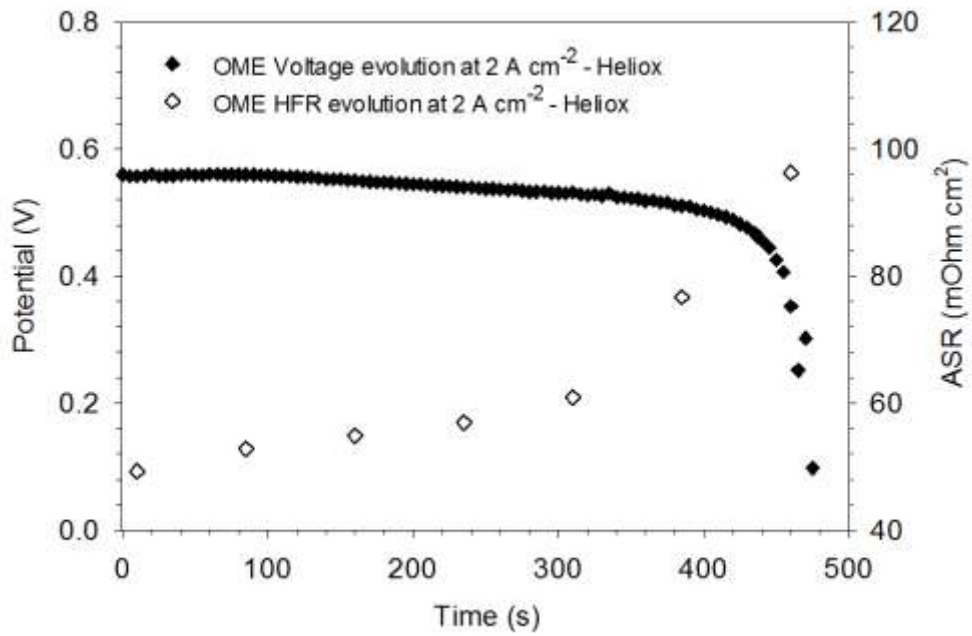


Figure 2-10. Voltage and ASR evolution of OME cell at 2 A cm^{-2} with Heliox flow at the cathode, and a cell temperature of 60°C .

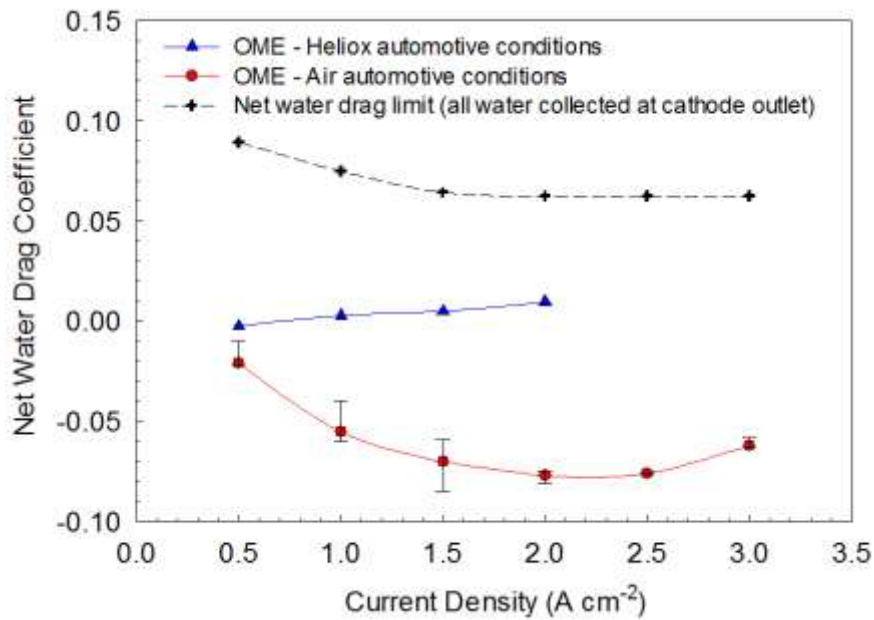


Figure 2-11. Measured net water drag coefficient of OME with air, and OME with heliox using automotive conditions. The computed theoretical limit where all the water is collected at the cathode outlet is also plotted.

Conclusion

A performance comparison between the OME architecture fuel cell capable of ultra-high current density and a conventional parallel channel/land architecture was discussed in this work. A stable peak power of 1.2 W cm^{-2} at a current density of 3 A cm^{-2} was generated using the OME architecture, at a cell operating temperature of 60°C , with low humidity hydrogen at the anode and dry air at the cathode, an improvement of 33% compared to the conventional channel/land design. It was shown that the open flow field architecture improves overall ohmic resistance of the cell through more uniform compression and reduction of contact resistance. The nature of performance improvement through the OME is similar to the boost in performance observed when a heliox mixture is introduced at the cathode of a parallel cell. Mass transport is greatly improved with the OME as the absence of land facilitates and homogenizes water removal, and eliminates the need for in-plane diffusion of the reactants to their specific active electrodes. However, when heliox was used in the OME cell, the combination of the absence of lands and improved water diffusivity in helium limited the current density to 2 A cm^{-2} due to cell dry-out. The limitation at high current density with OME is dry-out due to reduced water retention, and not flooding as commonly observed with conventional C/L flow field. Ionomer film resistances at the electrode do not preclude operation at extremely high currents. Future work will examine in detail the dry-out mechanism at different operating temperatures, and methods for increased water retention with OME.

References

1. DOE hydrogen and fuel cells program record # 11012
2. Li X, Sabir I. Int J Hydrogen Energy. 2005, 30:359-371.
3. Pollegri A, Spaziente PM. US Patent No. 4, 197,178, 1980.
4. Spurrier F, Pierce B, Wright M, US Patent No. 4,631,239, 1986.
5. Granata S, Woodle B, US Patent No. 4,684,582, 1987.
6. Jeon D, Greenway S, Shimpalee S, Van Zee J. Int J Hydrogen Energy. 2008, 33:1052-1066.
7. Hu G, Fan J, Chen S, Liu Y, Cen K. J Power Sources. 2004, 136:1-9.
8. Wang L, Liu H, J Power Sources. 2004, 134:185-196.
9. Cavalca C, Homeyer S, Walsworth E. US Patent No. 5,686,199, 1997.
10. Turhan A, Heller K, Brenizer J, Mench M M. J Power Sources. 2006, 160:1195-1203.
11. Turhan A, Heller K, Brenizer J, Mench M M. J Power Sources. 2008, 180:773-783.
12. Cho K, Mench M M. Int J Hydrogen Energy. 2010, 35:12329-12340.
13. Pekula N, Heller K, Chuang P, Turhan A, Mench M M., Brenizer J, Unlu K. Nuclear Inst Methods Physics Research. 2005, 542:134-141.
14. Trabold T, Owejan J, Jacobson D, Arif M, Huffman P. Int J Heat Mass Transfer. 2006, 49:4712-4720.
15. Goebel S. J Power Sources. 2011, 196:7550-7554.
16. Lai Y, Rapaport P, Ji C, Kumar V. J Power Sources. 2008, 184:120-128.
17. Nitta I, Hottinen T, Himanen O, Mikkola M. J Power Sources. 2007, 171:26-36.
18. Bajpai H, Khandelwal M, Kumbur E, Mench M M. J Power Sources. 2010, 195:4196-4205.

19. He S, Mench M. M. J Electrochem Society. 2006, 153:1724-1731.
20. Litster S, Buie C, Fabian T, Eaton J, Santiago J. J Power Sources. 2007, 154:1049-1058.
21. Yi J, Yang J, King C. American Institute Chemical Eng J. 2004, 50:2594-2603.
22. Weber A, Darling R. J Power Sources. 2007, 168:191-199.
23. Zheng L J, Srouji A K, Turhan A, Mench M M. J Electrochem Soc. 2012, 159:D1.
24. Wang L, Husar A, Zhou T, Liu H. Int J Hydrogen Energy. 2003, 28:1263-1272.
25. Boyer C, Gamburgzev S, Appleby A. J Applied Electrochemistry. 1999, 29:1095-1102.
26. Zhang J, Li H, Zhang J. Electrochemical Soc Trans. 2009, 31:65-76.
27. Turhan A, Kim S, Hatzell M, Mench M M. Electrochim Acta. 2010, 55:2734-2745.
28. Cussler E. Diffusion: mass transfer in fluid systems 2nd ed. Cambridge University Press, 1997.
29. Malevich D, Halliop Ela, Peppley A B, Pharoah G J, Karan K. J. Electrochemical Soc. 2009, 156:B216-B224.
30. Fouquet N, Doulet C, Nouillant C, Dauphin-Tanguy G, Ould-Bouamama B. J Power Sources. 2006, 159:905-913.

Chapter 3 Ultra-High Current Density Water Management in Polymer Electrolyte Fuel Cell with Porous Metallic Flow Field

This text is originally published in the Journal of Power Sources, referenced as:

Srouji, A. K., Zheng, L. J., Dross R., Turhan, A., Mench, M. M., "Ultra-high Current Density Water Management in Polymer Electrolyte Fuel Cell with Porous Metallic Flow Field," Journal of Power Sources 2013, pp. 1-10.
<http://dx.doi.org/10.1016/j.jpowsour.2013.03.145>

Preface to chapter 3

This chapter investigates water management specific to the open metallic architecture operating at high current density. Performance, net water drag, and electrochemical impedance spectroscopy measurements are used simultaneously with varying temperature and RH conditions in order to predict hydration states in the cell. The results are used to determine which fundamental water transport mechanism is limiting cell operation. The dry-out mechanism is described, and compared to the conventional cathode flooding and shutdown.

The work presented in this chapter is part of a collaborative project between the Pennsylvania State University and Nuvera Fuel Cells Inc., and funded by the U.S. Department of Energy.

Abstract

Efficient operation at ultra-high current density (3 A cm^{-2}) with reasonable voltage is possible in a polymer electrolyte fuel cell (PEFC) with a porous open metallic element (OME) flow field due to the dramatic improvement of mass transport through elimination of the conventional channel/land bias. Rather than flooding, improved reactant transport leads to enhanced water removal from the cell and the typical limitation of performance is a result of anode dry-out. In this work, the fundamental water transport mechanisms in the OME PEFC were examined in order to engineer further improved performance and higher temperature operation required for efficient heat rejection. Specifically, the net water drag (NWD) was measured over a range of conditions and analyzed with respect to electrochemical impedance spectroscopy and performance. As the cell operating temperature was increased, the effect of back diffusion was reduced due to the diminishing liquid water content in the cathode catalyst layer, and at critical liquid water content, anode dry-out was triggered primarily through electro-osmotic drag. Addition of cathode humidity was shown to promote high temperature operation mostly due to improved water back diffusion. The same mechanism can be achieved by creating a pressure differential across the membrane, with higher pressure on the cathode side. Stable operation was demonstrated at 90°C using a polymer electrolyte membrane. Real time NWD measurements were recorded during transient anodic dry-out conditions and are consistent with gradual membrane dehydration. The trade-off between liquid water overshadowing cathode catalyst sites and its contribution in promoting back diffusion is identified as a key factor in systems with anode dry-out limited operation.

Introduction

Growing concerns about preserving the environment and finding sustainable sources of energy have brought hydrogen to the forefront of clean energy carriers. Polymer electrolyte fuel cells (PEFCs) are prominent candidates as power generating devices, converting energy stored in hydrogen gas into useable electric power. PEFCs operating on renewable hydrogen are of particular interest to the automotive industry since they are highly efficient, with zero-emissions, and operate at high-power density. The next decade will play a major role in commercializing fuel cell vehicles as most major car manufacturers plan to enter early commercialization by 2015 [1-4]. Continual improvement in performance, cost, and durability is required for successful market implementation.

In PEFCs, the cathode performance is often limiting [5, 6]. This is due to both the slower oxygen reduction reaction (ORR) kinetics at the cathode compared to fast hydrogen oxidation reaction (HOR) at the anode, and mass transport limitation caused by limited oxygen diffusion and liquid water flooding at high current density [5-9]. The conventional bias in the design of fuel cell flow fields using alternating channel/land configuration is a result of the functional requirements of a flow field [10-17]. Channels distribute reactants and remove products, while lands are needed to provide adequate support, compression, and conduction of heat and current.

Various methods for excess water removal have been identified, and can involve modification of different components. Generally speaking, the modification can be in the flow field design, operating parameters, or in the soft materials such as diffusion media (DM), microporous layer (MPL) or catalyst layer (CL). Compared to a conventional

parallel channel/land (C/L) design, a properly designed serpentine flow field at the cathode removes more residual water due to increased pressure drop and enhanced convective forces at the same stoichiometry [18, 19], while an interdigitated flow field forces reactant flow convectively toward the active layer [20]. Modification of the C/L flow field material properties has also been proposed. Hydrophilic treatment of channel walls enhances liquid suction from locations under the land while polytetrafluoroethylene (PTFE) treatment of the C/L interface was demonstrated to increase water storage in the DM and promote flooding [21, 22]. A C/L flow field made of porous carbon was devised to distribute gas in a conventional way and to act as a passive wick for water removal and redistribution of humidity [23]. Component level modifications have also been proposed to mitigate flooding. For example, it was shown that DM with relatively low in-plane gas permeability accounts for a greater amount of liquid water retention under the lands. An increase in PTFE content in the DM and MPL was shown to promote removal of water from the cathode, but an excess amount of PTFE leads to increased electrical contact resistance and reduction in performance [24, 25]. In recent studies, DMs were altered by laser perforation to investigate the effect of structural change on water management [26-28]. Results indicated that perforations acted as water reservoir pools and redistributed water in low humidity conditions. At high current or wet conditions performance was poor. Even though the aforementioned strategies differ, they all deal with conventional architecture fuel cell consisting of alternating channel and lands. As some of them improve water removal and enhance performance, the main limit in typical operation is still due to flooding and mass transport at the cathode, an inherent characteristic of the channel land bias.

Porous metal and metallic mesh fuel distributors have been suggested for direct methanol fuel cells [29-34], and an improvement in performance is noted compared to conventional flow fields caused by improved methanol distribution and CO₂ removal. In PEFC, Kumar et al modeled the performance of a multi-parallel flow field and the effect of filling the rectangular channels with porous metal of different permeability. The addition of porous metal in the rectangular channels leads to improved performance, and more importantly to a more uniform local current distribution. The highest simulated current density was 842 mA cm⁻² [35]. Tsai et al examined the effect of the location of manifolds in a porous metal flow field fuel cell on fuel distribution and concluded that dividing the metal foam into multiple regions and using multiple inlets effectively increases the gas distribution and utilization rate [36].

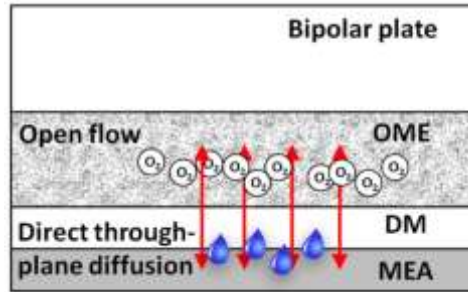
A single cell with an open metallic element (OME), designed and developed by Nuvera Fuel Cells Inc (Billerica, MA), was tested at 60°C in our previous work, and compared to a conventional parallel C/L architecture cell [37-38]. Results showed that mass transport limitation was drastically reduced in the OME cell. No sign of flooding was visible up to 3 A cm⁻². This was attributed to the elimination of conventional lands that usually overshadow electrode active area, trap water inside the cell, and block reactant access to the CL. Unlike an interdigitated flow field, in which through plane convection promotes water removal under land segments, the mode of through plane transport in the OME architecture is diffusion [38]. A cross sectional schematic representing gas and liquid-phase direct flow in an OME architecture cell is presented in Figure 1a.

Part of the water introduced in the humidified reactant streams crosses the membrane electrode assembly (MEA), and contributes to electrolyte-phase hydration. The ORR at the

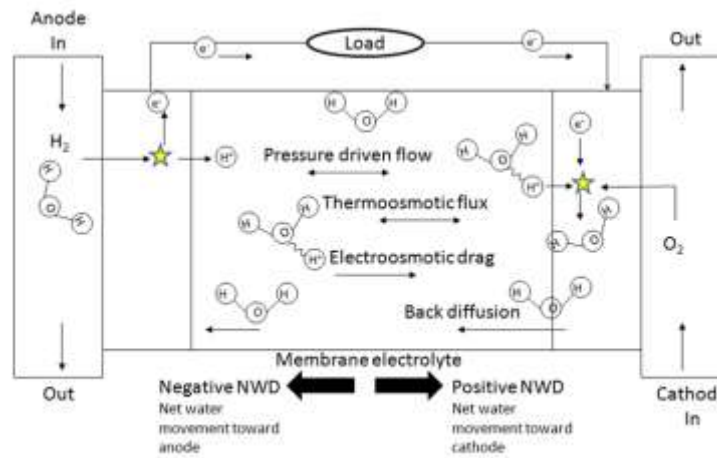
cathode is another source of water. Water is also moved from the anode to the cathode side of the membrane via electroosmotic drag induced by proton transport. This is due to water forming a hydration shell around a proton, or hydrodynamic pumping due to ionic and hydration shell movement [39 - 41]. Because electroosmotic drag affects water management in a fuel cell, it has a local and general contribution to the performance and durability. A local dryout on the anode side of the membrane can be induced by electroosmotic drag. This affects the conductivity of the membrane and therefore increases ohmic resistance and heat generation. Both water generation and electroosmotic drag contribute to water accumulation in the cathode side of the MEA. Even though high water content in the cathode ionomer improves proton transport, the slight excess will result in reduced performance due to flooding and water film resistance over the electrochemically active area. Also, low water content in the ionomer phase of the cathode electrode is detrimental to charge transport and therefore performance. The multiple directions of water transport across the membrane are represented in Figure 1b. The transport of water to the cathode in most cases creates a concentration gradient across the membrane. When the water concentration on the cathode side is high enough, water can move from the cathode toward the anode compartment via back diffusion. The separate measurement and estimation of electroosmosis and diffusion rates are possible [42-46]. Pressure gradients between the two gas compartments (across the membrane) also affect net water transport direction. It has also been demonstrated that temperature gradients across the membrane contribute to the movement of water via thermo-osmosis [47-51]. The combined effect during typical fuel cell operating conditions dictates the overall direction of water transport and potential for anode dry-out, and is referred to as the effective or net water drag

(NWD). NWD is positive for a net flux toward the cathode and negative if the net flux is toward the anode.

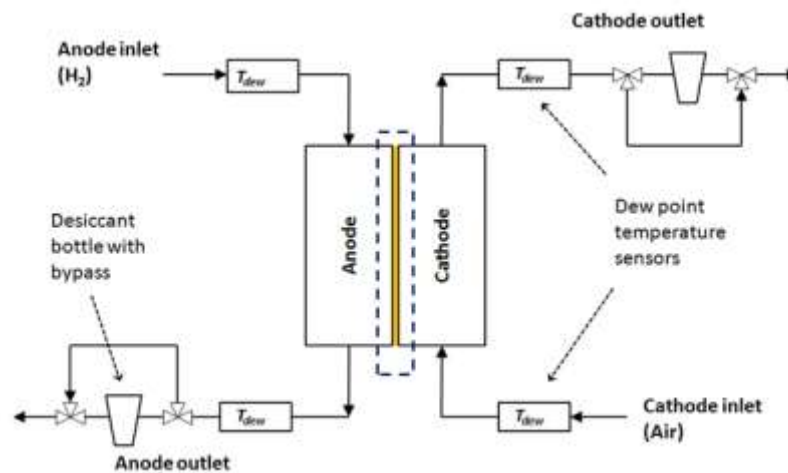
PEFC stack operation at elevated temperature is desirable to reduce heat exchanger size and load. The DOE technical target for the year 2017 requires automotive stacks to operate and reject heat at a specific rate per degree difference between the stack coolant out temperature and ambient temperature ($Q/\Delta T = 1.45 \text{ kW}/^\circ\text{C}$) [52]. Although previous work has shown the OME design can operate at extremely high current at reasonable voltage, it was demonstrated at only 60°C . The motivation of this study is therefore to extend the operating temperature window to higher temperatures suitable for automotive operation [53, 54], while using conventional type polymer electrolyte membrane. In this work, we employ a single cell with open metallic element (OME) designed and built by Nuvera Fuel Cells (Billerica, MA) and investigate the limits of operation and net water drag at ultra-high current density as a function of temperature, to understand the mechanism that limits performance at increased temperature and engineer the system to enable stable high temperature operation up to 90°C . Unlike trying to improve water evacuation in conventional C/L architecture, efforts in improving water retention are addressed for this specific architecture, and stable operation at ultra-high current density.



a.



b.



c.

Figure 3-1. a) cross section of cathode side showing OME and improved mass transport (not to scale), b) through-plane water transport in a PEFC and net water drag (NWD), c) schematic representation of PEFC with in-line dew point temperature sensors and water desiccant bottles for live and average water measurement, respectively.

Experimental

Apparatus

The single cell used in this paper has a porous open metallic element (OME) flow field and an active area of 50 cm^2 . The aspect ratio and boundary conditions are designed to match that of a full size stack cell. The anode and cathode reactant flows are operated in a counter-flow arrangement. All testing was conducted in galvanostatic mode. The membrane electrode assemblies (MEA) used were W. L. Gore, $18 \text{ }\mu\text{m}$ (dry) membrane with a catalyst loading of $0.15 \text{ mg Pt.cm}^{-2}$ at the anode and $0.4 \text{ mg Pt.cm}^{-2}$ at the cathode. The diffusion media (DM) used on both electrodes are Sigracet 25BC by SGL Group (Wiesbaden, Germany), with a 5%wt PTFE content and a micro porous layer (MPL) with 23%wt PTFE content.

An Arbin Instruments (College Station, TX) fuel cell testing station was used to control gas flow rates, back pressure and other operating parameters. The inlet cell pressure is set to desired values by controlling the throttle on the back pressure system. A stand-alone calibrated membrane-type humidification system from Fuel Cell Technologies Inc. (Albuquerque, NM) was used to humidify reactant gases as needed. Electrochemical impedance spectroscopy (EIS) was performed using a Zahner IM6ex, by Zahner Elektrik (Kronach, Germany). The frequency was swept from 100 mHz to 5 kHz using a 50 mV amplitude signal. A schematic of the water measurement apparatus and connections is shown in Figure 1c. Two calibrated dew point temperature sensors by Vaisala Inc (Helsinki, Finland) were used to measure the dew point temperatures of the gases exiting the anode and cathode of the OME cell, in order to compute the real time net water drag

coefficient. Each sensor was followed by a three way valve capable of directing the flow to a desiccant bottle filled with Dryerite[®] (anhydrous CaSO_4 , W.A. Hammond Drierite Co.) to condense and trap water. The cell outlet lines, sensors, and lines leading to each desiccant bottle were overheated in order to avoid any condensation in the lines before trapping the water. After water was trapped, the three way valves were switched to bypass the desiccant bottle. The bottles were then disconnected and the change in mass was recorded and attributed to the amount of trapped water. The measurement for each point with the desiccant bottle lasted between 15 and 20 minutes to maximize signal-to-noise ratio and reduce any error resulting from sporadic emissions of water droplets.

Operating conditions

Operating conditions for polarization curve

The baseline set of conditions used to evaluate a complete polarization curve are summarized in Table 1. The cell baseline operating temperature is 60°C, with ultra high purity hydrogen at the anode, and air (breathing grade D) at the cathode. Constant anode and cathode stoichiometries of 2 were used. The anode inlet relative humidity was 53% (Dew point temperature set at 47°C), and the cathode gas was dry (humidifier bottle bypassed). Back pressure was applied to both anode and cathode outlets such that their inlet pressures were both equal to 180 kPa absolute (1.8 bar absolute or 80 kPa gauge pressure).

Table 3-1. Baseline operating conditions

	Anode	Cathode
Cell operating temperature	60°C	60°C
Gas	Hydrogen	Air
Gas stoichiometry	2	2
Relative Humidity	53%	Dry (humidifier bypassed)
Humidifier dew point temperature	47°C	Dry (humidifier bypassed)
Inlet pressure (kPa, absolute)	180	180

Operating conditions for high current and increased temperature tests

Experiments to study water management as a function of increased operation temperature were all conducted at 2 A cm^{-2} since performance at this point is not limited by mass transport limitations or any dry-out phenomena, and efficiency is still high enough for practical operation. It also satisfies operation at ultra-high current density which is one of the main features of the cell design being investigated [37]. Operation was initiated at 2 A cm^{-2} under baseline conditions from Table 1, at 60°C. Four specific test conditions were utilized as summarized in Table 2. Temperature was increased in steps after one hour of steady state operation, during which ASR, EIS and water measurement were performed. Every operation at a specific temperature lasted at least an hour in order to insure a steady state was achieved if possible. Operation was eventually limited by dryout at a specific temperature. After that, the cell was reconditioned under humid conditions, Baseline operation performance was checked and tests were continued. The first modification to the baseline conditions was the increase of the cathode back pressure, from 180 kPa absolute to 240 kPa absolute, with all other conditions constant. After reconditioning the second modification was the addition of 50% RH to the cathode stream at 240 kPa absolute, with

all other conditions constant. The third modification was the further increase of cathode humidity to 75% RH at the same inlet pressure of 240 kPa absolute. The specified RH at each operating condition was kept constant with increasing cell temperature. This was important, in that the humidifiers' dew points were increased with cell temperature in order to keep a constant relative humidity.

Table 3-2. Operating conditions for increased temperature experiments

	Modification to Baseline	Purpose
Condition 1	Baseline condition (Table 1)	
Condition 2	Increase of cathode inlet pressure from 180 kPa to 240 kPa	A pressure differential is created across the membrane
Condition 3	Increase of cathode humidity from dry to 53% RH, with a cathode inlet pressure of 240 kPa	More water is added to the cathode side via cathode stream humidification
Condition 4	Increase of cathode humidity from 53% RH to 75% RH, with a cathode inlet pressure of 240 kPa.	An excessively humid inlet cathode stream condition is investigated (75% RH)

Net water drag calculation

Net water drag calculation

The net water drag (NWD) is defined as the net amount of water molecules transferred across the membrane, from anode to cathode, per proton transferred:

$$C_{NWD} = \frac{\dot{n}_{H_2O}^{in,an} - \dot{n}_{H_2O}^{out,an}}{iA/F} \quad (1)$$

Therefore, a positive NWD implies an overall water transport from the anode to the cathode. This means electro-osmotic drag dominates transport in the absence of pressure or temperature gradient effects. A negative NWD means the net water movement direction is from the cathode toward the anode, and back diffusion dominates, in the absence of pressure or temperature gradient effects. The NWD directions are labeled in Figure 1b.

Desiccant method

The average NWD was measured by condensing and collecting the water at the anode outlet. For repeatability, it is highly recommended to condense and collect the water at the cathode outlet as well. That way the NWD is measured and the water mass conservation equation is verified. Therefore for each measurement, the cell outlet streams were condensed and trapped in separate desiccant bottles filled with Dryerite[®] (anhydrous CaSO₄, W.A. Hammond Drierite Co.). The change in bottle mass due to the condensed water was recorded. For the conservation of mass, the amount of water coming in the cell with the gas streams and the amount of water generated during the experiment should be equal to the amount of water collected at the anode and cathode outlets according to

$$m_{H_2O}^{in,an} + m_{H_2O}^{in,cat} + m_{H_2O}^{gen} = m_{H_2O}^{out,an} + m_{H_2O}^{out,cat} \quad (2)$$

Where the mass of water generated during the measurement is simply

$$m_{H_2O}^{gen} = (iA/2F) \cdot M_{H_2O} \cdot \Delta t \quad (3)$$

The galvanostatic operation insures that the rate of water generation is constant and well known. Using the desiccant method, the net water drag coefficient is computed from

$$C_{NWD} = \frac{m_{H_2O}^{in,an} - m_{H_2O}^{out,an}}{(iA/F) \cdot M_{H_2O} \cdot \Delta t} \quad (4)$$

In all data recorded and presented here, the experimental deviation from the steady state conservation of mass was less than 5%, indicating a true steady state had been achieved and storage/depletion terms were insignificant during measurement

Real time dew point sensors method

With careful heating of dew point sensors and exit lines, water condensation is prevented and the dew point sensors can be used to compute an instantaneous or average net water drag coefficient. Using the dew point temperature reading at the anode outlet the saturation pressure of the stream can be calculated, and therefore the real-time anode outlet water flow rate can be shown as:

$$\dot{n}_{H_2O}^{out,an} = (\lambda_{H_2} - 1) \frac{iA}{2F} \frac{P_{sat}(T_{dew_anOut})}{(P - P_{sat}(T_{dew_anOut}))} \quad (5)$$

Similarly, the inlet water vapor flow rate at the anode is calculated, since the anode inlet dew point is an input defined for the experiment and delivered by the calibrated humidification system:

$$\dot{n}_{H_2O}^{in,an} = \lambda_{H_2} \frac{iA}{2F} \frac{P_{sat}(T_{dew_anIn})}{(P - P_{sat}(T_{dew_anIn}))} \quad (6)$$

The net water drag coefficient from the sensor readings is therefore computed by plugging Eq. 5 and 6 into Eq. 1. The water amount at the cathode outlet can be computed in a similar fashion to verify that mass is conserved.

Results and Discussion

The performance curve introduced under baseline conditions is at a cell temperature of 60°C. After steady operation at 2 A cm⁻² established, the cell temperature was increased in steps while adjusting the dew point to keep the required RH constant. Operation at each temperature lasted for more than 45 minutes in order to ensure steady state in performance and water transport and storage, as verified by performance and water balance measurements. After steady state operation, water was collected with the desiccant bottles for around 20 minutes, while the dew point sensors were recording the real time water measurement. After water collection, EIS was performed. The same was repeated after each temperature step until cell operation was not possible due to dry-out. The same experiments at 2 A cm⁻² were performed under each operating condition shown in Table 2.

Baseline performance curve

Figure 2 shows the baseline condition performance curve with the corresponding area specific resistance (ASR). The cell temperature is maintained at 60°C while the hydrogen gas is humidified to 53%, and the cathode inlet is dry. Both anode and cathode sides are pressurized to 180 kPa absolute at the inlet, so the pressure gradient across the membrane is considered negligible. The performance curve at low and medium current densities is typical, with a kinetic drop at very low current densities and an ohmic region characterized by a constant slope at medium current density (1 – 1.5 A cm⁻²). The performance curve does not have an inflection point at high current densities to represent non-linear mass transport loss as commonly observed in channel/land cells [37]. At current densities above

2 A cm⁻², the performance curves seems to slightly change slope. This is simultaneous with the linear increase in ASR recorded after 2 A cm⁻². The ASR is almost constant below 2 A cm⁻². At 2 A cm⁻² it is slightly lower (44 mOhm cm²) than other values and this is attributed to sufficient membrane hydration due to water generation at 2 A cm⁻², with the dominance of back diffusion. The increase in ASR after 2 A cm⁻² is due to the dominance of electro-osmotic and thermo-osmotic [38] drag at such high current densities, which contribute in partially drying out the membrane. At 3 A cm⁻² ASR is increased to around 50 mOhm cm⁻². A current density of 2 A cm⁻² was chosen for temperature step testing since the performance at this point is not limited by mass transport limitations or any dry-out phenomena, and efficiency is still high enough for practical operation.

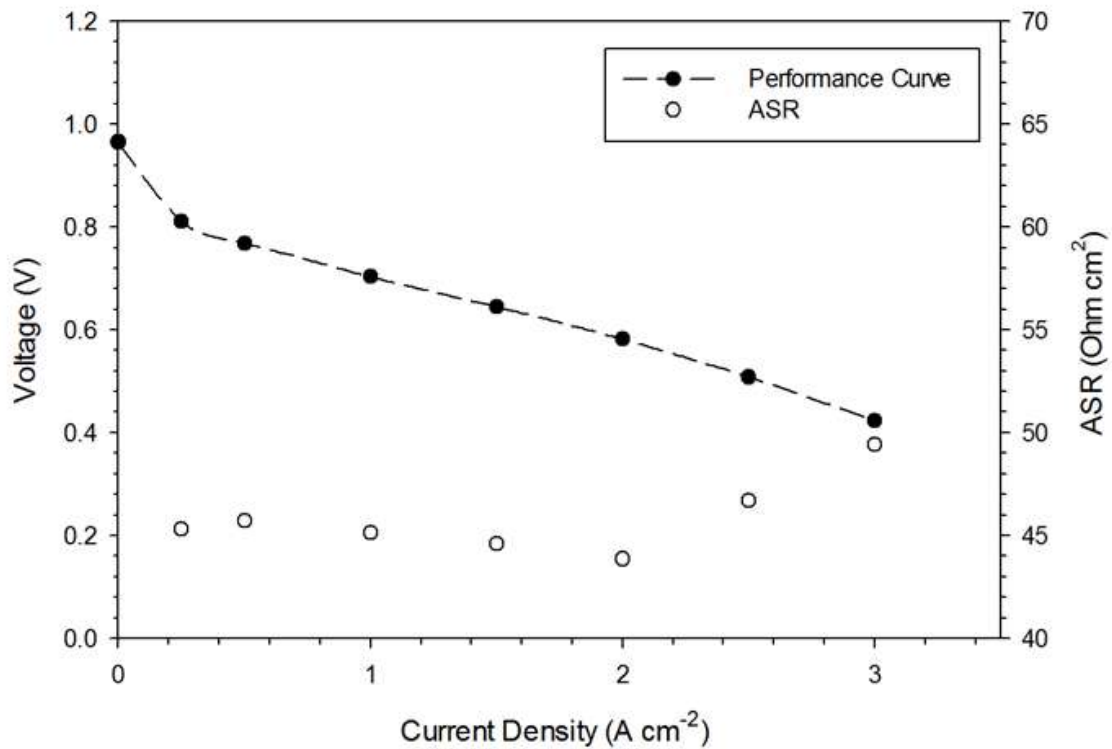


Figure 3-2. Performance curve and ASR for baseline conditions at a cell temperature of 60°C.

Exploring high temperature operation – dry cathode inlet and cathode pressure effect

Two testing conditions have a dry cathode inlet: The baseline condition with a cathode inlet pressure of 180 kPa, and Condition 2 which varies from the baseline conditions by the increase of cathode inlet pressure to 240 kPa, therefore creating a pressure differential across the membrane.

Temperature was increased in steps at 2 A cm^{-2} , as shown in Figure 3. Under baseline Condition 1, the highest achieved stable operating temperature at 2 A cm^{-2} was 65°C . The voltage increases from around 570 mV to a little above 590 mV, as the temperature goes from 60 to 65°C . Looking at the NWD in Figure 4, we observe that at 60°C the NWD has a negative value. As the temperature is increased, the NWD becomes less negative and a change in sign of NWD occurs at an intermediate temperature between 62.5 and 65°C . This means that as the experiment started at 60°C , the overall net direction of water was back to the anode and dominated by back diffusion. As the temperature increased, the direction of net water transport changed toward the cathode. Also, at the temperature of 65°C it is clear that the net water direction is from the anode toward the cathode. No data are shown at a temperature higher than 65°C because the cell could not operate in steady state at 67.5°C . As previously discussed, Condition 2 is the same as the baseline condition except for an increase of cathode pressure from 180 kPa to 240 kPa to create a pressure differential across the membrane, favoring transport to the anode. The voltage under Condition 2 is also plotted as a function of temperature on Figure 3. The voltage under Condition 2 is higher than the voltage of the baseline condition, as expected due to the increase of pressure at the cathode. Although the baseline condition did not operate above 65°C , Condition 2 operates stably at the temperature of 72.5°C . Voltage increased as

temperature increased and peaked at 70 °C. Then it dropped at 72.5 °C, yet remained stable, whereas there was no stable operation at 75 °C. As seen from Figure 4, the NWD for Condition 2 is almost a perfect negative offset of the NWD from the baseline condition, which is expected due to the linear relationship between pressure differential and convective flux [55]. The more negative NWD reveals that the creation of the pressure differential across the membrane forced more water back from the cathode toward the anode, keeping the membrane hydrated to a higher temperature. An effective permeability of use for models can be computed using Eq. (7) in order to describe the negative offset due to the pressure differential:

$$Q = \frac{-KA}{\mu} \frac{\Delta P}{L} \quad (7)$$

Q , A , and μ represent the flow rate, cross-sectional area of flow, and viscosity of water respectively. $\Delta P/L$ is the pressure gradient across the membrane having thickness L . K is the effective Darcy permeability. The flow rate Q , can directly be calculated from Eq. (8), and then converted from mol s⁻¹ to m³ s⁻¹ for consistency:

$$Q = (NWD_{Cond_2} - NWD_{Cond_1}) \frac{iA}{F} \quad (8)$$

The computed effective permeability values at each temperature are shown in Table 3, and clearly indicate a linear offset due to the pressure gradient. The effective in-situ permeability averages at 3.64 x 10⁻²⁰ m², which is consistent to the range of values found in literature (between 10⁻²⁰ and 10⁻¹⁸ m²) [56, 57].

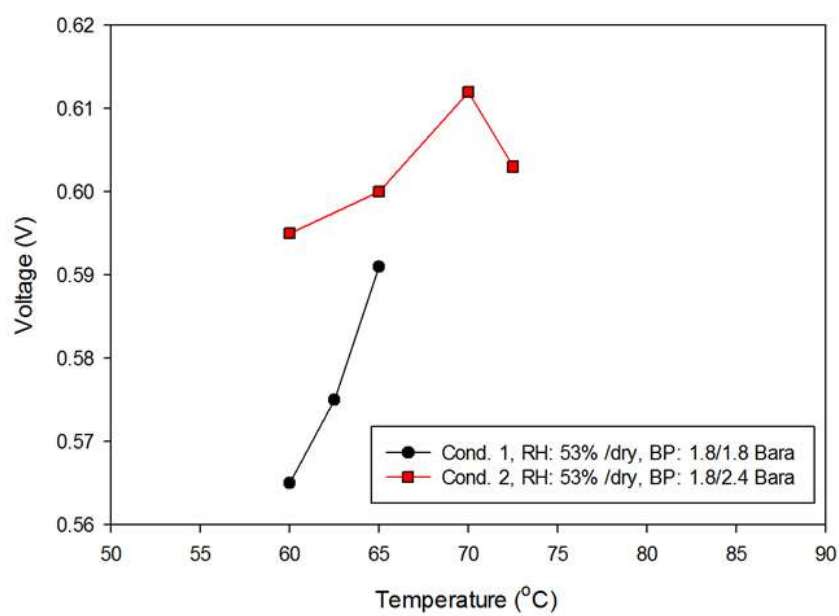


Figure 3-3. Cell voltage as a function of temperature with baseline condition 1, and condition 2, at 2 A cm^{-2} .

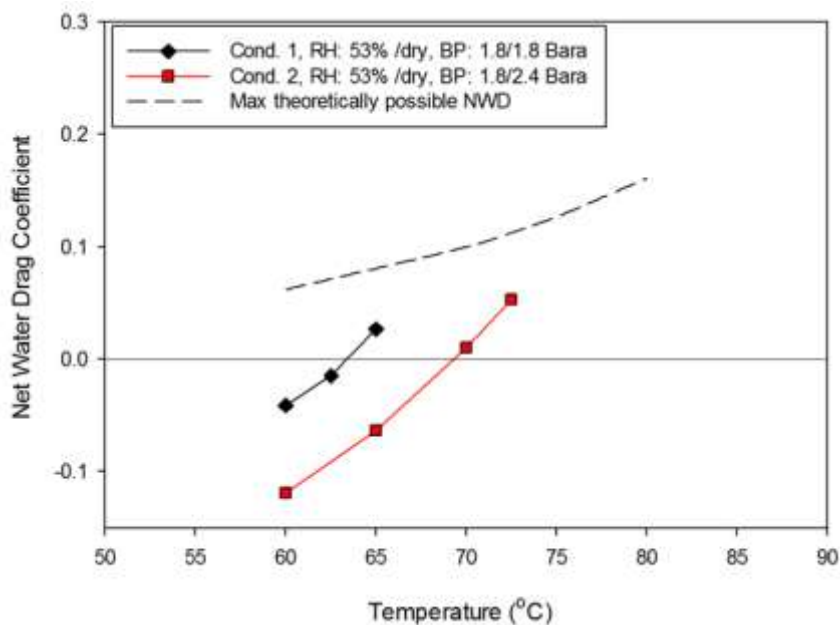


Figure 3-4. NWD coefficient evolution as a function of temperature with baseline Condition 1, and Condition 2, at 2 A cm⁻².

Table 3-3. Calculated effective water permeability for a pressure differential of 60 kPa

Temperature (°C)	Effective hydraulic permeability k (m ²)
60	3.46×10^{-20}
62.5	3.42×10^{-20}
65	4.04×10^{-20}
Average: $3.64 \times 10^{-20} \pm 9\%$	

As temperature increased, the NWD also increased and became less negative, where it eventually changed sign and became slightly positive at the cell temperature of 70° C. At this point, the operation was stable and performance was at peak value. Further increase in temperature elevated the NWD to a more positive value, resulting in anode-dryout and unstable performance.

Figure 5 represents the transient voltage, ASR and NWD evolution when the temperature reached 67.5 °C under the baseline Condition 1. The voltage gradually decreases over a period of less than 7 minutes until there is no stable operation and the cell shuts down. Simultaneously, the ASR gradually increased. The initial ASR is 48 mOhm cm² and the final ASR is 104 mOhm cm² right before cell shutdown. The voltage drop with simultaneous ASR increase is a clear indication of membrane dry out. Also on Figure 5, the evolution of real time NWD reveals an increasingly positive NWD with time evolution concurrent to the voltage drop and ASR increase. This indicates that with time, at 67.5 °C and baseline Condition 1, less water is exiting from the anode outlet side of the cell, since the anode inlet is a constant value. An increasing anodic dry out is the reason for gradual voltage drop. The same is true for Condition 2 at 75 °C. Impedance spectra for baseline Condition 1 and Condition 2 are plotted in Nyquist format in Figure 6. The common electric circuit analogy used to deconvolute charge transfer resistances, ASR and mass transport is shown in Figure 6c [58, 59]. ASR and charge transfer resistance deconvoluted from the impedance spectra are shown in Figure 7 for the different temperatures at 2 A cm⁻². For baseline Condition 1, as temperature increases, there is no change in ASR until 65 °C. The charge transfer resistance gradually decreases as temperature increases. This is also clearly observed in the reduction of charge transfer arc diameter in Figure 6a. Even though ASR increased as temperature increased from 62.5 to 65 °C, this did not significantly reduce the cell voltage. The cell voltage is more likely to have increased due to the reduction of charge transfer resistance or improved transport, which is already an indication that even though stable operation was limited by membrane conductivity, the performance was dominated by another mechanism. The emphasis on the charge transfer

resistance in the interpretation of the results comes from the fact that the slight change in water content in the catalyst layer is usually recorded in the high frequency arc as well. This is due to water coverage of catalytic sites or dehydration of ionomers in the case where water content is low in the cathode catalyst layer. The sensitivity of the cell operation to the water content in the catalyst layer is a result of the OME design not limited by mass transport in the flow field or DM. This is due to low water saturation of 0.2 in the DM, as previously explored [37, 38] attributed to improved water removal by the OME design, through elimination of conventional lands. This makes the low frequency arc (mass transport) less sensitive to changes in water content since water sites that block oxygen transport are minimal in the GDL and the flow field.

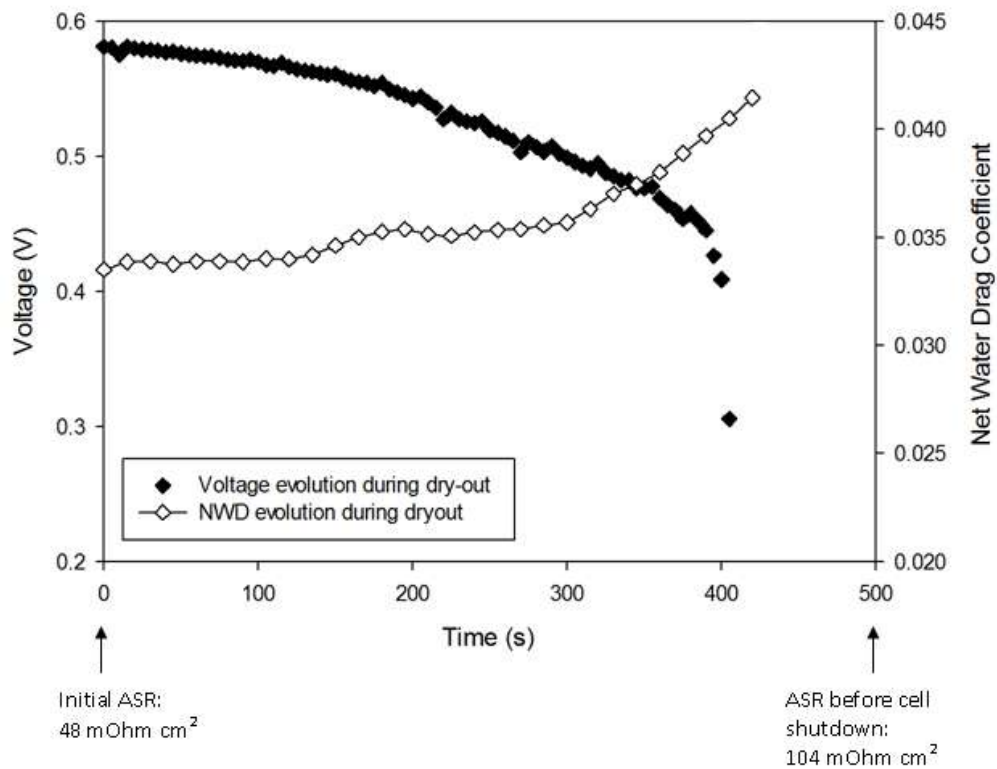
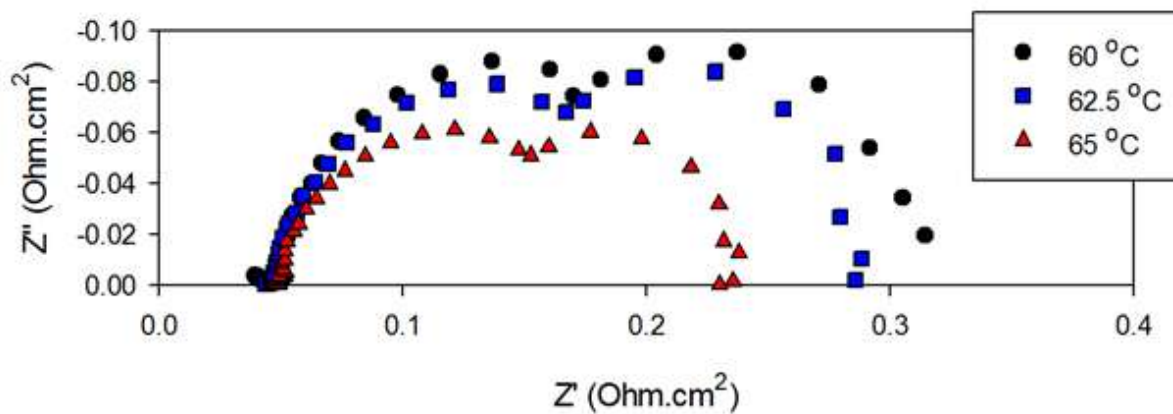
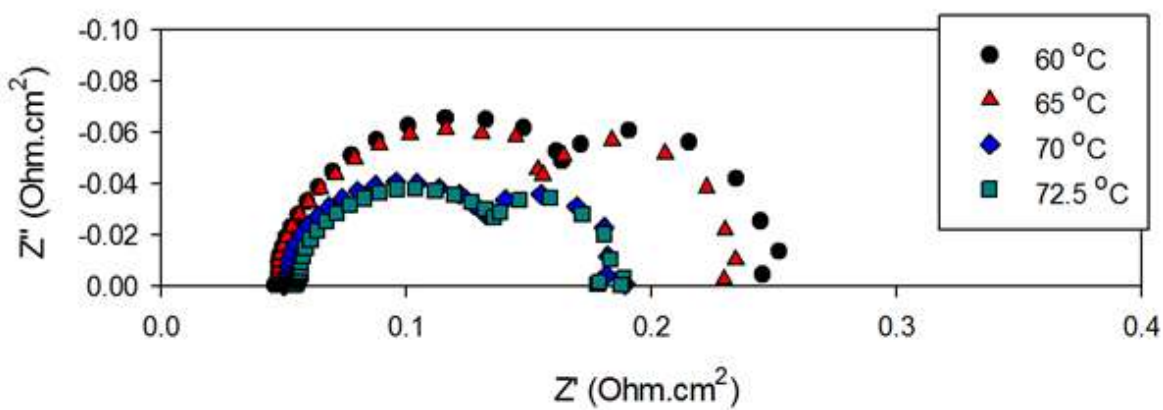


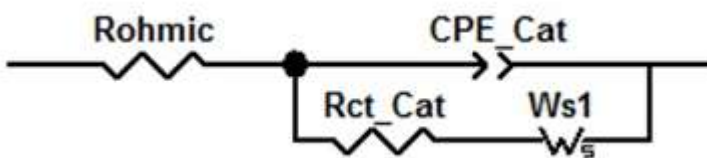
Figure 3-5. evolution of voltage, NWD and ASR during transient dry-out that leads to shut down of operation at 67.5 °C with baseline condition, at 2 A cm⁻².



a)



b)



c)

Figure 3-6. a) Nyquist plot for Baseline condition 1, b) Nyquist plot for Condition 2, c) electric circuit model used for EIS data fit.

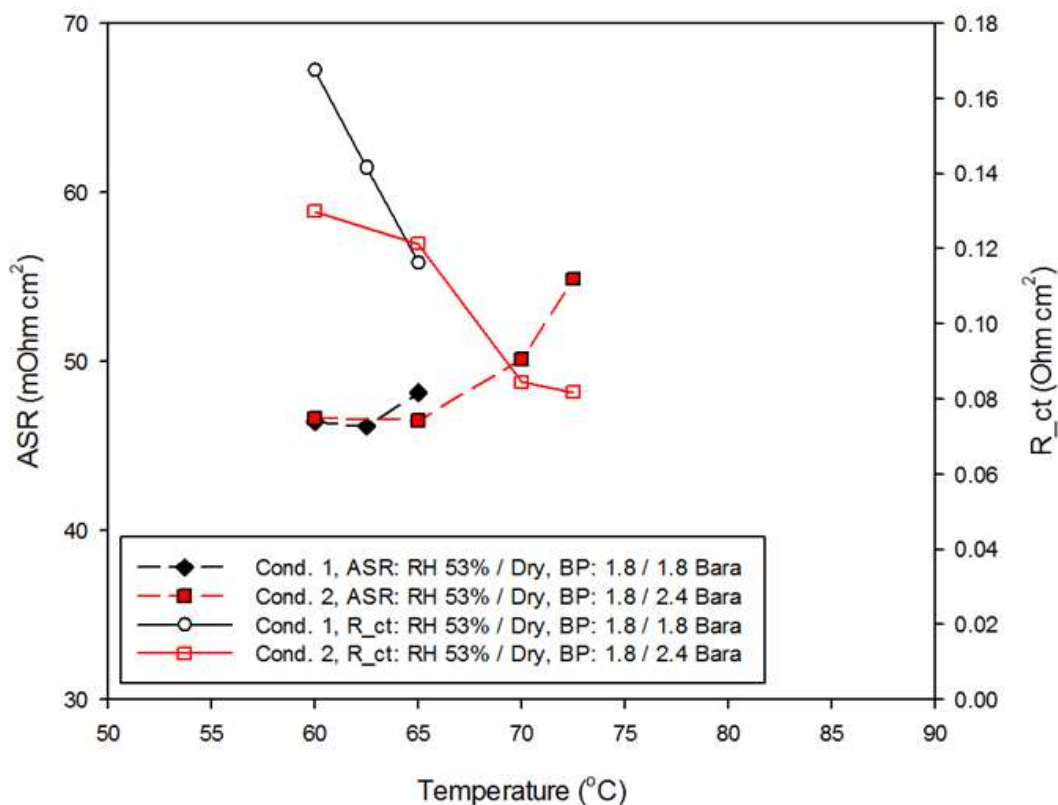


Figure 3-7. Charge transfer resistance and ASR data from EIS, for Baseline Condition 1, and condition 2, at 2 A cm^{-2} .

The impedance spectra of Condition 2 are plotted in Figure 6b, and the deconvoluted charge transfer resistance and ASR are plotted on Figure 7 along those of baseline condition previously discussed. The ASR trend as a function of temperature is very similar to the one observed for the baseline Condition 1. As the cell temperature increased from 60 to 65 °C, there was no change in ASR. Then as temperature increased from 65 to 72.5 °C, ASR gradually increased. Both Conditions 1 and 2 show a flat ASR followed by a gradual increase. Charge transfer resistance for Condition 2 decreases with increasing cell temperature and almost reaches a plateau. The decrease is small from 60 to 65 °C relative

to the decrease in charge transfer resistance from 65 to 70 °C. This is also shown in the slight change in charge transfer arc diameter in Figure 6b from 60 to 65 °C, followed by a more significant drop in arc dimension between 65 and 70 °C. The increase in ASR is also seen on the Nyquist plot by a shift in the real axis intercept to higher values. We also note that the peak performance at 70 °C corresponds to a slightly positive NWD. The same observation made for the baseline condition can be made for Condition 2 in regard of performance and ASR. There is an increase in performance from 65 to 70 °C even though ASR indicates that the membrane became dryer with increased temperature. Therefore, it is not the membrane hydration that dominates performance over this temperature range, but the state of the catalyst as observed by the behavior of the charge transfer resistance. The mechanism and physics that describe this change in charge transfer resistance are investigated and interpreted in the next section.

Exploring high temperature operation – effect of cathode humidity

Condition 3 varies from Condition 2 only in the increased humidification of the cathode inlet stream to 53% RH. The pressure gradient across the membrane is the same as Condition 2. The voltage evolution with temperature for Condition 3 is plotted in Figure 8. Voltage increases from 60 °C to 75 °C and peaks at 75 °C. Voltage decreases after 75°C but stable operation is possible up to a temperature of 80°C due to a combined effect of cathode flow humidification and favorable pressure gradient toward the anode. The voltage of Condition 3 is lower when compared to Condition 2, partially due to reduced oxygen mole fraction, and the effect of added humidity on the catalyst layer. Nevertheless operation for Condition 3 is possible at a higher temperature. Even though there is a reduction in gas phase oxygen mole fraction from Condition 2 to Condition 3 due to the

added humidity, Eq. 9 can be used to evaluate the impact of reduced oxygen mole fraction on overpotential [60].

$$V_{Cond_3} - V_{Cond_2} = \frac{R_u}{F} [T_{Cond_3} \ln(C_{O_2,3}) - T_{Cond_2} \ln(C_{O_2,2})] \quad (9)$$

Using Eq. 9, the voltage drop calculated, due to the reduced mole fraction of oxygen with the introduction of humidity at the cathode in Condition 3 is expected to be around 2 mV. However, the measured voltage drop varies between 8 mV and 16 mV as shown in Figure 8. We attribute the additional loss to increased catalyst layer coverage from water with the introduction of humidity.

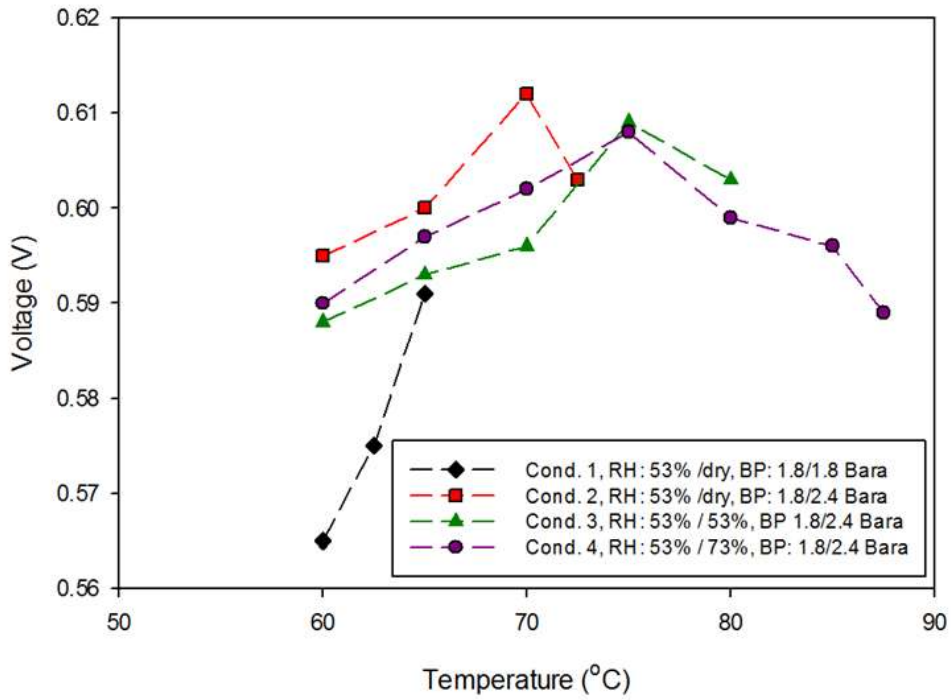


Figure 3-8. Cell voltage as a function of temperature under all measured conditions, at 2 A cm⁻².

The NWD coefficient is shown in Figure 9 and the Nyquist plots from EIS are shown in Figure 10. The NWD in Figure 9 confirms that the reason for increased maximum temperature operation is a more negative NWD. This is also shown in the the ASR trend in Figure 11. ASR as a function of temperature in Condition 3 exhibits the same trend as the previous conditions, but the ASR remains constant over a broader temperature range before increasing due to loss of water in the membrane. The charge transfer resistances are shown in Figure 11. Charge transfer resistances with the humidified cathode are higher than charge transfer resistances of Condition 2 with a dry cathode. There is also an increase in mass transport resistance in Condition 3 compared to Condition 2, as shown in Figure 12.

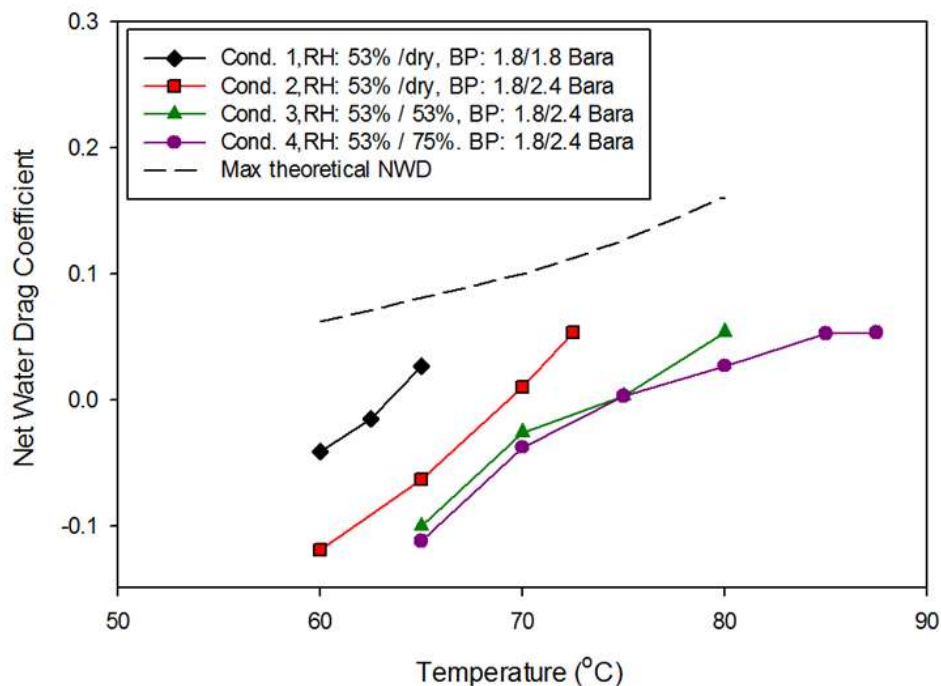
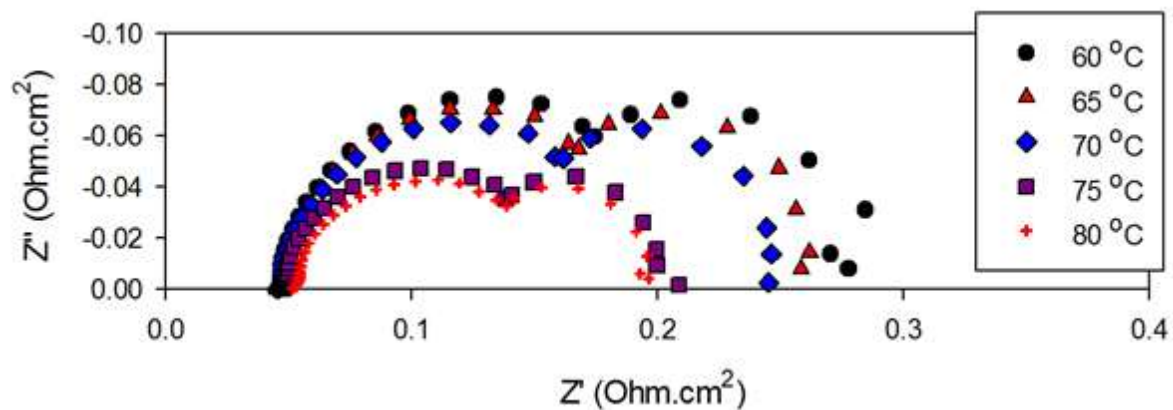
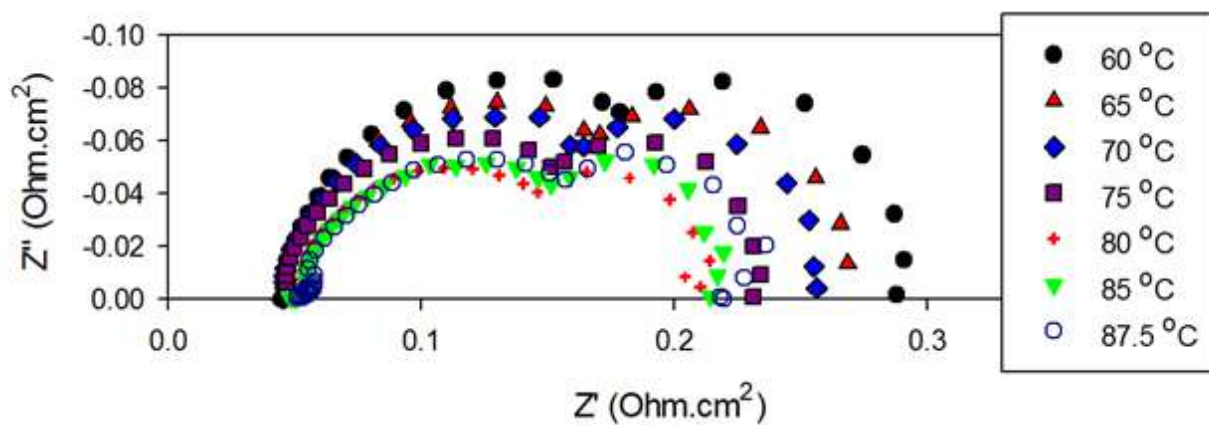


Figure 3-9. NWD coefficient as a function of temperature under all measured conditions.



a.



b.

Figure 3-10. a) Nyquist plot for Condition 3, b) Nyquist plot for Condition 4.

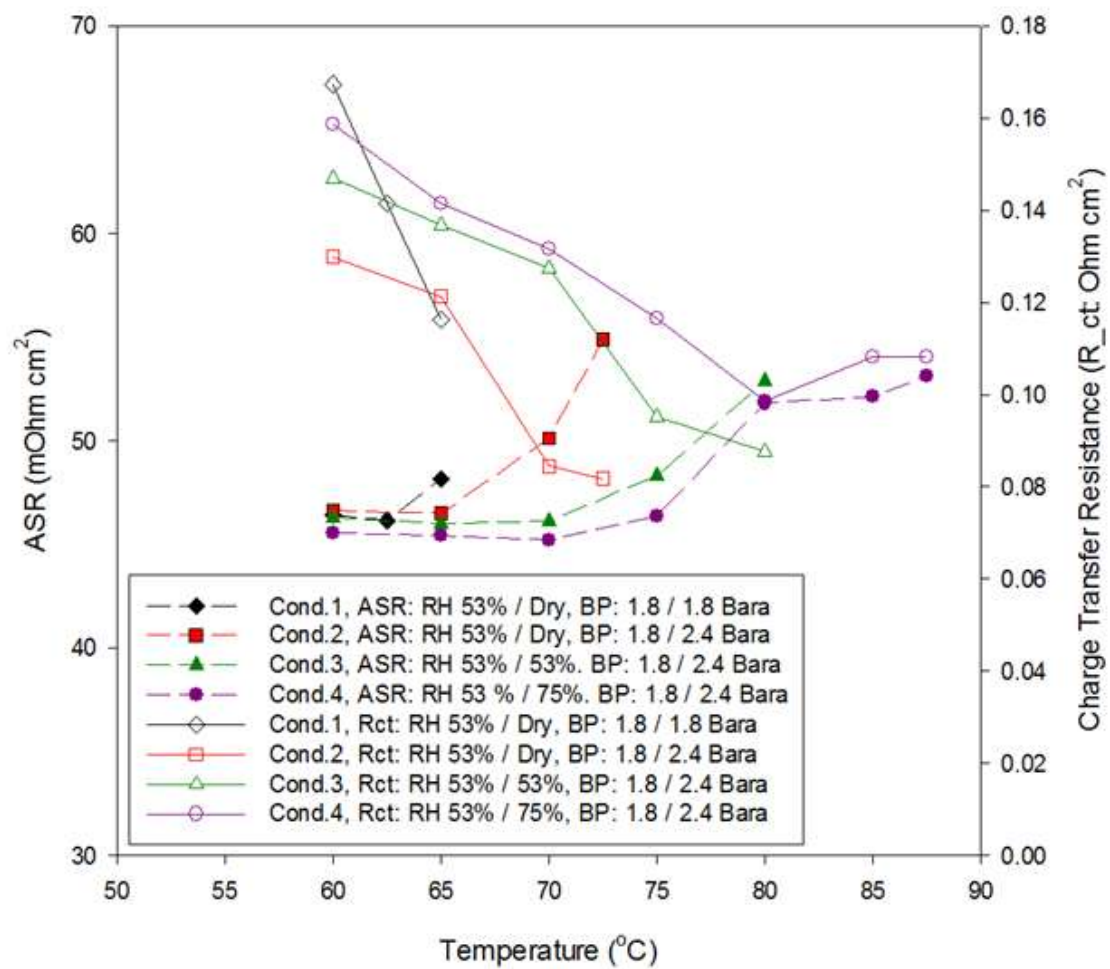


Figure 3-11. Charge transfer resistance and ASR data from EIS, for all measured conditions, at 2 A cm⁻².

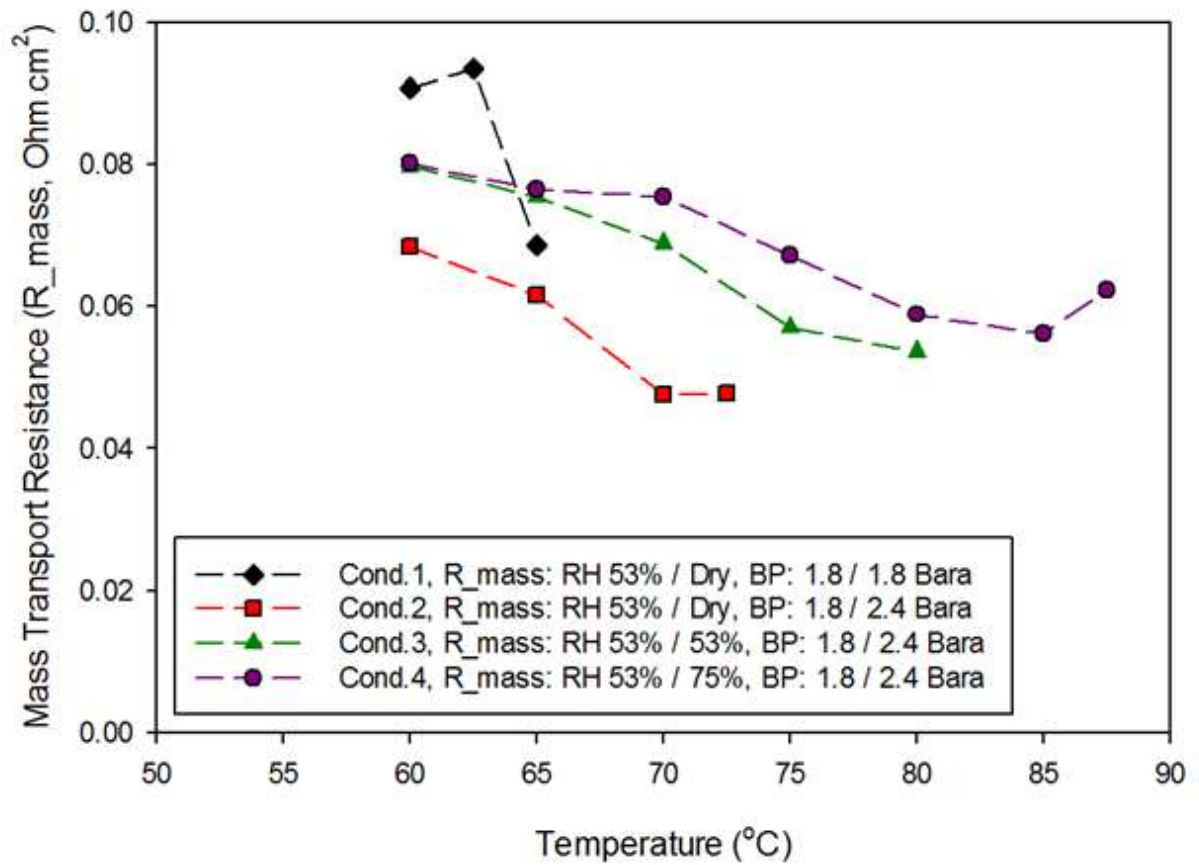


Figure 3-12. Calculated mass transport resistances for all measured conditions deduced from EIS data, at 2 A cm^{-2} .

For Condition 3, we also notice that the peak voltage corresponds to a slightly positive net water drag coefficient and to an ASR value that is higher than the minimum. This again shows that at the maximum stable operating temperature limit is determined by membrane hydration but the performance here is limited at the catalyst level.

Condition 4 varies from Condition 3 by the increase of the cathode inlet RH from 53% to 75%. The voltage evolution with respect to increasing temperature is very similar to what was observed in Condition 3. The peak voltage also occurs at the cell temperature of 75°C ,

with an overall voltage trend at 2 A/cm^2 that is slightly higher than that of Condition 3. The voltage in Condition 4 remains lower than that of Condition 2 with a dry cathode. The explanation is the same as the one given in the previous section. A 75% RH cathode inlet increased water in the catalyst layer compared to the dry cathode in Condition 2. In fact, the higher the water content at the cathode inlet, the higher the charge transfer resistance, as shown in Figure 11. The increased mass transport resistance in Figure 12 is a clear indication that the increase in charge transfer observed is due to an increase in the water on the catalyst layer. Interestingly, the voltage in Condition 4 is higher than the one observed with Condition 3, even though we see that more water obstructed catalyst activity. The reduced oxygen mole fraction with increased humidity in Condition 4 can only contribute to reduced voltage. Therefore, the increased performance could be partially attributed to better membrane humidification from increase water availability. The ASR values are lowest with a 75% RH, as seen in Figure 11. This could explain the improved performance compared to a 53% RH cathode inlet humidity. The peak voltage also occurs at a slightly positive NWD as seen in Figure 9, with a slightly elevated ASR value compared to the minimum.

Proposed water mechanism continuum between NWD and performance during dry-out

One can speculate that the maximum performance at a slightly elevated ASR observed is a result of the competition between localized flooding and ionomer dehydration in the catalyst layer (CL). For Conditions 2, 3, and 4, an increase in voltage is visible with increasing temperature, until a peak is reached. This occurred simultaneously with the observed monotonic decrease in charge transfer resistance with increasing temperature,

until a drop in charge transfer resistance to a plateau was observed at the temperature for which the highest voltage was recorded at a specific condition. The ASR trend was also consistent, with a flat ASR as a function of temperature followed by a monotonic increase in ASR at the temperature with the highest voltage and lowest charge transfer resistance for a specific conditions set. This increase in ASR also corresponds to the change in NWD direction from anode to cathode. The impact of water addition at the cathode on the charge transfer resistance and mass transport behavior indicates that the phenomenon observed is likely water accumulation in the catalyst layer. The addition of more water (75% RH) increased the charge and mass transport resistances but pushed more water back to the anode and therefore increased membrane hydration at higher temperatures. Figure 13a is a simplified, not to scale schematic the cathode catalyst layer in agglomerate form next to the membrane. At low temperatures, the high charge transfer resistance due to an excess of liquid water content in the catalyst layer is sketched in Figure 13b. Excess liquid water in the catalyst layer is the cause of the observed reduced electrochemically active area and increased oxygen diffusion effective resistance. This also provides a negative NWD through enhanced back diffusion, as also shown in Figure 13 by the arrows. The concentration of liquid water in the cathode catalyst layer is high enough to promote back diffusion and therefore keep a low ASR value. As the temperature increases, the fraction of liquid water in the cathode catalyst layer is reduced as represented in Figure 13c. More catalyst active area is cleared therefore the charge transfer resistance is reduced, mass transport is improved for oxygen, and performance has increased. This same reduction in liquid water content results in a lower back diffusion and therefore a less negative NWD, represented by the smaller arrow. NWD is still negative at this point and provides

enhanced membrane hydration, as shown by the flat ASR with the initial increase in temperature under a specific operating condition. As temperature is increased, the liquid water fraction in the cathode catalyst layer is further reduced to the point where most catalytic active areas are cleared, and the hydration is optimal. There is a correct amount of liquid water to keep the ionomer of the cathode catalyst layer hydrated and highly conductive to ions, with minimal excess water is present to block the active sites and hinder oxygen permeation. This optimal cathode catalyst hydration is observed with the abrupt drop in charge transfer resistance at a specific temperature and a peak in the performance. The NWD at this condition is slightly positive, and beyond this critical value, anode dry-out is initiated.

As inlet humidity is increased at the cathode, the drop in charge transfer resistance (the transition from Figure 13c to Figure 13d) occurs at a more elevated temperature. This is another indication that the kinetic activity at the cathode catalyst layer that is being interpreted through charge transfer deconvolution from EIS data. At this critical cathode catalyst hydration, the liquid water concentration is not high enough to promote back diffusion of liquid water from the cathode to the membrane. Therefore the net water movement becomes from the anode to the cathode as observed by the measured positive NWD and indicated by the direction of the arrows in Figure 13d. This triggers the increase in ASR due to anodic dry-out that is now dominated by electro-osmotic drag due to reduced back diffusion. As temperature is further increased, electro-osmotic drag leads to anodic dehydration to a point where operation is not possible, due to the very high electric resistance induced in the membrane. These results indirectly show a linkage between

cathode CL liquid water content and maximum operating temperature, through the mechanism of enhanced back diffusion with liquid availability.

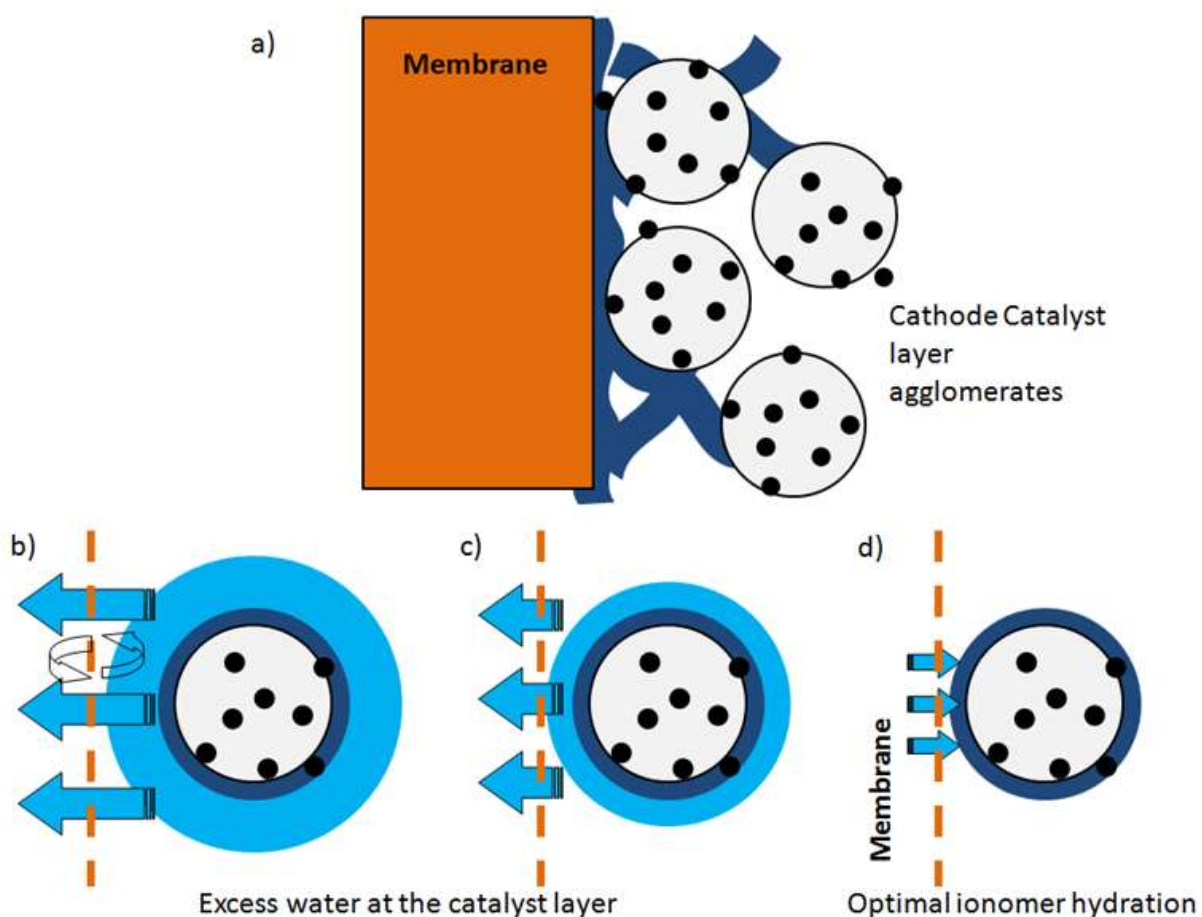


Figure 3-13. Cathode catalyst layer hydration state as interpreted from temperature step experiments a) membrane and cathode catalyst layer schematic, b) agglomerate with excess water and back diffusion, c) agglomerate with partially evaporated water film, d) enough water for ionomer hydration only, and limited back diffusion

Conclusion

A comprehensive examination of net water movement, ASR and EIS data were used to understand the origins of performance and operation limitations and enable high temperature operation suitable for automotive application at high current density (2 A cm^{-2}) of a PEFC using a porous open metallic element (OME) flow field. Operation at ultra-high current density (3 A cm^{-2}) is possible. For the OME architecture, the limiting factor for high power operation at elevated temperatures suitable for automotive operation is anodic dry-out triggered by electro-osmotic drag as a result of improved water evacuation from the cathode. Results indicated a coupling between the availability of liquid in the catalyst layer and maintaining stable high temperature operation. As temperature was increased at any specific operating condition, voltage increased since more catalyst areas were cleared, as long as the net water drag (NWD) was toward the anode. After the maximum voltage peak, a further increase in temperature resulted in a net water movement toward the cathode, gradually drying out the anode side of the membrane. This anodic dry out resulted in an increased ASR and reduction of voltage. When ASR reached a high value due to excess dry-out, steady operation at high temperature was not possible and a transient voltage drop was recorded until cell shutdown. The increase in cathode pressure and cathode inlet relative humidity increased maximum temperature for which stable operation is possible (from 60°C to 90°C) for the conditions tested. At a 0.6 Bar differential pressure across the membrane, an effective hydraulic permeability of $3.64 \times 10^{-20} \text{ m}^2$ was measured. This is due to a more negative net water drag caused by improved back diffusion. The trade-off between liquid water overshadowing cathode catalyst sites and its

contribution in promoting back diffusion is identified as key in the design for anodic dry-out limited operation.

References

1. Toyota Motors Co., Detroit MI. [press release]. *“Toyota Confirms Hydrogen Fuel-Cell Sedan Due Out in 2015”* Aug. 8 2012. Retrieved from:
<http://www.insideline.com/toyota/toyota-confirms-hydrogen-fuel-cell-sedan-due-out-in-2015.html>
2. Toyota Motors Co. Detroit Auto Show 2012 [press release]. *“Toyota: \$50,000 fuel cell sedan on track to launch in 2015, or sooner”*. Retrieved from:
<http://green.autoblog.com/2011/01/14/toyota-fuel-cell-sedan-on-track-for-2015/>
3. Nissan Motor Co. Japan [press release]. *“by 2016 [...] all-new fuel cell electric vehicle (FCEV) together with strategic partner, Daimler”*. Retrieved from:
<http://green.autoblog.com/2011/11/29/nissan-fuel-cell-vehicle-on-track-for-2015/>
4. General Motors. Detroit MI. [press release]. *““We do believe fuel cells can be commercialized by (the) 2015/2016 time frame”*. Retrieved from:
<http://www.earthtechling.com/2012/09/gm-keeps-2015-in-its-sights-for-fuel-cell-vehicles/>
5. T. A. Zawodzinski, T. E. Springer, F. Uribe, S. Gottesfeld. Solid State Ionics, 60 (1993) 199.
6. M. L. Perry, J. Newman, E. J. Cairns. J Electrochem Soc, 145 (1998) 5.
7. T.E. Springer, S. Gottesfeld. Electrochem Soc Proc, 197 (1991) 232.
8. M. Eikerling, A.A. Kornyshev. J Electroanal Chem, 453 (1998) 89.
9. H. Li, Y. Tang, Z. Wang, Z. Shi, S. Wu, D. Song, J. Zhang, K. Fatih, J. Zhang, H. Wang, Z. Liu, R. Abouatallah, A. Mazza. J Power Sources, 178 (2008) 103.
10. X. Li, I. Sabir. Int J Hydrogen Energy 30 (2005) 359.

11. A. Pollegri, P. M. Spaziente, US Patent No. 4, 197,178, 1980.
12. F. Spurrier, B. Pierce, M. Wright, US Patent No. 4,631,239, 1986.
13. S. Granata, B. Woodle, US Patent No. 4,684,582, 1987.
14. D. Jeon, S. Greenway, S. Shimpalee, J. Van Zee. Int J Hydrogen Energy 33 (2008) 1052.
15. G. Hu, J. Fan, S. Chen, Y. Liu, K. Cen. J Power Sources 136 (2004) 1.
16. L. Wang, H. Liu. J Power Sources 134 (2004) 185.
17. C. Cavalca, S. Homeyer, E. Walsworth, US Patent No. 5,686,199, 1997.
18. N. Pekula, K. Heller, P. Chuang, A. Turhan, M.M. Mench, J. Brenizer, K. Unlu. Nucl Instrum Methods Phys Res 542 (2005) 134.
19. T. Trabold, J. Owejan, D. Jacobson, M. Arif, P. Huffman. Int J Heat Mass Transf 49 (2006) 4712.
20. A. Kazim, H. T. Liu, P. Forges. J Appl Electrochem 43 (1999) 1409.
21. A. Turhan, S. Kim, M. C. Hatzell, and M. M. Mench. Electrochi. Acta 55 (2010) 2734.
22. P. Owejan, T.A. Trabold, D.L. Jacobson, M. Arif, S.G. Kandlikar. Int J Hydrogen Energy, 32 (2007) 4489.
23. S. Litster, C. Buie, T. Fabian, J. Eaton, J. Santiago. J Power Sources, 154 (2007) 1049.
24. G. Velayutham, J. Kaushik, N. Rajalakshmi, K. S. Dhathathreyan. WILEY-VCH, FUEL CELLS 07 2007 314.
25. G. Park, Y. Sohn, T. Yang, Y. Yoon, W. Lee, C. Kim. J Power Sources, 131 (2004) 182.

26. M. P. Manahan, and M. M. Mench. J Electrochem Soc, 159 (2012) F322.
27. H. Markötter, R. Alink, J. Haußmann, K. Dittmann, T. Arlt, F. Wieder, C. Tötzke, M. Klages, C. Reiter, H. Riesemeier, J. Scholta, D. Gerteisen, J. Banhart, I. Manke. Int J Hydrogen Energy, 37 (2012) 7757.
28. M. P. Manahan, M.C. Hatzell, E. C. Kumbur, M. M. Mench. J Power Sources, 196 (2011) 5573.
29. M. S. Wilson, C. Zawodzinski, US Patent No. 6,207,310 B1
30. M. S. Wilson, C. Zawodzinski, US Patent No. 6,037,072
31. M. S. Wilson, C. Zawodzinski, US Patent No. 5,798,187
32. M. S. Wilson, US Patent No. 5,641,586
33. S. Arisetty, A. K. Prasad, S. G. Advani. J Power Sources 165 (2007) 49
34. T. Shudo, S. Naganuma. Society Automotive Engineers 39 (2011) 7261
35. A. Kumar, R. G. Reddy. J Power Sources 113 (2003) 54
36. B. T. Tsai, C. J. Tseng, Z. S. Liu, C. H. Wang, C. I. Lee, C. C. Yang, S. K. Lo. Int J Hydrogen Energy 37 (2012) I3060
37. A.K Srouji, L.J. Zheng, R. Dross, A. Turhan, M. M. Mench. J Power Sources, 218 (2012) 341.
38. L.J. Zheng, A.K. Srouji, A. Turhan, M. M. Mench. J Electrochem Soc, 159 (2012) F267.
39. M. Eikerling, Y. I. Kharkats, A. A. Kornyshev, Y. M. Volfkovich. J Electrochem Soc, 145 (1998) 2684.
40. B. S. Pivovar. Polymer 47 (2006) 4194.

41. T.A. Zawodzinski, S. Radzinski, R.J. Sherman, V.T. Smith, T.E. Springer, S. Gottesfeld. *J Electrochem Soc*, 140 (1993) 1041.
42. T.A. Zawodzinski, J. Davey, J. Valerio, S. Gottesfeld, *Electrochim. Acta*, 40 (1995) 297.
43. A.B. LaConti, A.R. Fragala, J.R. Boyack, S. Srinivasan, E.G. Will, *Proceedings of the Symposium on Electrode Materials and Processes for Energy Conversion and Storage*, 77 (1977) 354.
44. T.F. Fuller, J. Newman, *J. Electrochem. Soc.* 139 (1992) 1332.
45. G. Xie, T. Okada, *J. Electrochem. Soc.* 142 (1995) 3057.
46. X. Ren, W. Henderson, S. Gottesfeld, *J. Electrochem. Soc.* 144 (1997) L267.
47. S. Kim, and M. M. Mench. *J Membrane Science*, 328, (2009), 113.
48. M. Tasaka, T. Hirai, R. Kiyono, Y. Aki, *J Membrane Sci* **71**, 151 (1992).
49. J. P. G. Villaluenga, B. Seoane, V. M. Barragan, C. Ruiz-Bauza, *J Membrane Sci* **274**, 116 (2006).
50. R. Zaffou, S. Y. Jung, H. R. Kunz, J. M. Fenton, *Electrochemical and Solid-State Letters* **9**, A418 (2006).
51. R. Bradean, H. Haas, K. Eggen, C. Richards, T. Vrba, *ECS Transaction* **3**(1), 1159 (2006).
52. DOE, Fuel Cell Technologies Program, Multi-Year Research and Development Plan. (2011),

http://www1.eere.energy.gov/hydrogenandfuelcells/mypp/pdfs/fuel_cells.pdf
53. S. Jung, S. Kim, M. Kim, Y. Park, T. Lim. *J Power Sources*. 170 (2007) 324.
54. D. Jeon, K. Kim, S. Baek, J. Nam. *Int J Hydrogen Energy*, 36 (2011) 2499.

55. M. M. Mench. Fuel Cell Engines, Wiley and Sons (2008).
56. D. M. Bernardi, M. W. Verbrugge, J Electrochem Soc, 139 (1992) 2477.
57. F. Meier, G. Eigenberger, Electrochimica Acta, 49 (2004) 1731.
58. D. Malevich, E. Halliop, A.B. Peppley, G.J. Pharoah, K. Karan, J Electrochem Soc, 156 (2009) B216.
59. N. Fouquet, C. Doulet, C. Nouillant, G. Dauphin-Tanguy, B. Ould-Bouamama, J Power Sources, 159 (2006) 905.
60. H. A. Gasteiger, W. Gu, R. Makharia, M. F. Mathias, B. Sompalli. Wiley VCH, New York (2003) 593.

Chapter 4 Oxygen Transport Resistance in Polymer Electrolyte Fuel Cell Catalyst Layer

This text is originally submitted to the Journal of the Electrochemical Society referenced as:

Srouji, A. K., Zheng, L. J., Dross R., Mench, M. M., "Oxygen Transport Resistance in Polymer Electrolyte Fuel Cell Catalyst Layer," Journal of the Electrochemical Society 2013, (submitted).

Preface to Chapter 4

The work in this chapter builds on the results of chapters 2 and 3, in order to use the open metallic element fuel cell as a tool to study oxygen transport resistance in the catalyst layer without the channel/land effects eminent to the conventional flow field architecture. Limiting currents are measured under oxygen transport limited conditions to evaluate the fundamental nature of oxygen transport resistance, recently observed with reduced platinum loading. By using two different architectures and different Pt loadings, the indirect effect of water management on oxygen transport resistance is addressed.

The work presented in this chapter is part of a collaborative project between the Pennsylvania State University and Nuvera Fuel Cells Inc., and funded by the U.S. Department of Energy.

Abstract

In this work, limiting current measurements were used to evaluate oxygen transport resistance in the catalyst layer of a PEFC. The pressure independent oxygen transport resistance in the electrode was evaluated with two different cell architectures, and two different cathode Pt loadings (0.4 and 0.07 mgPt.cm⁻²). The compounded effect of the flow field and Pt loading is used to identify the nature of the observed resistance. By varying gas pressure and using different low oxygen concentrations, the total oxygen transport resistance is divided into intermolecular gas diffusion (pressure dependant) and a pressure independent component, Knudsen diffusion or dissolution film resistance. The pressure independent oxygen transport resistance in the catalyst layer was measured to vary between 13.3 and 34.4 s/m. It is shown that the pressure independent oxygen transport resistance increases with reduced Pt loading, but that effect is exacerbated by using conventional channel/lands. The results indicate that the open metallic element architecture improves the oxygen transport resistance in ultra-low Pt loading electrodes due to enhanced water management.

Introduction

Major automotive manufacturers have expressed intentions to introduce fuel cell cars to the consumer market by 2016, marking the onset of the early adoption phase in the long term plan of fuel cell vehicles deployment, reaching mass commercialization by 2025 [1-4]. Exceeding the Department of Energy (DOE) target in terms of stack power density of 0.9 W/cm² is possible [5-6], but continued improvement in performance and price reduction are necessary. One strategy for achieving price reduction is the decrease of total platinum (Pt) loading from 0.4 – 0.25 mgPt.cm⁻² to ultra-low loading of 0.1 mgPt.cm⁻² without sacrificing power density. High performance low Pt loading electrodes are therefore an area of intense research [7]. Oxygen transport in polymer electrolyte fuel cell (PEFC) components becomes critical with high current density operation, specifically because high current density operation was shown to be limited by mass transport.

The concurrent need to reduce precious metal loading while increasing power density has highlighted the issue of oxygen transport in low Pt loaded electrodes. Recently, a number of automotive companies and membrane electrode assembly (MEA) developers have published results in which a resistance of unknown origin, was shown to directly or indirectly scale with Pt loading. A lack of understanding of the mechanism responsible for such resistance is noted, and several possible theories have been presented [10-18]. This lack of fundamental understanding of the origins of this resistance adds complexity to computational models which are designed to capture performance behavior with ultra-low loading electrodes.

In order to reach a reaction site on the cathode side, oxygen must be transported via diffusion or convection from the flow field through the diffusion medium (DM), adjacent to a micro porous layer (MPL) and the catalyst layer (CL). The CL has been described by an agglomerate model composed of a homogenous mixture of ionomer, micropores, and Pt supported on carbon particles [19-21]. The diffusion regime is strongly dependant on pore size distribution. The diffusion media generally consist of larger pores having a diameter of 10 to 100 μm [8, 9], where oxygen transport is dominated by intermolecular diffusion, which is pressure dependant. In the smaller pores of the CL, Knudsen diffusion becomes important. A third type of transport occurs at the CL, when oxygen diffuses through electrolyte and thin liquid water film. Knudsen diffusion and oxygen diffusion in the thin film is independent of pressure via Henry's law [7, 11, 13].

Work at Nissan's research and development center has analyzed reactant gas transport in low platinum loaded electrodes and the performance loss associated with them [10-12]. A pressure independent transport resistance was estimated by subtracting the molecular diffusion resistance from the total gas transport resistance, and was termed the other transport resistance (R_{other}). R_{other} was shown to increase with a larger ionomer to carbon (I/C) ratio. This was interpreted as a result of the difference in porosity with the variation of I/C ratio affecting the Knudsen diffusion coefficient. However, the Knudsen diffusion coefficient was steady regardless of Pt-loadings, while the R_{other} increased with a decrease in Pt-loadings. With a simple transport model, it was suggested that the increase of R_{other} was a result of the decrease in effective Pt surface area (also known as the roughness factor) in the lower loading catalyst layers. After taking into account the observed R_{other} in

a performance model, experimental performance curves obtained with low loading electrodes were still difficult to fit.

Other research published by Toyota investigated the oxygen dissolution rate from the gas phase to the Nafion[®] surface, by varying the Nafion[®] thickness [15]. They conclude that the oxygen dissolution process to the ionomer phase, rather than the large agglomerate, increases oxygen transport resistance at the catalyst. Another important outcome was that their model was able to predict the experimental results by assuming a reasonable size agglomerate, instead of over predicting the agglomerate diameter as done in some other work [15]. In subsequent work it was found that the ionomer-film resistance is dominant, especially at lower temperatures and lower Pt loadings (even when lower loading electrodes were thinner than their high loading counterpart) [16]. The increase of the oxygen permeation resistance through the ionomer film with lower loading electrodes is thought to be a result of the decrease of the ionomer surface area for effective oxygen permeation.

A comprehensive investigation by General Motors examined oxygen transport resistance in PEFC by separating the total transport resistance into the contribution from individual components parts [13]. This was achieved by varying DM and micro porous layer (MPL) thickness. The transport resistance was also separated into pressure-dependant and pressure-independent components. The study concludes that the MPL contributes to less than 10% of total oxygen transport resistance, and that most of it comes from pressure dependant diffusion. The greater part of the pressure-independent transport resistance,

which accounts for 15% of the total oxygen transport resistance, originated from the electrode. Even though defining the physical nature of the other transport resistance was outside the scope of this study, the results do highlight the significance of catalyst layer transport. Another study by General Motors builds on the same method of separating the transport resistance into multiple components, and specifically examines the impact of Pt loading on the oxygen transport resistance [14]. Five different Pt loading cathodes were used, from 0.4 mgPt cm^{-2} down to $0.03 \text{ mgPt cm}^{-2}$, which corresponded to a geometric roughness factor of $235 \text{ cm}^2\text{Pt.cm}^{-2}$ down to $25 \text{ cm}^2\text{Pt.cm}^{-2}$, respectively. The electrode transport resistance was measured to be inversely proportional to Pt loading, or equivalently, Pt surface area (roughness factor). The Pt loading dependant transport resistance was claimed to be of unknown origin, but behaved similarly to a thin resistive film covering the Pt surface. However, given the ionomer conductivity, the estimated thickness of the resistive film and equivalent agglomerate particles dimensions do not correspond to measurements observed by scan electron microscopy (SEM). The authors also note the importance of literature suggesting that thin ionomer films ($<10 \text{ nm}$) have different properties than those of bulk membranes, and that their proton resistance increases dramatically when their thickness is reduced [22]. Kudo et al., hypothesize that interfacial oxygen resistance can dominate bulk diffusion resistance through the ionomer when the ionomer is thin [15].

A model developed by Debe from 3M based on elementary kinetic gas theory and known molecule/surface interaction mechanisms that take place in the Knudsen regime explains the loss of high current density with reduced cathode loading [18]. The model explains that low electrode surface area densities with low Pt loading reduce the rate of physisorption

events, which are related to the gas phase molecular velocities in the Knudsen regime. Debe also clarifies that 3M's Nano-Structured Thin Film (NSTF) electrodes are better suited to entrap adsorbing oxygen molecules due to their alignment, geometrical aspect ratio, and spacing.

Beuscher from W. L. Gore and Associates investigated mass transport resistance by using multiple DM configurations, varying temperature, and diluting oxygen in heliox [17]. The work concluded that Knudsen and film diffusion through ionomer and water account for more than half of the total oxygen transport resistance. Mass transport mechanisms inside the catalyst layer are therefore considerable. Literature values of pressure independent transport resistance in the electrode are summarized in Table 1.

In this work, oxygen transport resistance was studied by the limiting current method, in two different cell architectures using two different cathode Pt loadings to elucidate the effect of the flow field on oxygen transport resistance in the catalyst layer. The effect of the Pt loading on the oxygen transport resistance is also examined. By using different flow fields (a conventional channel / land cell, and an open metallic element cell, designed by Nuvera Fuel Cells Inc.) and different Pt loadings, the compounded effect of Pt loading and flow field was analyzed, to provide a better understanding of the physical origins of the pressure independent oxygen transport resistance in the catalyst layer, and examine if a flow field has any indirect contribution to such resistance. The open metallic element cell is selected as a tool to reduce the effects eminent to the conventional C/L flow field [23-25]. The procedure for limiting current measurement is based on the work of Baker et al

[13], and the data analysis and deconvolution is based on the method of Mashio et al [10], the details of which as applied in this work are summarized in the following sections.

Table 4-1. Summary of methodology and R_{other} measurements from literature.

Publication	Limiting current method used	Temp. (°C)	RH (%)	R_{other} (s/m)	Comments
Mashio et al. [10]	O ₂ dilution in N ₂ O ₂ dilution in He	80	90	7 - 38	Varies I/C ratio
Sakai et al. [11] and Ono et al. [12]	O ₂ dilution in N ₂	80	90	10 - 48	
Nonoyama et al. [16]	O ₂ dilution in N ₂ O ₂ dilution in He	50 - 80	60	38 - 78	Uses a porous metal flow field, to reduce land/channel effects.
Greszler et al. [14]	O ₂ dilution in N ₂	80	62	10 - 170	

Relationship of oxygen transport resistance to limiting current

The total oxygen transport resistance R_T in the cell is defined as the change in oxygen concentration from the channels to the reaction site in the cathode catalyst layer ΔC_{O_2} , divided by the average normal molar flux of oxygen at the catalyst layer N_{O_2} [9, 12]. Since the molar flux of oxygen is related to the current density i by the Faraday constant, R_T may be expressed as

$$R_T = \frac{\Delta C}{N_{O_2}} = \frac{4F}{i} \Delta C \quad (1)$$

Oxygen concentration at the electrode approaches zero when the cell operates at a cathode mass limiting current. Consequently, the concentration difference can be expressed as the channel concentration only, C_{inlet} , which is directly related to the oxygen mole fraction by

$$\Delta C = C_{inlet} = \frac{p-p_w}{RT} \chi_{O_2}^{inlet} \quad (2)$$

With T being the absolute cell temperature, p the total gas pressure, p_w the water vapor partial pressure, and R the universal gas constant. Using Eq. 1 and 2, and operating at limiting current i_{lim} , the total oxygen transport resistance is written as

$$R_T = \frac{4F}{i_{lim}} \frac{p-p_w}{RT} \chi_{O_2}^{inlet} \quad (3)$$

Where i_{lim} is measured from the test stand as described in the following section.

Experimental Method

Cell hardware- Two single cells are used in this study to evaluate the flow field architecture impact on oxygen transport resistance. The first cell has a conventional parallel channel / land (C/L) flow field, as shown in Fig. 1(a). The second cell has an open metallic element (OME) flow field, as shown in Fig. 1(b) and described in previous work [5,6,21,22]. The cell temperature was controlled with coolant flow at very high flow rates to insure temperature stability and uniformity.

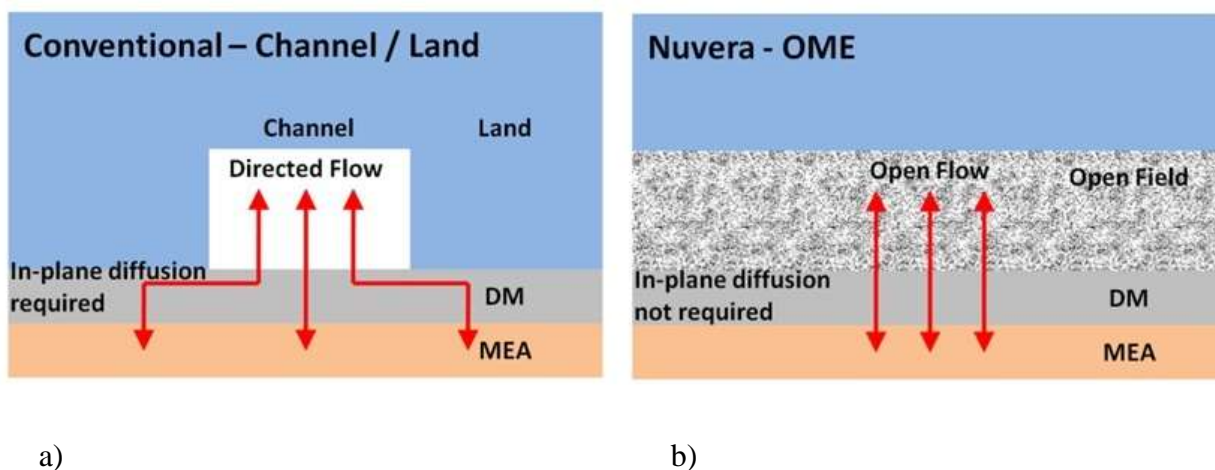


Figure 4-1. Cross section view of cathode in a) Channel / Land, b) Open metallic element fuel cell (not to scale). Reproduced from [5].

Materials – Each cell was tested with two different cathode catalyst loadings. A typical loading of 0.4 mgPt.cm^{-2} , and a high performance ultra-low loading of $0.07 \text{ mgPt.cm}^{-2}$. It is important to note that the electrochemical surface area of both types of electrodes are very similar, even though the Pt loadings were different. The gas diffusion layer used for each cell is a Sigracet SGL 25 BC. The assembled cells' other specifications are summarized in Table 2.

Table 4-2. Cell build specifications

Cell architecture	Cathode catalyst loading (mgPt.cm⁻²)	Diffusion Media
Parallel channel/land	0.4	SGL 25BC
Parallel channel/land	0.07	SGL 25BC
Open Metallic Element	0.4	SGL 25BC
Open Metallic Element	0.07	SGL 25BC

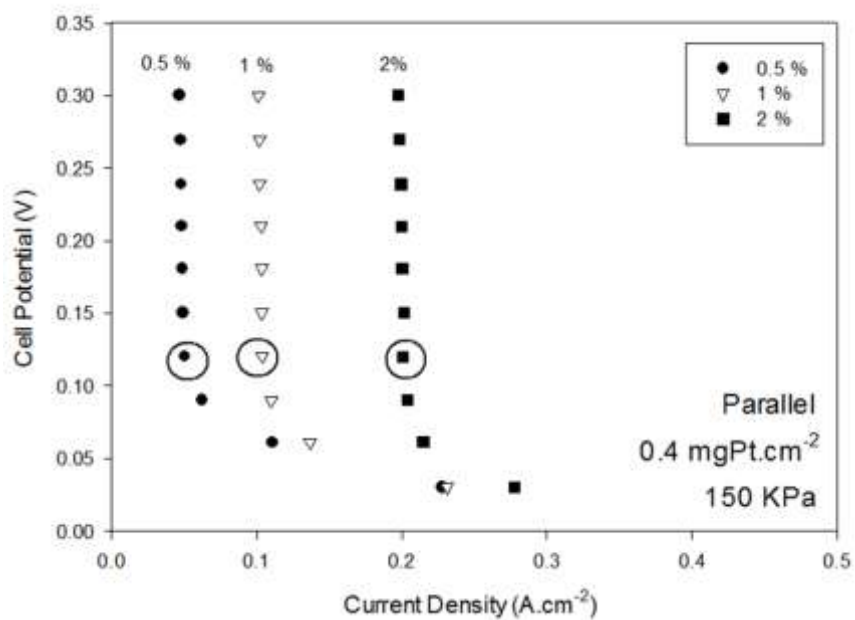
Operating protocol and conditions for limiting current measurement- The method used is mostly similar to the protocol of Baker et al [19]. Limiting current is recorded by reducing the cell potential from 0.3 to 0.03 V in 0.03 V steps, with a three minute hold time at each step. The measurements were conducted at a cell temperature of 80°C and gas streams at 62% relative humidity (RH). Limiting current measurement for each cell and each electrode loading were conducted at three different nitrox mixtures with 0.5, 1 and 2% oxygen dry mole fraction. Each test was repeated at four different cathode stream pressures of 107, 150, 200 and 300 kPa. 62% RH was chosen to keep liquid water condensation minimal in the DM, but provide enough hydration in order not to be limited by membrane resistance. The operating conditions for limiting current measurements are summarized in Table 3.

Table 4-3. Operating parameters for limiting current measurement

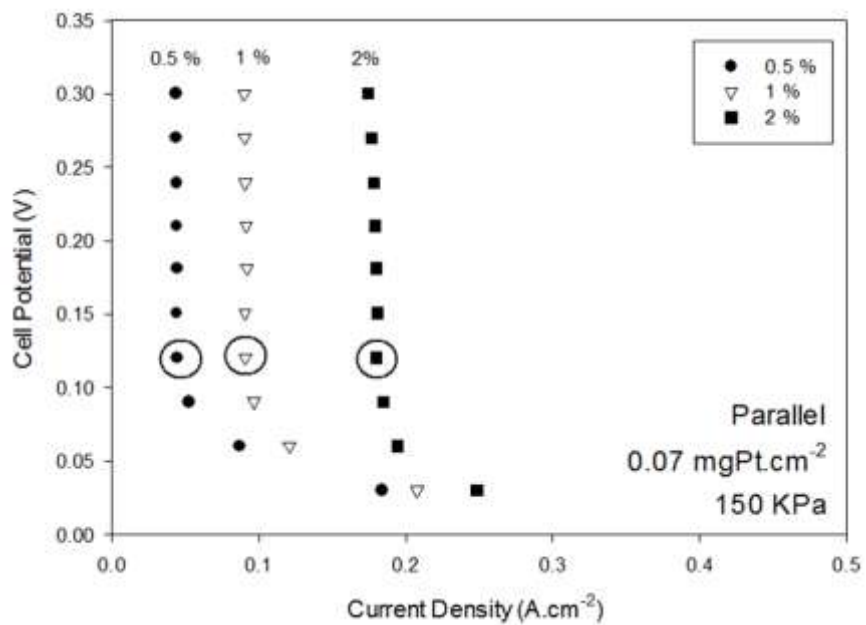
Cell temperature (°C)	Relative humidity (%)	O ₂ dry mole fraction in N ₂	Operating pressure (kPa)			
80	62	0.005	107	150	200	300
		0.010	107	150	200	300
		0.020	107	150	200	300

Results

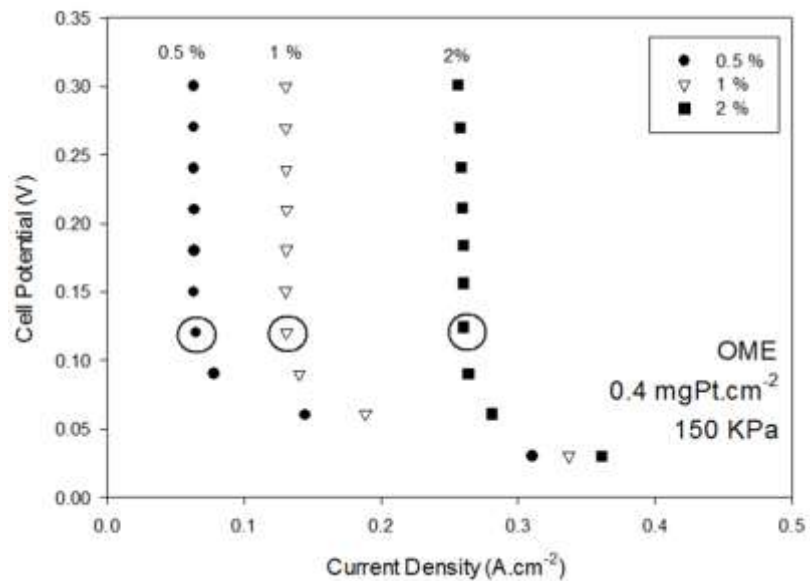
Limiting current measurements and total oxygen transport resistance - Limiting current measurement by step-wise reduction of voltage from 0.3 to 0.03 V are shown in Figure 2, for four different cell specifications at 150 kPa operating pressure, under the three different dry oxygen mole fractions. The same data was also recorded for the other operating pressures of 107, 200, and 300 kPa. As observed in Figure 2, the curves are mostly vertical over 100 mV with no variation of current density as voltage is reduced. This is a clear indication that the cells are operating at an oxygen transport limiting current density. At voltages below 100 mV, hydrogen evolution occurs and current density deviation from the vertical line is visible. Limiting current densities are marked by a circle on Figure 2, and correspond to the current density at a voltage of 120 mV.



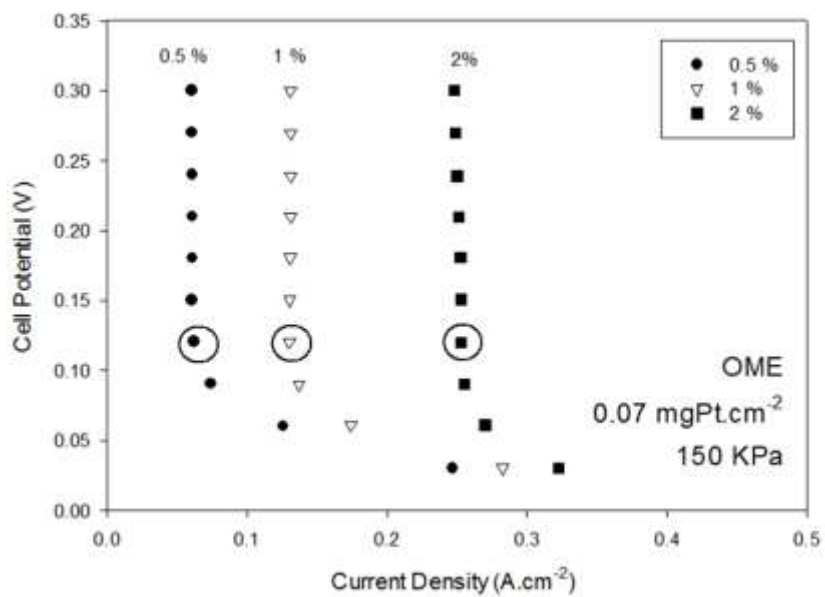
a)



b)



c)



d)

Figure 4-2. Limiting current measurements at a cell operating pressure of 150 kPa, for different flow field architectures and different loadings. a) Parallel with 0.4 mgPt.cm^{-2} , b) Parallel with $0.07 \text{ mgPt.cm}^{-2}$, c) OME with 0.4 mgPt.cm^{-2} , d) OME with $0.07 \text{ mgPt.cm}^{-2}$.

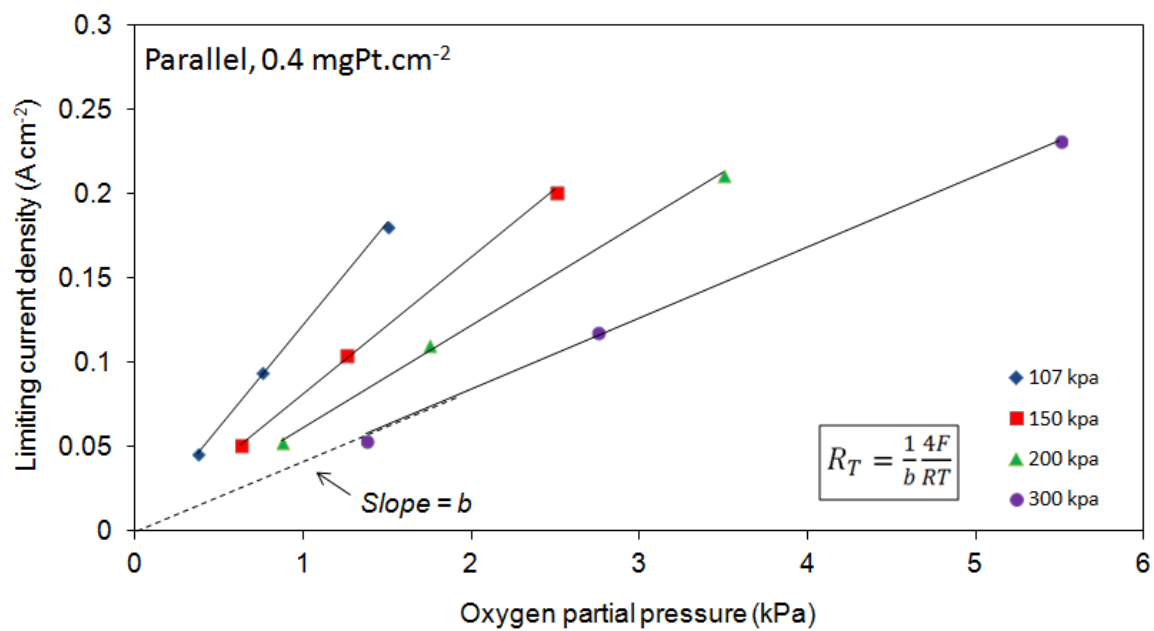
Eq. 3, which relates the total oxygen transport resistance to the limiting current density, can be rewritten as

$$i_{lim} = \frac{1}{R_T} \frac{4F}{RT} (p - p_w) x_{O_2}^{inlet} = \frac{1}{R_T} \frac{4F}{RT} p_{O_2} \quad (4)$$

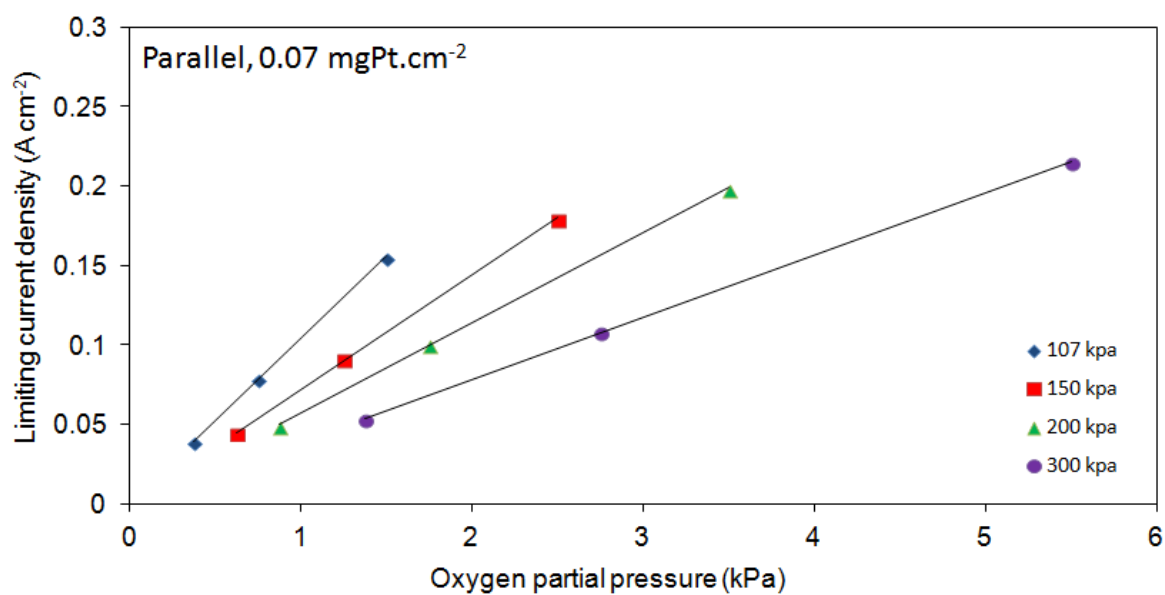
Which is a straight line passing by the origin with slope b

$$b = \frac{1}{R_T} \frac{4F}{RT} \quad (5)$$

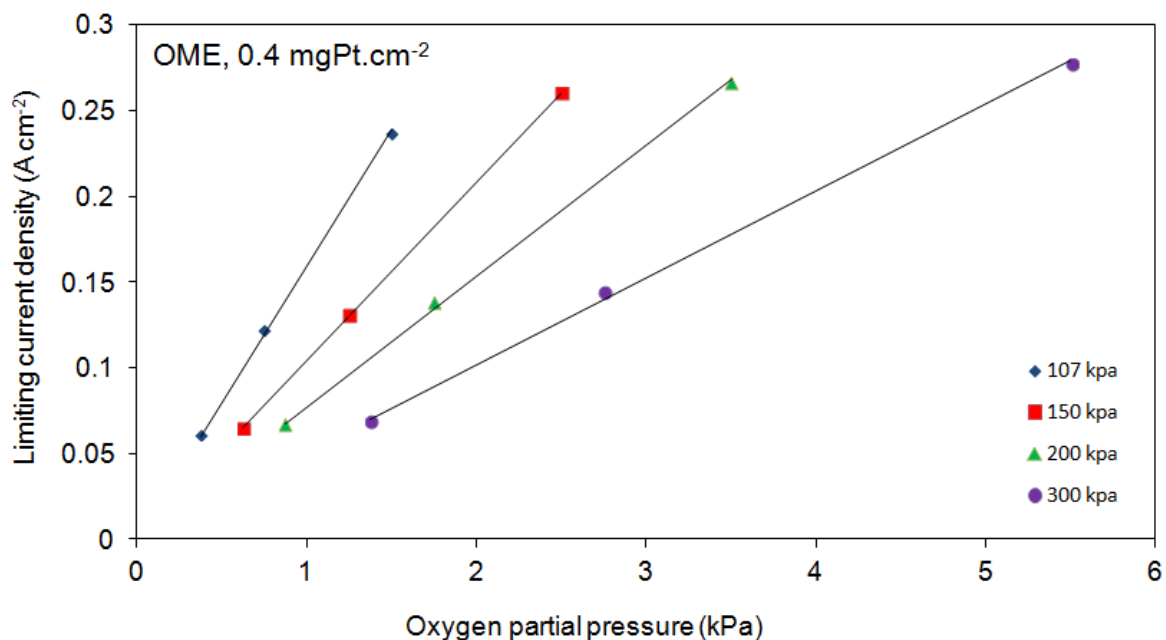
The limiting current density can therefore be plotted as a function of oxygen partial pressure, at each cell operating pressure, as shown in Fig. 3. At each operating pressure, the data indeed lies on a straight line passing through the origin conforming to Eq. 4; an indication that water is not condensing and changing transport properties [9, 12].



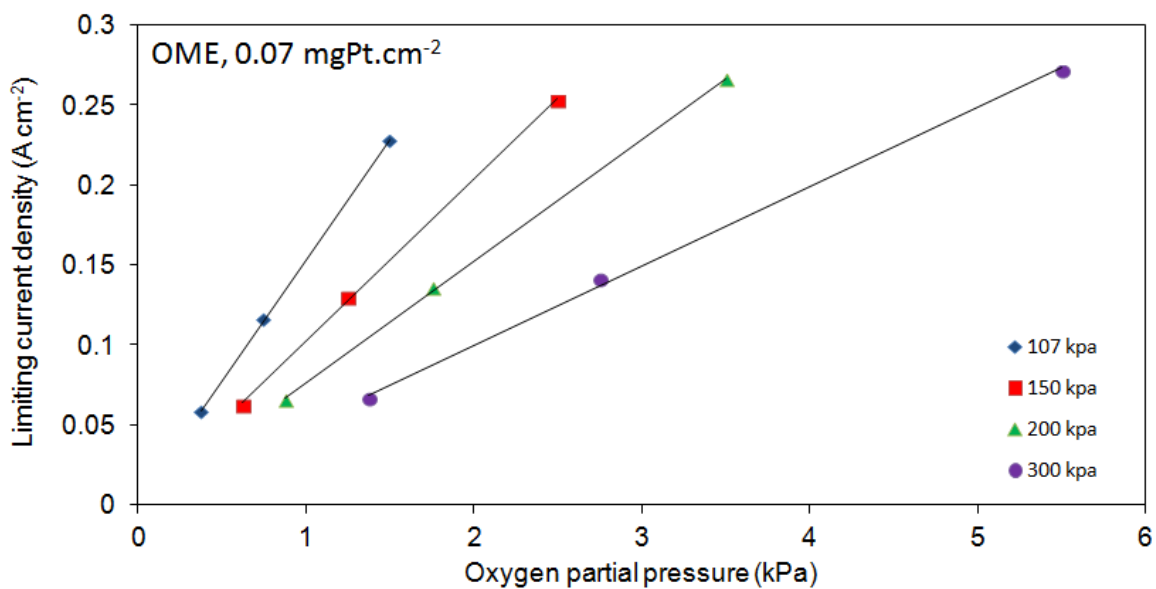
a)



b)



c)



d)

Figure 4-3. Limiting current density as a function of reactant gas partial pressure for different cells. a) Parallel with 0.4 mgPt.cm⁻², b) Parallel with 0.07 mgPt.cm⁻², c) OME with 0.4 mgPt.cm⁻², d) OME with 0.07 mgPt.cm⁻².

From each plot in Fig. 3, and using Eq.5, four values for total oxygen transport resistance R_T are computed from the slopes corresponding to four different cell operating pressures respectively. For each cell assembly, transport resistance R_T is plotted in Fig. 4 as a function of cell operating pressure, and is linearly proportional to the total operating pressure. The slope, is the derivative of the transport resistance with respect to operating pressure, and corresponds to the molecular diffusivity of oxygen, mostly in the DM [9, 12, 23]. Using the analysis developed by Mashio et al [9], the other transport resistance R_{other} , including Knudsen diffusion and transport resistance into the ionomer and thin water films, can be calculated from the slope and the intercept. The methodology for data analysis is summarized in the following section.

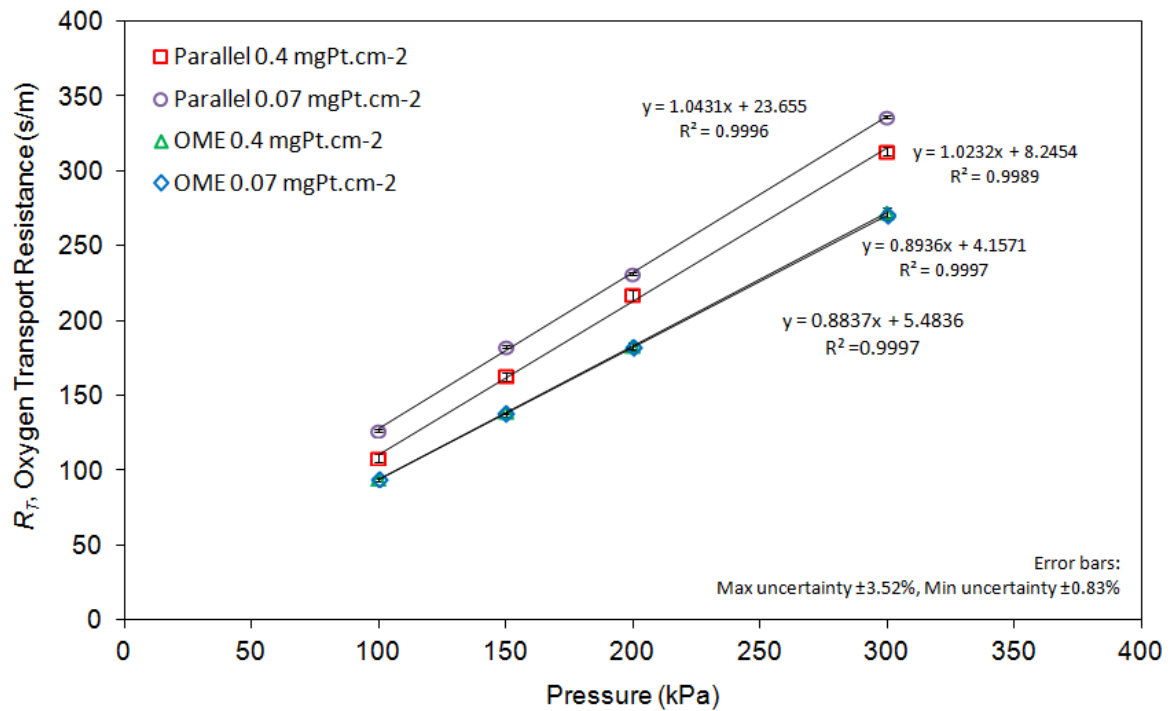


Figure 4-4. Oxygen transport resistance as a function of total pressure for different cell architectures and loadings.

Extraction method of R_{other} from the total oxygen transport resistance R_T – The extraction relies on the Stefan-Maxwell equation for molecular gas diffusion [10, 24], and assumes convection effects to be negligible in the DM and CL at the low-oxygen concentration employed [6, 25, 27]. The relationship between oxygen flux and oxygen concentration gradient is written as

$$\frac{dx_{O_2}}{dz} = \frac{RT}{P} \left(\frac{x_{O_2}N_w - x_wN_{O_2}}{D_{O_2,w}^{eff}} + \frac{x_{O_2}N_{N_2} - x_{N_2}N_{O_2}}{D_{O_2,N_2}^{eff}} \right)$$

(6)

In the molecular diffusion region a linear oxygen profile is assumed, and the molar flux of oxygen is expressed as

$$\begin{aligned} N_{O_2} &= \left(\frac{x_w}{D_{O_2,w}^{eff}} + \frac{x_{N_2}}{D_{O_2,N_2}^{eff}} \right)^{-1} \frac{C_{O_2,2} - C_{O_2,1}}{Z_{dif}} + \left(\frac{x_w}{D_{O_2,w}^{eff}} + \frac{x_{N_2}}{D_{O_2,N_2}^{eff}} \right)^{-1} \left(\frac{x_{O_2}N_w}{D_{O_2,w}^{eff}} + \frac{x_{O_2}N_{N_2}}{D_{O_2,N_2}^{eff}} \right) \\ &= D_{nitrox}^{eff} \frac{C_{O_2,2} - C_{O_2,1}}{Z_{dif}} + D_{nitrox}^{eff} \left(\frac{x_{O_2}N_w}{D_{O_2,w}^{eff}} + \frac{x_{O_2}N_{N_2}}{D_{O_2,N_2}^{eff}} \right) \\ &= R_{dif}^{-1} (C_{O_2,2} - C_{O_2,1}) + \left[D_{nitrox}^{eff} \left(\frac{x_{O_2}N_w}{D_{O_2,w}^{eff}} + \frac{x_{O_2}N_{N_2}}{D_{O_2,N_2}^{eff}} \right) \right] \end{aligned} \quad (7)$$

where the indices 2 and 1 correspond to the gas channel and the transition boundary between molecular diffusion region and Knudsen diffusion region, respectively. Index 0 is used next for the surface of the Pt. R_{dif} is the molecular diffusion resistance, defined as the inverse of diffusivity. Z_{dif} is the average oxygen diffusion distance, and is different from

cell to cell architecture due to variation in channel / land dimensions. Z_{dif} is expected to be smaller for the OME cell due to elimination of conventional lands under which oxygen would normally diffuse, as was shown in Fig.1. The calculations in the following portion are in agreement with this. Since very low oxygen concentration is used, the term in brackets in Eq. 7 can be ignored.

In the other transport processes responsible for R_{other} , oxygen paths include Knudsen diffusion and dissolution through ionomer and liquid film phases. According to Fick's law:

$$N_{O_2} = \frac{(C_{O_2,1} - C_{O_2,0})}{R_{other}} \quad (8)$$

Using Eq. 7 and 8, with oxygen concentration at the catalyst $C_{O_2,0}$ equal zero during limiting current operation, and assuming a series alignment of transport resistances

$$N_{O_2} = \frac{C_{O_2,2}}{R_{dif} + R_{other}} = \frac{C_{O_2,2}}{R_T} \quad (9)$$

Where R_T is total oxygen diffusion resistance as expressed in Eq. 3.

The molecular diffusion resistance is expressed as a function of the total operating pressure as

$$\begin{aligned}
R_{dif} &= \frac{Z_{dif}}{D_{nitrox}^{eff}} = Z_{dif} \left(\frac{x_w}{D_{O_2,w}^{eff}} + \frac{x_{N_2}}{D_{O_2,N_2}^{eff}} \right) = Z_{dif} \left(\frac{x_w}{D_{O_2,w}^{eff}} + \frac{1-x_{O_2}-x_w}{D_{O_2,N_2}^{eff}} \right) \\
&= Z_{dif} \left(\frac{P_w}{PD_{O_2,w}^{eff}} + \frac{P-P_{O_2}-P_w}{PD_{O_2,N_2}^{eff}} \right) \\
&= \frac{Z_{dif}}{PD_{O_2,N_2}^{eff}} P + \left(\frac{1}{PD_{O_2,w}^{eff}} - \frac{1}{PD_{O_2,N_2}^{eff}} \right) Z_{dif} P_w - \frac{Z_{dif} P_{O_2}}{PD_{O_2,N_2}^{eff}}
\end{aligned} \tag{10}$$

Eq. 10 is expressed as

$$R_{dif} = R_{dif,P}P + R_{dif,0} \tag{11}$$

Therefore the total transport resistance can be expressed in terms of pressure dependant and pressure independent terms as

$$R_T = R_{dif,P}P + R_{dif,0} + R_{other} \tag{12}$$

Mashio et al [9] highlight that R_{other} should be described as function of pressure since the Knudsen number (ratio of pore diameter and mean free path of gas) is a function of pressure, more specifically inversely proportional to pressure. It is arguable that if Knudsen diffusion resistance depends on pressure more than the molecular diffusion resistance depends on pressure, then the total transport resistance R_T would be inversely proportional to pressure. However, as indicated from the data, R_T was proportional to pressure, which leads to the assumption of R_{other} being independent of pressure in the analysis.

Using Eq. 12 and the four linear curves from Fig. 4, $R_{dif,P}$ of each cell assembly is determined from each corresponding slope. Employing the effective molecular diffusion distance Z_{dif}^{eff} , $R_{dif,P}$ and $R_{dif,0}$ are expressed from Eq. 10 and 11 as

$$R_{dif,P} = \frac{Z_{dif}}{PD_{O_2,N_2}^{eff}} = \frac{Z_{dif}^{eff}}{PD_{O_2,N_2}} \quad (13)$$

$$R_{dif,0} = \left(\frac{1}{PD_{O_2,w}^{eff}} - \frac{1}{PD_{O_2,N_2}^{eff}} \right) Z_{dif}^{eff} P_w - \frac{Z_{dif}^{eff} P_{O_2}}{PD_{O_2,N_2}} \quad (14)$$

Z_{dif}^{eff} is calculate from Eq.13 after $R_{dif,P}$ is computed form the slopes of Fig. 4. With a computed value of Z_{dif}^{eff} , $R_{dif,0}$ can then be calculated from Eq. 14. Using the intercepts of the curves in Fig.4 and the corresponding values of $R_{dif,0}$, R_{other} can be calculated for each one of the four cell assemblies. The results for each cell assembly are summarized in Table 4.

Table 4-4. Summary of computed transport resistances and effective diffusion lengths

	Parallel		OME	
	0.07 mgPt.cm ⁻²	0.4 mgPt.cm ⁻²	0.07 mgPt.cm ⁻²	0.4 mgPt.cm ⁻²
R_{dif,p} (slope) s/(m.kpa)	1.043	1.023	0.884	0.894
Intercept (s/m)	23.655	8.245	5.484	4.157
Z_{eff_diff} (m)	0.00252	0.00247	0.00214	0.00216
R_{other} (s/m)	34.316	18.703	14.512	13.290

Discussion and interpretation

By comparing different cell architectures and different Pt loadings, the effect of eliminating the conventional channel/land paradigm on oxygen transport resistance can be evaluated, in addition to the combined effect of flow field architecture and reduced Pt. As shown in Table 4 and Fig 5., the pressure dependant oxygen transport resistance $R_{diff,p}$, was strictly a function of the specific flow field architecture. $R_{diff,p}$ was 15% lower for the cells using the open metallic element, compared to parallel channel/land. This is due to the reduced effective molecular diffusion distance Z_{dif}^{eff} by 15% as reported in Table 4, which is a direct result of the reduction or quasi-elimination of through plane diffusion under lands as shown in Fig1. $R_{diff,p}$ was almost identical for each specific flow field regardless of the Pt loading. This is expected since intermolecular gas diffusion dominates in larger pores such as the DM, and would be insensitive to Pt loading. Reduced Z_{dif}^{eff} and $R_{diff,p}$ for the OME architecture and the fact that the measurements yielded “identical” values specific to flow field selection is a good indication of the soundness of the original measured data and methodology.

Values for R_{other} were higher for the cells using the parallel channel/land flow field compared to their OME counterparts with same Pt loading, as shown in Fig. 6. R_{other} for the OME cell slightly increased with the reduction of Pt loading, while the parallel channel/land cell suffered from a significant increase in R_{other} at the reduced Pt loading of $0.07 \text{ mgPt.cm}^{-2}$. The values computed for R_{other} in Table 4 are in good agreement with the ranges computed by other research groups and summarized in Table 1. The fact that the

other transport resistance increased in a greater proportion with the channel/land architecture when Pt loading decreased, combined with the nature of R_{other} being pressure independent gives evidence supporting film resistance at the catalyst layer, possibly due to presence of thin liquid water film around catalyst agglomerates. The increase in R_{other} could be due to increased oxygen dissolution resistance, as proposed by Kudo et al [14]. The open metallic element transport, performance and water management was investigated in previous work [5, 26] and was shown to be characterized by enhanced removal of water vapor and liquid phase from the cathode of the cell. It was also shown that when enough water was present at the catalyst layer for back diffusion into the membrane, the charge transfer and mass transport resistance increased due to possible catalyst coverage with liquid film. This is in agreement with the findings of Mashio et al [10], and Nanoyama et al [16] who propose an oxygen dissolution resistance due to ionomer thin film with reduced loading, and liquid water film formation on catalyst agglomerate. It is possible that with the cells used in this study, R_{other} for the Pt loading of 0.4 mgPt.cm^{-2} increased in the parallel cell due thin liquid water film retention inherent to the parallel C/L alterations, and the more dramatic increase of R_{other} with ultra-low loading of $0.07 \text{ mgPt.cm}^{-2}$ using C/L is a compounded effect due to liquid thin film over reduced size Pt agglomerates. Under the operating conditions it is clear that the flow field architecture can have an important effect in analyzing oxygen transport in the catalyst layer, due to change in water removal efficiency.

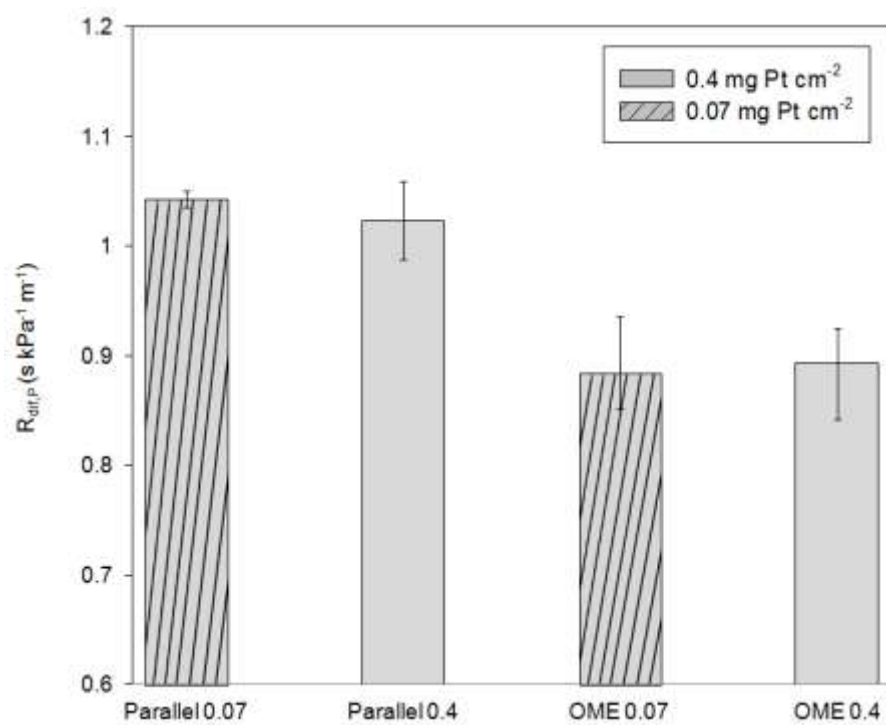


Figure 4-5. Effect of Pt loading and flow field architecture on pressure dependant molecular diffusion resistance $R_{diff,p}$.

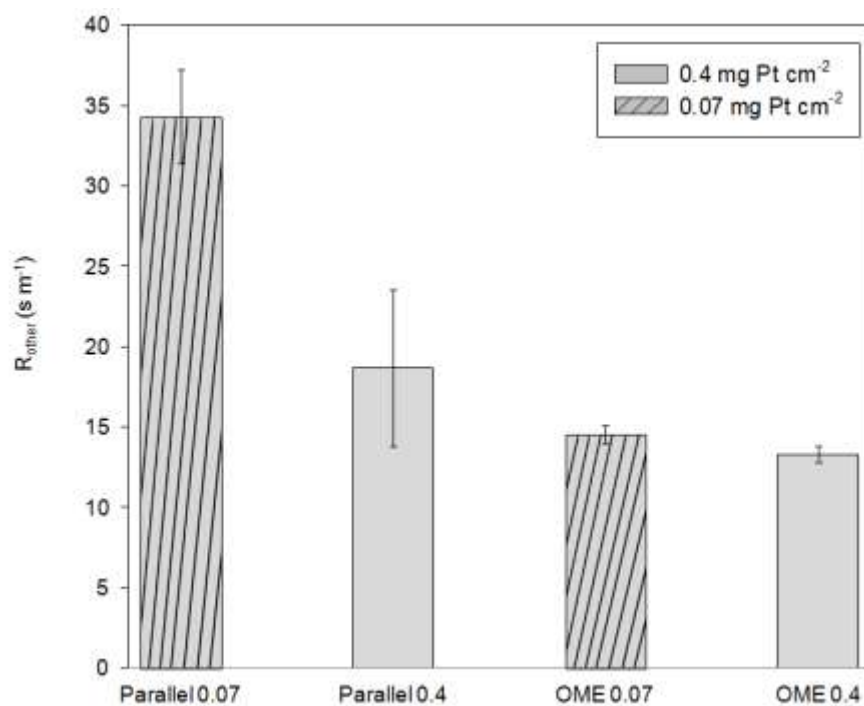


Figure 4-6. Effect of Pt loading and flow field architecture on the other transport resistance R_{other} .

Conclusion

Reduction of Pt loading at the cathode catalyst layer of a PEFC without a concomitant loss of performance is important to achieve cost target reductions. Limiting current measurements were used to determine the effect of reduced Pt loading (from 0.4 mgPt.cm^{-2} to ultralow $0.07 \text{ mgPt.cm}^{-2}$), as well as the impact of flow field architecture on the pressure independent oxygen transport resistance (R_{other}), at the catalyst layer.

The increase in R_{other} with reduced catalyst Pt loading was significant using the parallel channel/land flow field. R_{other} increased from 13.7 to 34.3 s/m with reduction of loading and using a conventional flow field, while it only varied from 13.3 to 14.5 s/m with the open metallic element. This suggests that the origin of the increased R_{other} can lie in a phenomena affected by the flow field specifications.

Pressure dependant oxygen transport resistance was insensitive to Pt loading for both cells and was a function of flow field architecture only. It was 15% lower for the open metallic element, due to 15% reduction in effective oxygen diffusion length, Z_{dif}^{eff} , as a result of eliminating lands.

The results show that under operating conditions used, it is clear that the flow field architecture can have an important effect in analyzing oxygen transport in the catalyst layer. An increased R_{other} is possible due to reduction in agglomerate size and effective ionomer surface area for oxygen dilution. Oxygen dilution resistance is increased with the conventional channel/land architecture due to its ineffectiveness in flushing thin liquid water film in the catalyst layer. This effect was mitigated in an open metallic flow field known to improve water removal from the cathode.

References

1. Toyota Motors Co., Detroit MI. [press release]. *“Toyota Confirms Hydrogen Fuel-Cell Sedan Due Out in 2015”* Aug. 8 2012. Retrieved from: <http://www.insideline.com/toyota/toyota-confirms-hydrogen-fuel-cell-sedan-due-out-in-2015.html>
2. Toyota Motors Co. Detroit Auto Show 2012 [press release]. *“Toyota: \$50,000 fuel cell sedan on track to launch in 2015, or sooner”*. Retrieved from: <http://green.autoblog.com/2011/01/14/toyota-fuel-cell-sedan-on-track-for-2015/>
3. Nissan Motor Co. Japan [press release]. *“by 2016 [...] all-new fuel cell electric vehicle (FCEV) together with strategic partner, Daimler”*. Retrieved from: <http://green.autoblog.com/2011/11/29/nissan-fuel-cell-vehicle-on-track-for-2015/>
4. General Motors. Detroit MI. [press release]. *““We do believe fuel cells can be commercialized by (the) 2015/2016 time frame”*. Retrieved from: <http://www.earthtechling.com/2012/09/gm-keeps-2015-in-its-sights-for-fuel-cell-vehicles/>
5. A.K. Srouji, L.J. Zheng, R. Dross, A. Turhan, M. M. Mench. J Power Sources, 218 (2012) 341.
6. L.J. Zheng, A.K. Srouji, A. Turhan, M. M. Mench. J Electrochem Soc, 159 (2012) F267.
7. S. Martin, P. L. Garcia-Ybarra, J.L. Castillo. Int J Hydrogen Energy 35 (2010) I0446.
8. M. V. Williams, E. Begg, L. Bonville, H. R. Kunz, J. M. Fenton. J Electrochem Soc, 151 (2004) A1173.

9. C. S. Kong, D. Y. Kim, H. Lee, Y. Shul, T. Lee. J Power Sources, 108 (2002) 185.
10. T. Mashio, A. Ohma, S. Yamamoto, K. Shinohara. ECS Transactions, 11 (2007) 529.
11. K. Sakai, K. Sato, T. Mashio, A. Ohma, K. Yamaguchi, K. Shinohara. ECS Transactions 25 (2009) 1193
12. Y. Ono, T. Mashio, S. Takaichi, A. Ohma, H. Kanesaka, K. Shinohara. ECS Transactions, 28 (2010) 69.
13. D. R. Baker, D. A. Caulk, K. C. Neyerlin, M. W. Murphy. J Electrochem Soc, 156 (2009) B991.
14. T. Greszler, D. Caulk, P. Sinha. J Electrochem Soc, 159 (2012) F831.
15. K. Kudo, T. Suzuki, Y. Morimoto. ECS Transactions, 33 (2010) 1495.
16. N. Nonoyama, S. Okazaki, A. Z. Weber, Y. Ikogi, T. Yoshida. J Electrochem Soc, 158 (2011) B416.
17. U. Beuscher. J Electrochem Soc, 153 (2006) A1788.
18. M. K. Debe. J Electrochem Soc, 159 (2011) B53.
19. A. Z. Weber, J. Newman. Chem. Rev. 104 (2004) 4679.
20. W. Yoon, A. Z. Weber. J Electrochem Soc. 158 (2011) B1007.
21. W. K. Epting, S. Litster. Int J Hydrogen Energy. 37 (2012) 8505.
22. Z. Siroma, R. Kakitsubo, N. Fujiwara, T. Ioroi, S.-i. Yamazaki, K. Yasuda. J Power Sources, 189 (2009) 994.
23. A. Turhan, K. Heller, J.S. Brenizer, M. M. Mench. J Power Sources, 180 (2008) 773.

24. A. Turhan, S. Kim, M. Hatzell, M. M. Mench. *Electrochim Acta*, 55 (2010) 2734.
25. K. T. Cho, M. M. Mench. *J Power Sources*, 195 (2010) 6748.
26. D. Baker, C. Wieser, K.C. Neyerling, N.W. Murphy, *ECS Trans.*, 3 (2006) 989.
27. Cussler E. *Diffusion: mass transfer in fluid systems* 2nd ed. Cambridge University Press, 1997.
28. L.J. Zheng, A.K. Srouji, R. Dross, A. Turhan, M. M. Mench. *J Electrochem Soc*, 160 (2013) F119.
29. A.K. Srouji, L.J. Zheng, R. Dross, A. Turhan, M. M. Mench. *J Power Sources*, in press, (2013)
30. J. Benziger, E. Kimball, R. Mejia-Ariza, I. Kevrekidis. *J American Inst Chem Eng*. 57 (2011) 9.

Chapter 5 CONCLUSION

A fuel cell with an open metallic element flow field is characterized with the ultimate goal of investigating the pressure independent oxygen transport resistance appearing in catalyst layers with low precious metal loading.

Stable operation at 3 A cm^{-2} is recorded with an OME cell, and reported for the first time in the open literature. A 33% increase in power density over a conventional channel/land flow field is noted. Oxygen dilution in helium (heliox) improved parallel cell performance due to enhanced intermolecular gas diffusion of oxygen, but no reportable gains in power density were recorded when air was replaced with heliox in an OME cell. In fact the parallel cell operating on heliox performed like the OME operating on air. Performance curves with corresponding electrochemical impedance spectroscopy data indicated that the OME flow field improved gas diffusion of oxygen as a result of eliminating conventional lands. Diffusion length is reduced as a result of diminished in the plane diffusion. OME also reduced ohmic resistance of the cell due to more uniform compression. Ultra-high current density operation was not precluded by film resistance.

Water management at high current density using the OME flow field was investigated by varying cell temperature, gas relative humidity, and backpressure differential. Steady-state and transient net water drag measurements coupled with electrochemical impedance spectroscopy indicated that operation was limited by anodic dry-out of the membrane.

Unlike conventional channel/land flow fields known for trapping water in the cathode, the OME was shown to improve liquid water evacuation from the cathode compartment of the cell. Excess water removal leads to reduced back diffusion of water, and when coupled with high current density, results in electroosmotic drag being the dominant mechanism.

The characteristics of the OME cell performance, improved gas diffusion, and enhanced water management, make it a good tool to investigate oxygen transport resistance in the catalyst layer, without the overshadow effects of channel/lands. Limiting current measurements were used to determine the effect of reduced Pt loading (from 0.4 mgPt.cm^{-2} to ultralow $0.07 \text{ mgPt.cm}^{-2}$), as well as the impact of flow field architecture on the pressure independent oxygen transport resistance (R_{other}), at the catalyst layer. The increase in R_{other} with reduced catalyst Pt loading was more significant using the parallel channel/land flow field. This suggests that the origin of the increased R_{other} can lie in a phenomena affected by the flow field specifications. The origin of transport resistance is identified as film resistance. As water is trapped in the electrode due to the inherent nature of a channel/land flow field, water film covers catalyst agglomerates. Smaller agglomerates, associated with reduced loading, require a higher flux of oxygen due to their decreased surface area. Their coverage with water makes them less robust to oxygen transport, than bigger surface area agglomerates. The OME through improved water evacuation reduces water content in the catalyst layer and leads to reduced water film presence on agglomerates. Hence the lower oxygen transport resistance at the catalyst layer, measured using the OME fuel cell.

Chapter 6 FUTURE WORK

In this work the characteristic performance and mass transport of a fuel cell using an open metallic element flow field were presented. Anodic dry-out triggered by water evacuation from the cathode side is highlighted as the main operating limitation of such fuel cell. Even though the water evacuation properties can limit operation, that same phenomena makes the OME cell suitable to be used as a tool to investigate the origins of increased oxygen transport resistance with low platinum loading electrodes. The nature of the apparent oxygen transport resistance in low loading electrodes is identified as oxygen dissolution in thin film. This work can be used as a foundation for further investigations as described below.

Fundamental two-phase transport through porous metallic element

Two phase water transport in conventional channels in the flow direction has been a subject of intense research. Water droplet accumulation and formation on channel walls has been examined, and the effects of channel wall properties have been studied intensively, through direct camera/microscope visualization, neutron radiography, and x-ray synchrotron imaging. Two-phase transport and liquid droplet transport in an open metallic element flow field has not been investigated or visualized. The elimination of conventional lands was clearly shown to improve water phase removal, but the specific role of pore network in porous metallic media remains unexplored. Visualization

techniques if employed will show if water droplets block pores, or accumulate around necks and struts of pores and leave the center of the pore clear for gas phase transport. Also it is not clear if water droplets are flushed by moving from pore to pore, or along the struts of different pores. Effects of material properties and geometric properties such as pore shape can be studied to tailor highly efficient open metallic element flow fields.

Fundamental water transport mechanism through cell layers

As water is formed at the cathode catalyst layer, it finds its way out through diffusion and capillary action through the microporous layer, the diffusion media, and is flushed from the channels, or open metallic element. When using a conventional channel/land design, multiple two phase flow regimes through the diffusion media have been identified such as funicular regime, capillary fingering, and eruptive regime. The open metallic element, when adjacent to the diffusion media could be thought of as additional branches of the diffusion media pore network. Multiple pores of the diffusion media meet in one larger pore of the open metallic element. The effect of the bifurcation tree formation on the flow regime through the DM plane need to be studied.

Effect of DM properties on water retention and dry out mitigation

In this work, it was demonstrated that the open metallic element fuel cell operation is limited by dry-out as a result of low back diffusion of water. However, efforts in tailoring DM have always focused on improving water removal away from the catalyst layer and into the channels, because the conventional flow field limited operation from excess water at the cathode, known as flooding. With the development of more porous metallic flow field, DM should be carefully tailored to improve water retention to promote back

diffusion, without causing an excess of water flooding. The fundamental need for a DM can also be questioned when using a porous metallic flow field.

Cell active area compression

This work showed that an open metallic element flow field improves cell ohmic resistance as a result of more uniform compression, and reduced contact resistances. The experiments in this work were all conducted at a 30 kgf active area compression. The effect of compression on two-phase transport and performance should be investigated. Changing compression can alter soft material porosity and thickness, which are important parameters to changing gas phase and liquid phase transport. It is possible to see compression change the back diffusion properties of the cell. Optimal assembly compression can be identified for improved operation and transport.

Wider range of Pt loading, and understanding loading effect and effective surface area

Two different Pt loading cathodes have been used in this study (0.4 and $0.07 \text{ mgPt.cm}^{-2}$) to investigate oxygen transport resistance in the catalyst layer. It is necessary to investigate a broader range of catalyst layer loadings. Methods of catalyst synthesis have improved, and catalyst layers with different catalyst loadings can be synthesized to have similar effective surface area. The separation of the direct effect of Pt loading, and the direct effect of effective surface area on oxygen transport resistance should be better understood. It is also possible to build a series of catalyst layers with different agglomerate diameters in order to

find a direct correlation between agglomerate size and oxygen transport resistance through thin film.

Durability study from dry-out cycling at ultra-high current density

This work shows stable operation at high current density with partial membrane dry-out. Even though no loss of performance was recorded after dry-out events, consecutive dry-out and rehydration cycles were not investigated. Ultra-high current density induced dry-out cycling should be used to understand membrane durability under such operating conditions. As the membrane is operated under partial dry-out from the anode side local stresses induced by overheating could damage the membrane.

Appendix A: Data repeatability from cell assemblies

As shown in Figure A1.1, start with the cathode seal plate bolted on the mounting frame and place the six bolt insulations as shown in the figure. From this point on always leave fixture lying down.

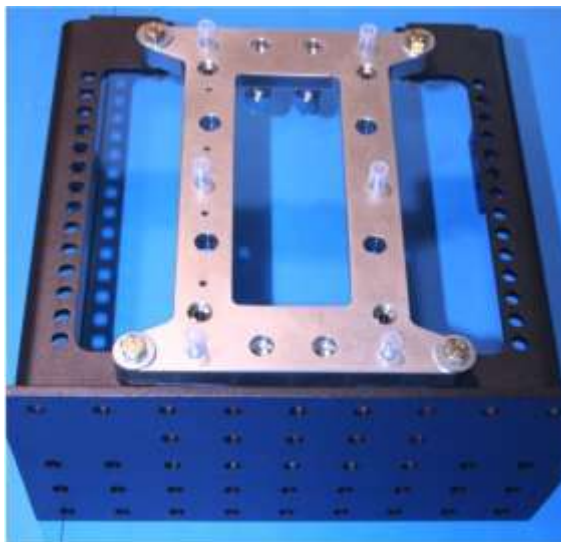


Figure A1.1 – Cathode seal plate bolted to mounting frame

Superpose the following items in order on top of the cathode seal plate:

1. Cathode cooling cell plate
2. Cathode cooling cell gasket
3. Cathode cooling cell flow field
4. Cathode bipolar plate
5. Cathode gasket
6. Cathode flow field
7. Cathode diffusion media (microporous layer facing the membrane)
8. Membrane electrolyte assembly (Anode side up)
9. Anode diffusion media (microporous layer facing the membrane)
10. Anode gasket
11. Anode flow field
12. Anode bipolar plate
13. Anode cooling cell gasket
14. Anode cooling cell flow field
15. Anode cooling cell plate

Install the anode seal plate, with the six seal screws with 120 in.lbs of torque, as shown in Figure A1.2.

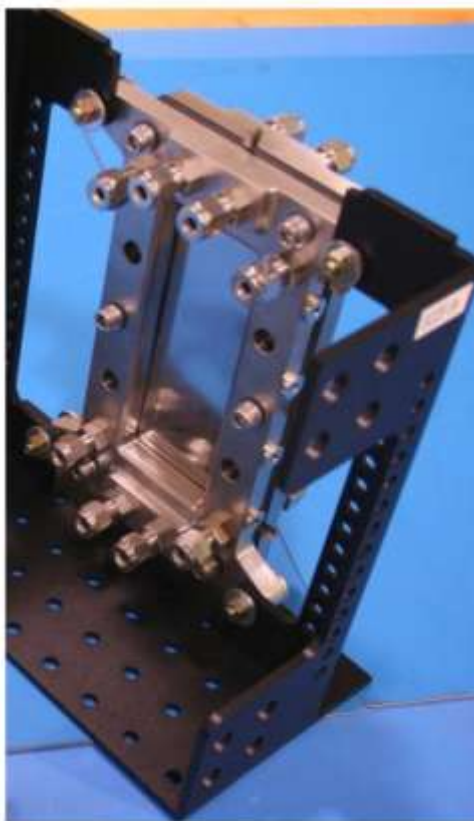


Figure A1.2 – Sealed cell assembly

Install the current collectors with the active area compression plates and hand-tighten the bolts compressing the bellevilles, as shown in Figure A1.3.

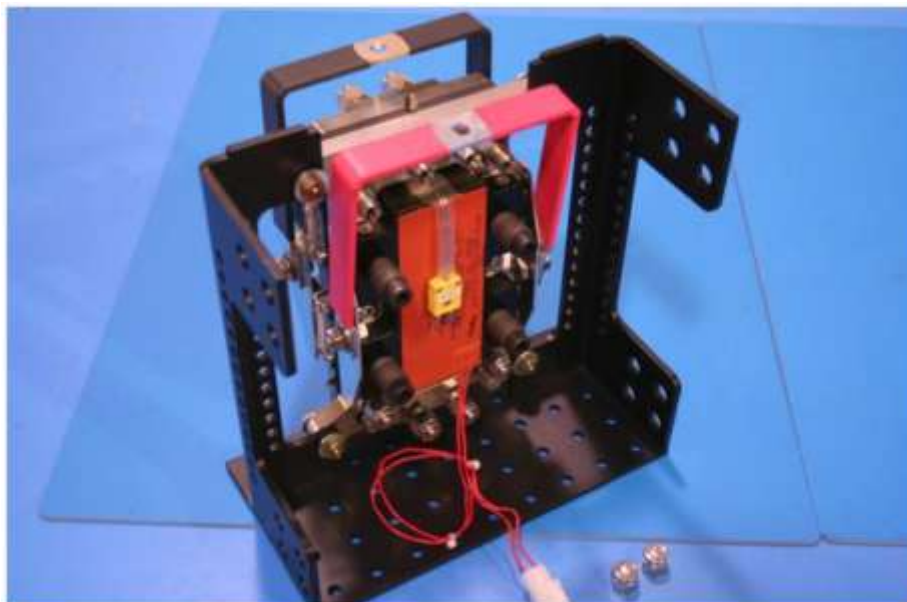


Figure A1.3 – Assembled cell with active area compression

Leak check the cell compartments with nitrogen, without exceeding 60 psi. If the cell is not leaking proceed with belleville compression as shown in Figure A1.4. To assemble at 30 kgf of compression, belleville height [A] and [B] should average to 29.68 cm.

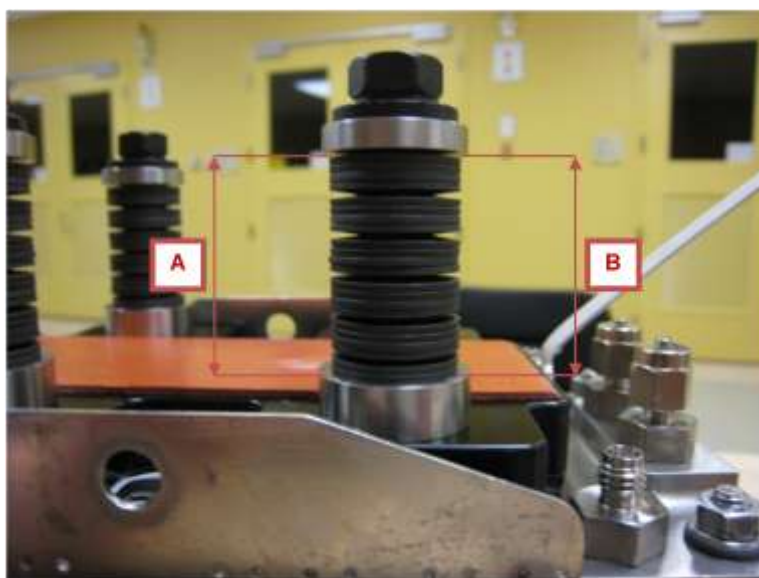


Figure A1.4 – Belleville height measurement. Average [A] and [B] height of 28.69 cm on each bolt resulting in 30 kgf of compression.

Following this method ensures repeatability of cell assemblies, and guarantees repeatable performance as observed in Figure A1.5, at 60°C using stoichiometries of 2, 1.8 Bara inlet pressure, and 53% / dry relative humidity.

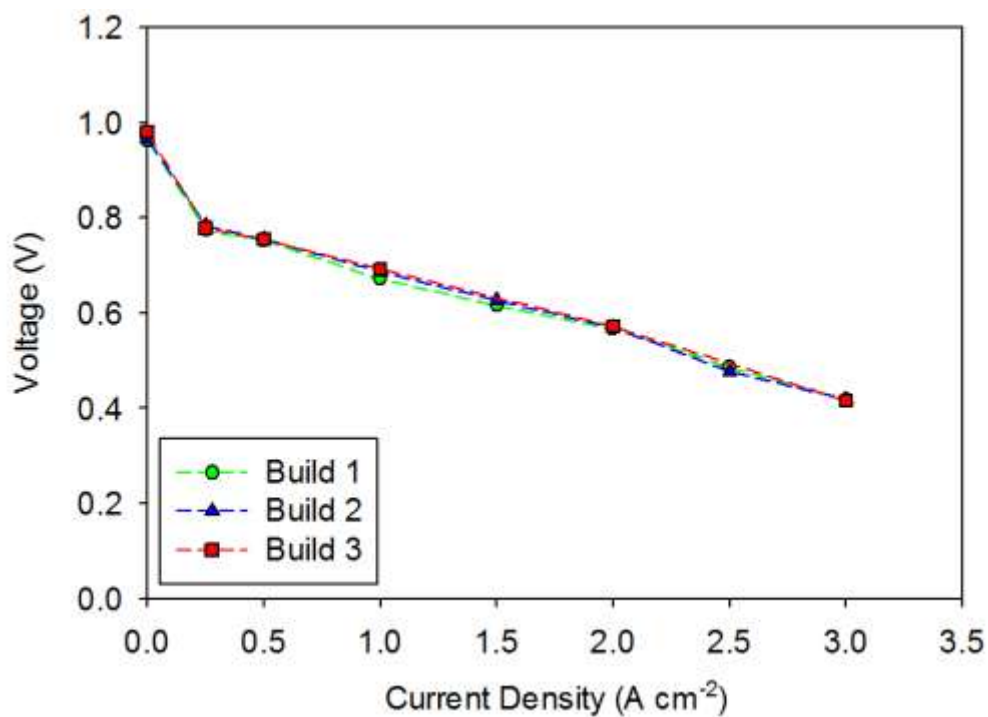


Figure A1.5 – Performance curves at 60°C for three

Appendix B: Electrochemical Impedance Spectroscopy Verification with Kramer-Kronig Transform

Electrochemical impedance spectroscopy measurements were recorded after changing an extensive parameter, such as temperature, pressure or current density, and sometimes a combination of both. The fuel cell must be in equilibrium over the entire frequency range of an EIS experiment, in order to have reliable complex non-linear least squares analysis of the impedance data. It is therefore important to conduct an independent check of the validity of the impedance data and their compliance within the constraints of linear systems theory [1-6].

Kramers-Kronig transform theory states that real and imaginary impedance data should contain equivalent information. In other words, the imaginary values of a dispersion can be calculated from the real parts of the dispersion and vice versa, over the whole frequency range ($\omega = 0$ to $\omega = \infty$). The transformation for the real part of the impedance, $Z_{re}(\omega)$, is expressed as

$$Z_{re}(\omega) = Z_{re}(\omega) + \frac{2}{\pi} \int_0^{\infty} \frac{x Z_{im}(x) - \omega Z_{im}(\omega)}{x^2 - \omega^2} dx \quad (\text{A.1})$$

And the imaginary part $Z_{im}(\omega)$, is expressed as

$$Z_{im}(\omega) = -\frac{2\omega}{\pi} \int_0^{\infty} \frac{Z_{re}(x) - Z_{re}(\omega)}{x^2 - \omega^2} dx \quad (\text{A.2})$$

Where ω is the frequency of transform and x is the frequency of integration.

In order to attribute validation for a data set, the measured real part and transformed imaginary part, Equation A.1, should match. The same is true for the measured imaginary

part and the transformed real part, Equation A.2. The process is represented graphically in Figure A.1. The transformed spectra should be identical to the measured spectra. If they are not the same, this suggests a problem with the original data [6].

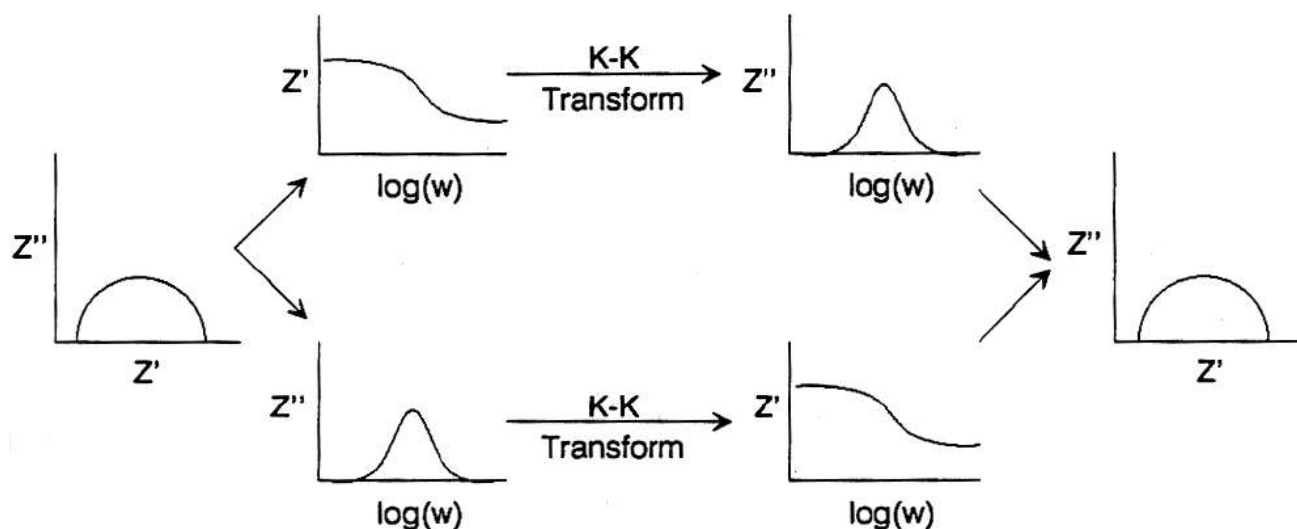


Figure A.1: Graphical representation of impedance data validation via Kramer-Kronig transform.

The Kramers-Kronig transform was applied using ZView software by Scribner Associates Inc. A good match was computed for all EIS data, two sets are selected here under different operating conditions and are shown in Figures A.2 and A.3.

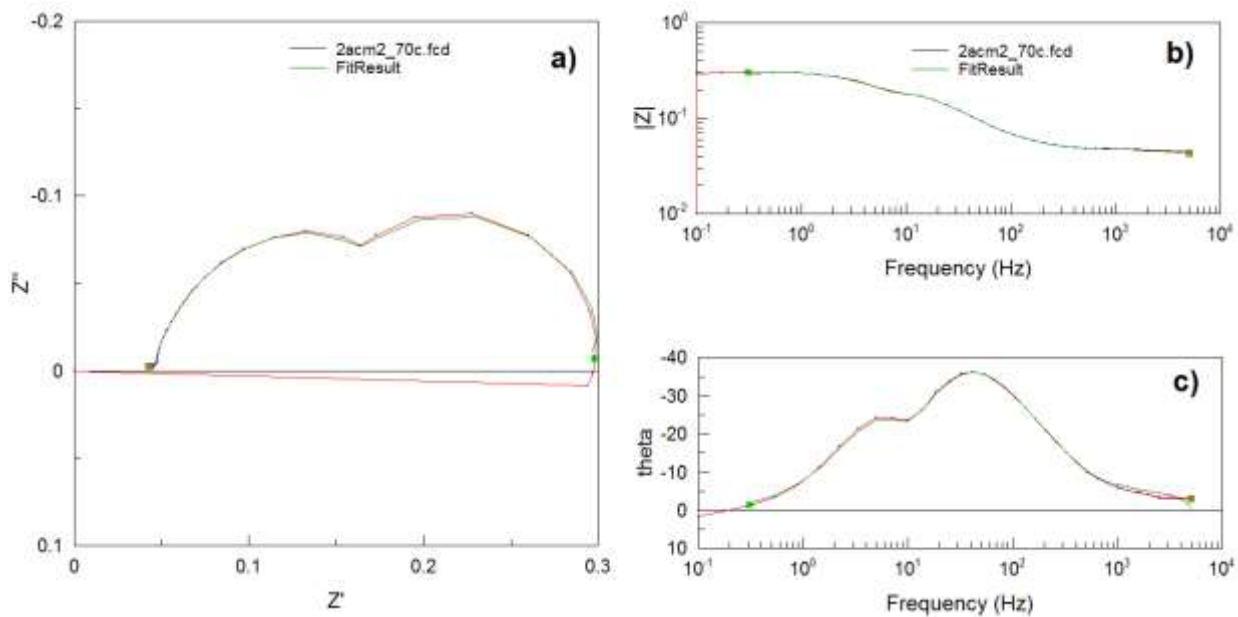


Figure A.2: EIS data and their corresponding KK transform. a) Nyquist plot, b) Magnitude, c) Angle (70°C, RH 53/0, BP 1.8/1.8 Bara at 2 A cm⁻²).

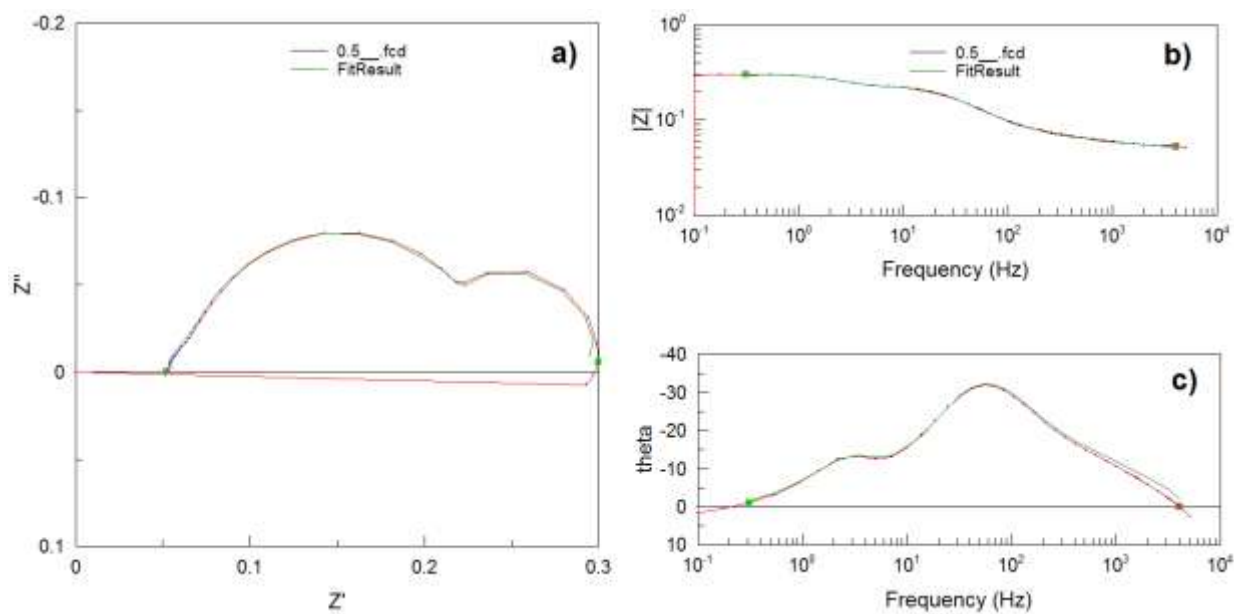


Figure A.3: EIS data and their corresponding KK transform. a) Nyquist plot, b) Magnitude, c) Angle (60°C, RH 100/0, no BP at 0.5 A cm⁻²).

1. D. D. Macdonald, M. Urquidi-Macdonald, “Application of Kramers-Kronig Transformations in the Analysis of Electrochemical Impedance Data, Part 1”, J Electrochem Soc, 132(10), p 2317, 1986.
2. D. D. Macdonald, M. Urquidi-Macdonald, “Application of Kramers-Kronig Transformations in the Analysis of Electrochemical Impedance Data, Part 2” J Electrochem Soc, 133 (10), 2023 1986.
3. M. Urquidi-Macdonald, S Real, D. D. Macdonald, Applications of Kramers-Kronig transforms in the analysis of electrochemical impedance data—III. Stability and linearity. Electrochim Acta 35(10):1559–66, 1990.
4. N. Priyantha, P. Jayaweera, D. D. Macdonald, A. Sun, “An electrochemical impedance study of alloy 22 in NaCl brine at elevated temperature. I. Corrosion behavior”. J Electroanal Chem 572 (2):409–19, 2004.
5. M. Shi, Z. Chen, J. Sun, “Kramers-Kronig transform used as stability criterion of concrete”. Cem Concr Res 29(10):1685–8 1999.
6. BA Boukamp, Practical application of the Kramers-Kronig transformation on impedance measurements in solid state electrochemistry. Solid State Ionics 62(1–2):131–41 1993.

Curriculum Vitae – Abdul Kader (AK) Srouji

Education

The Pennsylvania State University

Doctor of Philosophy, Energy and Mineral Engineering, 2014

Masters of Science, Mechanical Engineering, 2010

The American University of Beirut

Bachelor of Engineering, Mechanical Engineering, 2008

Peer Reviewed Journal Papers and Book Chapter

Srouji A. K., Zheng L. J., Dross R., Mench M. M., “Oxygen Transport in PEFC with Ultra-low Loading Electrodes”, in prep.

Srouji A. K., Zheng L. J., Dross, R., Turhan A., Mench M. M., “Water Management in PEFC with Porous Metallic Flow Field at Ultra-high Current Density”, Journal of Power Sources, in press.

Srouji A. K., Zheng L. J., Dross, R., Turhan A., Mench M. M., “Performance and Mass Transport in Open Metallic Element Architecture Fuel Cells at Ultra-high Current Density”. Journal of Power Sources, 218, 341 (2012)

Srouji A. K., Mench M. M., “Freeze-Related Degradation in Polymer Electrolyte Fuel Cells”. Elsevier Academic Press, Chapter 6, 293-329 – 2011.

Zheng L. J., **Srouji A. K.**, Dross, R., Turhan A., Mench M. M., “Computational Engineering of Porous Flow Field PEFCs to Enable High Temperature High Power Density Operation”. Journal of the Electrochemical Society, 160, F119 (2013)

Zheng L. J., **Srouji A. K.**, Turhan A., Mench M. M., “Computational Exploration of Ultra-high Current PEFC Operation with Porous Flow Field”. Journal of the Electrochemical Society, 159, F267 (2012)

Zheng L. J., **Srouji A. K.**, Gambini, F., Mench M. M., “Exploration of Ultra-high Current Operation in PEFC Using a Validated Model”. ECS Transaction, 41 (1), 229 (2011).

Presentations at Technical Conferences

Srouji A.K., Zheng L. J., Turhan A., Mench M. M., “Eliminating the Channel/Land Paradigm: Ultra-high Current Density Operation of PEFC with Open Metallic Element Flow Field” 1st international education forum on environment and energy science. (Won best presentation award).

Srouji A. K., Zheng L. J., Mench M. M., “Study of Water Transport in a PEFC with an Open Metallic Element Flow Field at Ultra-High Current Density” 221st ECS Meeting, Seattle, May 2012.

Srouji A. K., Zheng L. J., Mench M. M., “A Comparison of Open Flow Field and Conventional PEFC Architecture Limitations at Ultra-High Current Density”, 219th ECS Meeting, Montreal, May 2011.

Srouji A.K., Mench M. M., “Investigation of Degradation from Repeated Sub-Zero Cold Starts in PEFC”, 219th ECS Meeting, Montreal, May 2011.

Personal Contact Info

For any information relevant to this dissertation, publications, or otherwise feel free to contact the author at:
ak.srouji@gmail.com